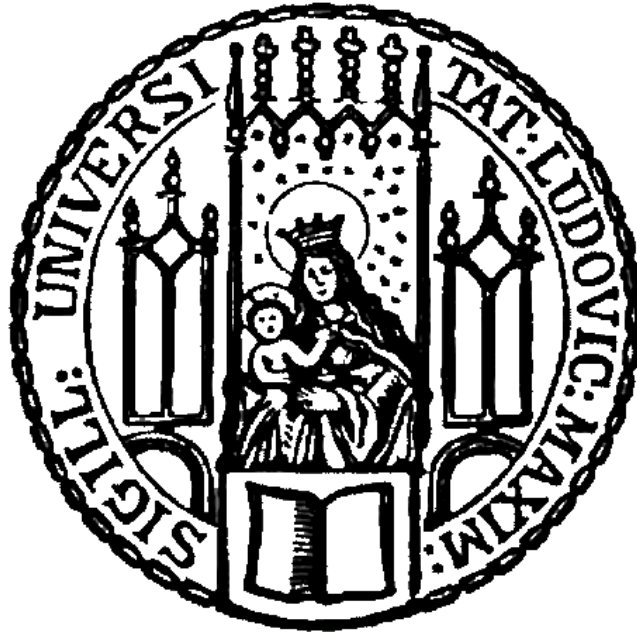


**Dissertation zur Erlangung des Doktorgrades
der Fakultät für Chemie und Pharmazie
der Ludwig-Maximilians-Universität München**



**Novel Chemical Tools to Target Two-Pore Channel 2,
P-Glycoprotein and Histone Deacetylase 6 in Cancer**

Martin Müller
aus Memmingen, Deutschland
2020

Erklärung

Diese Dissertation wurde im Sinne von § 7 der Promotionsordnung vom 28. November 2011 von Frau Prof. Dr. Angelika M. Vollmar betreut.

Eidesstattliche Versicherung

Diese Dissertation wurde eigenständig und ohne unerlaubte Hilfe erarbeitet.

München, den 30.07.2020

(Martin Müller)

Dissertation eingereicht am: 31.07.2020

1. Gutachterin: Prof. Dr. Angelika M. Vollmar

2. Gutachter: Prof. Dr. Franz Bracher

Mündliche Prüfung am: 03.09.2020

Meinen Eltern

Table of contents

1	Summary.....	1
2	Introduction	5
2.1	The need for identification of novel, druggable targets in cancer.....	5
2.2	Endolysosomal two-pore channel 2 as novel target for cancer therapy.....	5
2.3	Successful inhibition of the efflux transporter P-glycoprotein – an unmet need in tumor therapy	7
2.4	Targeting lysosomal ion channels as potential strategy to overcome chemoresistance in cancer	9
2.5	Histone Deacetylase 6 - an emerging drug target in cancer therapy	9
2.6	Aims of the study	12
3	Materials and Methods	14
3.1	Materials.....	14
3.1.1	Compounds	14
3.1.2	Reagents: Biochemicals, kits, inhibitors and cell culture reagents.....	14
3.1.3	Technical equipment.....	17
3.2	Cell culture	17
3.2.1	Cell culture buffers and solutions	17
3.2.2	Cell lines.....	18
3.2.3	Passaging.....	19
3.2.4	Freezing and thawing	19
3.3	Apoptosis assays.....	20
3.4	Calcein-AM retention assay	20
3.5	Cellular uptake assay	20
3.6	CYP3A4 P450-Glo™ assay	21
3.7	Endolysosomal patch clamp method	22
3.8	Fura-2 Ca ²⁺ imaging	22

Table of contents

3.9	Fluo-4 Ca ²⁺ imaging.....	23
3.10	FLIM-FRET imaging	23
3.11	Generation of a RIL175 TPC2 knockout cell line using CRISPR-Cas9.....	25
3.11.1	sgRNA design and cloning of constructs.....	25
3.11.2	Transfection and evaluation of genome targeting efficiency.....	27
3.11.3	Single cell dilution, clonal expansion and knockout verification.....	27
3.11.4	Off-target screening	28
3.12	Generation of a VCR-R CEM TPC2 knockout cell line using CRISPR-Cas9 ...	28
3.13	<i>In vivo</i> experiments.....	29
3.14	Lysosomal uptake assay.....	30
3.15	Mitochondrial mass.....	30
3.16	Mitochondrial membrane potential	31
3.17	Molecular cloning of pcDNA3-CYP3A4-EGFP	32
3.18	Proliferation assays	34
3.19	Western Blot analysis	35
3.20	Wound healing assay	38
3.21	Seahorse XF ⁹⁶ : Metabolic profiling	38
3.21.1	Purpose and measurement principle	38
3.21.2	Hydration of the Seahorse XF ⁹⁶ sensor cartridge	39
3.21.3	Coating of the Seahorse XF ⁹⁶ microplate	39
3.21.4	Seeding and treatment of cells in the XF ⁹⁶ microplate.....	39
3.21.5	Preparation of assay medium	39
3.21.6	Washing of cells in the XF ⁹⁶ microplate.....	40
3.21.7	Loading of the XF ⁹⁶ sensor cartridge with injection compounds	40
3.21.8	Seahorse run.....	40
3.22	Quantitative real-time PCR analysis	41
3.23	Statistical analyses	42
3.24	Toxicity assays	42

Table of contents

4	Results	46
4.1	Part I: Tetrahydroisoquinolines as inhibitors of TPC2 and P-gp	46
4.1.1	Functional effects of TPC2 knockout on liver cancer cells.....	46
4.1.1.1	Generation and validation of a TPC2 knockout cell line using CRISPR-Cas9	46
4.1.1.2	TPC2 KO reduces proliferation and prevents tumor growth of HCC cells	47
4.1.1.3	TPC2 KO influences cellular energy metabolism.....	49
4.1.2	Development and biological investigation of novel cytostatic TPC2 inhibitors	50
4.1.2.1	Screening of a library of (bis)benzyltetrahydroisoquinolines	50
4.1.2.2	Functional characterization of the tetrandrine congeners SG-005 and SG-094	56
4.1.2.3	SG-005 and SG-094 are less toxic to non-cancerous cells than tetrandrine.....	60
4.1.2.4	SG-094 reduces tumor growth in a murine HCC model.....	62
4.1.3	TPC2 knockout or inhibition impairs phosphorylation of Akt and hexokinase II <i>in vivo</i>	64
4.1.4	Tetrandrine toxicity is independent of CYP3A4 expression <i>in vitro</i>	65
4.1.5	TPC2 blockers also act as P-gp inhibitors and <i>vice versa</i>	69
4.1.5.1	Simplified tetrandrine congeners inhibit P-gp	69
4.1.5.2	Third generation P-gp inhibitor elacridar is a potent TPC2 blocker	70
4.1.6	TPC2 function impacts chemoresistance of P-gp overexpressing cells....	71
4.1.7	Combination with benzylisoquinolines is beneficial in sorafenib-resistant hepatocellular carcinoma cells.....	73
4.1.8	Biological characterization of the isoquinoline-benzylisoquinoline alkaloid muraricine	74
4.1.9	Part I: Summary.....	78
4.2	Part II: Phenothiazine-based benzhydroxamic acids as inhibitors of HDAC6 ..	79
4.2.1	Functional characterization of the HDAC6 inhibitors KV-46, KV-70 and KV- 181	79

Table of contents

4.2.2	Influence of HDAC6 inhibition on immune checkpoints and unfolded protein response	81
4.2.3	Part II: Summary.....	83
5	Discussion.....	85
5.1	Discussion part I.....	85
5.1.1	Validation of two-pore channel 2 as target for cancer therapy and development of synthetically accessible inhibitors.....	85
5.1.2	Tetrandrine toxicity is independent of cellular CYP3A4 expression.....	88
5.1.3	TPC2, tetrahydroisoquinolines and chemoresistance	89
5.2	Discussion part II.....	92
6	References.....	95
7	Appendix	108
7.1	Supplementary Information.....	108
7.1.1	Supplementary Figures.....	108
7.1.2	Supplementary Tables.....	115
7.2	Abbreviations.....	121
7.3	Index of figures	123
7.4	Index of tables	125
7.5	Acknowledgements.....	126
7.6	List of publications and conference contributions.....	128
7.6.1	Research articles.....	128
7.6.2	Conference contributions.....	129

SUMMARY



1 Summary

The identification of previously unknown targets as well as the development of efficacious inhibitors for known targets are key factors to make more patients benefit from tumor therapy. For instance, the role of two-pore channel 2 (TPC2), one of the few cation channels localized on endolysosomal membranes, in cancer remains poorly understood. Here, we report that TPC2 knockout reduces proliferation of liver cancer cells *in vitro*, affects their energy metabolism and successfully abrogates tumor growth *in vivo*. Concurrently, we have identified novel, simplified analogues of the alkaloid tetrandrine (SG-005 and SG-094) as potent TPC2 inhibitors by screening a library of benzyltetrahydroisoquinoline derivatives using cell proliferation assays, endolysosomal patch clamp and calcium imaging. Removal of dispensable substructures of the lead molecule tetrandrine increases antiproliferative properties against several cancer cell lines and impairs proangiogenic signaling of endothelial cells to a greater extent than tetrandrine. Simultaneously, toxic effects on non-cancerous cells are reduced, allowing *in vivo* administration and revealing the first TPC2 inhibitor with antitumor efficacy in mice (SG-094). Hence, our study unveils TPC2 as valid target for cancer therapy and provides novel, easily accessible tetrandrine analogues as promising option for effective pharmacological interference.

Furthermore, in-depth studies were conducted to investigate a postulated mechanism of metabolic toxification of tetrandrine. A combined medicinal chemistry and cell biology approach showed that a reduction of the toxicity of tetrandrine cannot be achieved by replacing or eliminating the hypothesized metabolically instable functional group, clearly indicating that the proposed pathway is not the primary cause for the *in vitro* toxicity of tetrandrine and related alkaloids.

Moreover, we have uncovered that the simplified tetrandrine congeners SG-005 and SG-094 additionally inhibit P-glycoprotein (P-gp), a drug efflux pump associated with multidrug resistance and treatment failure in tumor therapy. Since no approved molecules targeting P-gp are currently available, SG-005 and SG-094 might represent promising candidates to treat drug-resistant cancers owing to their favorable drug-like properties. Generally, the dual mode of action of isoquinoline-based TPC2/P-gp antagonists is mentioned here for the first time. Based on this, the known third-generation P-gp inhibitor elacridar was exemplarily studied for its potential to block TPC2, revealing another potent TPC2 blocker and thereby challenging the assumption of elacridar specifically acting on efflux pumps.

Summary

Hence, on the one hand, a new lead structure (elacridar) for the development of prospective TPC2 blockers is provided. On the other hand, hints for common structural motifs on TPC2 and P-gp are given, which can facilitate the search for additional TPC2 antagonists.

We further uncovered that TPC2 and P-gp do not only share mutual small molecule inhibitors, but also seem to be functionally connected. This is reflected by the higher sensitivity of TPC2-deficient, drug-resistant leukemia cells to vincristine, opening the stage for further studying the implication of TPC2 in processes related to (P-gp-mediated) chemoresistance.

Summarizing, this work clearly illustrates that the endolysosomal cation channel TPC2 is a suitable target for tumor therapy. Additionally, synthetically accessible, potent TPC2 blockers were developed as promising preclinical candidates, making TPC2 a druggable protein target. Further, an implication of TPC2 and blockers of this channel in chemoresistance was uncovered, both by TPC2 promoting chemoresistance as well as by the dual action of isoquinolines on TPC2 and the drug efflux pump P-gp.

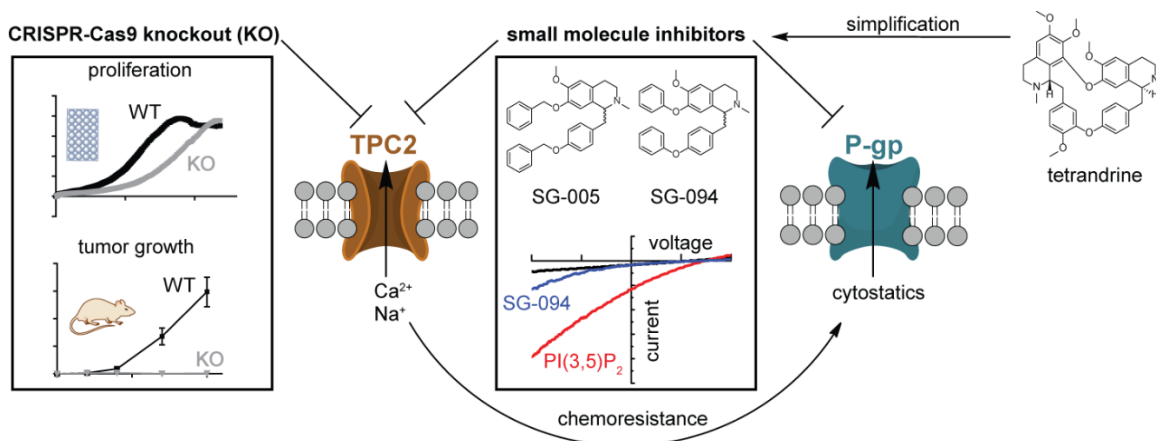


Figure 1 | Targeting TPC2 and P-gp in cancer – the project at a glance

Histone deacetylase 6 (HDAC6) is another protein that has gained attention as target for tumor therapy. HDAC6 is primarily located to the cytoplasm, where it deacetylates several non-histone proteins and thereby alters critical cancer-related pathways. Selective targeting of HDAC6 is aimed to reduce the toxicity associated with pan-HDAC inhibition and, along this line, we have developed and characterized potent and selective HDAC6 inhibitors (KV-46, KV-70, KV-181) with a phenothiazine system as cap group and a benzhydroxamic acid moiety as zinc-binding group. In accordance with effects of specific HDAC6 inhibition, KV-46, KV-70 and KV-181 are relatively non-toxic to healthy liver cells and moderately effective at reducing cancer cell proliferation and inducing apoptosis. Further, KV-46, KV-70 and KV-181 exposure increases the expression of critical protein markers of the unfolded protein response and the immune response, suggesting a potential benefit of combining HDAC6 inhibitors with proteasome inhibitors or immunomodulatory agents.

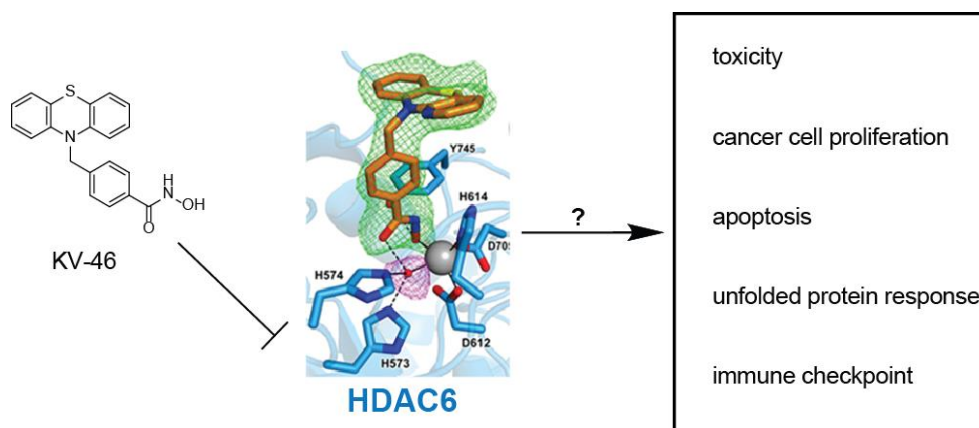


Figure 2 | Characterization of HDAC6 inhibitors in cancer – the project at a glance

INTRODUCTION



2 Introduction

2.1 The need for identification of novel, druggable targets in cancer

With an estimated number of 9.6 million deaths worldwide in 2018¹, cancer-related mortality represents a major health problem to date. Huge efforts have been made to identify suitable targets for cancer therapy and 109 protein targets could be addressed by 85 protein-targeted oncology drugs in 2017². On the contrary, around 600 cancer drivers have been discovered, but a majority thereof lacks detailed biological investigation or remains to be targeted by antitumor agents^{2, 3}. The need for the identification and validation of novel, druggable targets in cancer provided the rationale for this study. In the first part, benzylisoquinolines were utilized to block two-pore channel 2, a largely unknown target in cancer, but also to inhibit P-glycoprotein, a more established protein target. In the second part, benzhydroxamic acids were studied as subtype-selective inhibitors of histone deacetylase 6, a target with great potential in chemotherapy.

2.2 Endolysosomal two-pore channel 2 as novel target for cancer therapy

Two-pore channels (TPCs) are cation channels that span membranes of acidic vesicles of the endolysosomal (EL) system. EL ion channels are not targeted by anticancer drugs to date. Comprehensive information about structures of TPCs have long been scarce and reports about the ions they conduct were conflicting⁴. Very recent advantages, however, provided the first detailed view of an animal TPC⁵ and novel insights into the underlying mechanisms for ion selectivity⁶, respectively. There are two subtypes of TPCs in primates, TPC1 and TPC2⁴. By cryo-electron microscopy, She *et al.*⁵ have resolved the structure of mouse TPC1, comprising two subunits, each of which consisting of two transmembrane domains, 6-TMI and 6-TMII (**Figure 3**). Opening of the channel is suggested to be mediated by cooperation between the two transmembrane domains. Binding of the endogenous agonist, the phosphoinositide PI(3,5)P₂, to arginine residues of 6-TMI induces conformational changes to the pore, whereas 6-TMII acts as voltage sensor to finalize channel opening⁵. In contrast, opening of the other TPC subtype, TPC2, is not modulated by voltage changes⁴. The structure of TPC2 has not been resolved yet, but a recent report by Gerndt and coworkers⁶ improved the understanding of its ion permeability. It was shown that TPC2 conducts different ions (Na⁺, Ca²⁺) depending on its activation with either nicotinic acid adenine dinucleotide phosphate (NAADP) or PI(3,5)P₂, leading to different effects on exocytosis and lysosomal pH⁶.

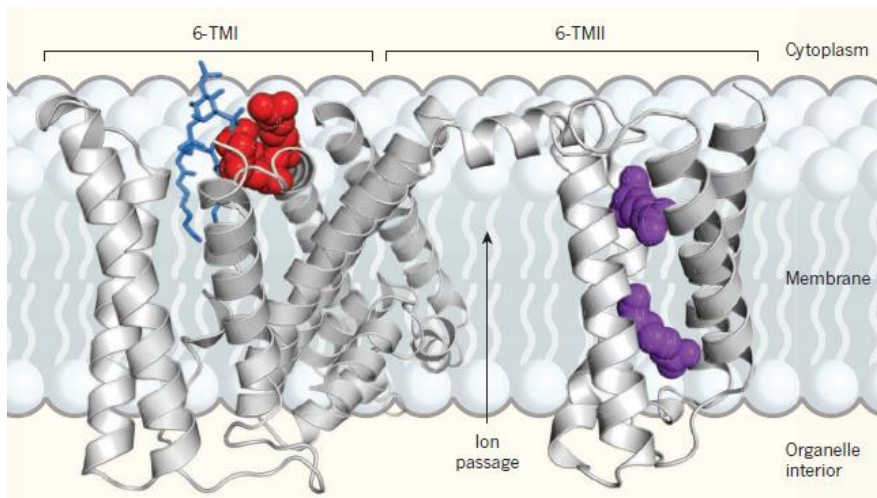


Figure 3 | Structure of murine TPC1. TPC1 consists of two subunits and each subunit has two transmembrane domains (6-TMI, 6-TMII) that are connected by a cytoplasmic linker. One TPC1 subunit is depicted here. Activation of the channel is facilitated by binding of the phosphoinositide PI(3,5)P₂ (blue) to arginine residues (red) in 6-TMI and voltage sensing in 6-TMII by arginine residues (purple), resulting in ion passage from the vesicle interior. The figure was adapted from Patel *et al.*⁴.

Aberrant TPC2 function is linked to several diseases, including Parkinson's diseases, fatty liver disease, viral infections, diabetes and cardiac dysfunction⁷. Furthermore, high gene expression of TPC2 was correlated with poor survival probability of prostate cancer patients⁸ and there is growing evidence that TPCs are necessary for sustaining cancer hallmarks^{9, 10}. Therefore, TPC2 might serve as an innovative target for antitumor drugs. In particular, silencing of TPC2, predominantly found on lysosomal membranes¹¹, reduced migration and adhesion of invasive tumor cells¹². The EL system facilitates trafficking of integrins and the disturbance of this recycling process impaired cancer cell migration *in vitro* and metastasis *in vivo*¹². Furthermore, vessel formation, a fundamental step for vascularization of solid tumors, was reduced in TPC2, but not in TPC1 knockout mice¹³. Whether TPCs, especially TPC2, are involved in other cancer hallmarks, such as sustained proliferation and deregulated cellular energetics¹⁴, however, remains largely unknown and was therefore investigated in the context of this study.

In the past years, several efforts have been made in the search for pharmacological inhibitors of TPCs, illustrating the increasing importance of the ion channels as novel drug targets. The NAADP antagonist and indirect TPC2 blocker *trans*-Ned-19 (Ned-19) reduced NAADP-induced Ca²⁺ release and was able to prevent the activation of the VEGFR2/NAADP/TPC2/Ca²⁺ signaling pathway¹³, as well as cancer cell migration¹², but required high micromolar doses ($\geq 100 \mu\text{M}$)^{12, 13}. Similarly, high concentrations ($\geq 500 \mu\text{M}$) of the direct TPC2 inhibitor naringenin were necessary to affect VEGF-evoked tube formation¹⁵. Furthermore, naringenin treatment bears the risk of undesired drug-drug

interactions due to inhibition of cytochrome P450 (CYP) enzymes, including CYP1A2¹⁶ and CYP3A4^{17, 18}, and can lead to QTc prolongation through acting on cardiac hERG channels^{19, 20}. Penny and coworkers²¹ recently extended the limited number of compounds directly inhibiting TPC2 with the dopamine receptor antagonist fluphenazine and the selective estrogen receptor modulator (SERM) raloxifene. The first-generation antipsychotic drug fluphenazine, however, can cause serious extrapyramidal side effects²², and raloxifene, used for treatment and prevention of osteoporosis, is approved for postmenopausal women only²³. Consequently, there is an emerging need for the development of inhibitors with drug-like properties and antitumor efficacy, and, concurrently, to unravel the involvement of TPC2 in cancer.

Tetrandrine, an alkaloid isolated from *Stephania tetrandra*, was recently shown to effectively inhibit cancer cell migration¹² and infections with Ebola²⁴, MERS-CoV²⁵ and SARS-CoV-2²⁶ viruses *via* directly acting on TPCs and thereby represents a promising lead structure for the development of TPC2 blockers. However, its poor solubility requires acidification of the injection solution before *in vivo* application^{24, 27} and its toxicity in animal models^{27, 28} are serious drawbacks of this compound. In addition, tetrandrine can only be obtained by extraction of plants or by complex chemical synthesis that involves 20 steps to gain enantiomerically pure tetrandrine²⁹, or 12 steps to obtain racemic tetrandrine³⁰. We aimed to overcome the outlined drawbacks by chemical simplification, substitution and derivatization of tetrandrine.

2.3 Successful inhibition of the efflux transporter P-glycoprotein – an unmet need in tumor therapy

Pharmacological activities of tetrandrine are diverse and not limited to modulation of TPCs. These include, among many others, antihypertensive³¹, anti-inflammatory³² and multidrug resistance reversing^{33, 34} effects by blocking L-Type Ca²⁺ channels³¹, proinflammatory cytokine production³² and the permeability-glycoprotein (P-glycoprotein, P-gp, ABCB1A)^{33, 34, 35}. Most importantly, tetrandrine has advanced into early phase clinical studies as P-gp inhibitor under the brand name CBT-1[®] (CBA Research, Inc.)³⁵. Although three clinical studies have either been completed or were announced (NCT00437749, NCT00972205, NCT03002805)³⁶, no study results were published since 2012 (NCT00972205)³⁵. Therefore, the current development stage of the molecule as P-gp inhibitor remains unclear and the reasons for the failure of its clinical progress are somewhat speculative. P-gp acts as an efflux pump that is capable of decreasing influx of cytostatic agents into tumor cells in an adenosine 5'-triphosphate (ATP)-dependent manner³⁷. Overexpression

of P-gp is regarded as a major contributor to treatment failure in chemotherapy and the phenomenon of multidrug resistance (MDR)³⁸. Generally, the development of efficacious P-gp inhibitors remains a high unmet need in clinics since no such approved drugs are available³⁹. In the last two decades, huge efforts have been made by both academia and industry in the search for P-gp inhibitors that can be used to overcome drug resistance in chemotherapy. With respect to their specificity and affinity, P-gp inhibitors can be divided into three generations.

The clinical use of first-generation inhibitors, approved drugs that exert inhibitory P-gp activity, such as verapamil, cyclosporine A and tamoxifen, is restricted by their dose-related toxicity to achieve the desired effect⁴⁰. The affinity of second-generation inhibitors, including valsopodar, an analogue of cyclosporine A, and dexverapamil, the D-isomer of verapamil, to P-gp could be improved, but their non-specific interaction with CYP enzymes represents a major drawback due to potential drug-drug interactions with antitumor agents. In contrast, third-generation inhibitors have a high affinity to P-gp and do not interact with CYP enzymes³⁹. Of them, elacridar was tested in clinical phase I^{41, 42} and tariquidar, laniquidar and zosuquidar have entered clinical phase II and III studies as add-on therapeutic for the treatment of newly diagnosed and/or refractory malignancies (NCT00048633, NCT00046930, NCT00028873)^{36, 39}. Even though a plethora of *in vitro* and *in vivo* data underlined effective P-gp blockade by third-generation inhibitors and, in turn, successful sensitization of drug-resistant cells and tumors, these molecules have failed in clinical studies^{43, 44}. Yet, the underlying reasons have not been completely understood. Poor pharmacokinetic properties of lipophilic third-generation P-gp inhibitors, undesired interactions with efflux transporters of the kidney, intestine, brain *etc.* leading to enforced accumulation of cytostatics in those organs and adverse events as well as the presence of P-gp-independent resistance mechanisms are hypothesized to play a role^{39, 43}. Consequently, translatability of P-gp blockade into clinical practice remains a major problem to be solved.

Recently, natural compounds, including bisbenzylisoquinoline alkaloids, have gained attention as P-gp inhibitors with tetrandrine being the most prominent representative^{37, 38}. Therefore, we aimed to test tetrandrine-derived TPC2 blockers and related benzylisoquinoline alkaloids additionally for their potential to inhibit P-gp and to reverse chemoresistance.

2.4 Targeting lysosomal ion channels as potential strategy to overcome chemoresistance in cancer

P-gp is a membrane-bound protein, usually embedded in the plasma membrane, actively transporting cargo into the extracellular space. Recently, lysosomal overexpression of P-gp has been reported in chemoresistant cells. Mechanistically, it is hypothesized that P-gp is incorporated into lysosomal membranes during trafficking and recycling events, rather than being redistributed after de-novo synthesis^{45, 46, 47}. Thus, lysosomal P-gp can contribute to the so-called drug safe house effect. In particular, the acidity of lysosomes facilitates luminal accumulation of cytostatic weak bases, leads to their protonation and reduces their ability to pass the lysosomal membrane, causing lysosomal drug sequestration. Cytostatics enter the lysosome either by passive diffusion along the pH gradient or may be actively transported across the membrane by inward turned P-gp drug efflux pumps embedded in the lysosomal membrane^{45, 46}. Consequently, localization of P-gp to lysosomal membranes can mediate drug resistance.

Since protein trafficking is dependent on proper function of EL membrane-integrated proteins, such as ion channels^{9, 12, 48}, targeting of those proteins might present a successful strategy to sensitize drug-resistant cells towards antitumor agents. In that context, knockdown or inhibition of acid sphingomyelinase und V-ATPase, which are responsible for hydrolysis of sphingomyelin and lysosomal acidification, respectively, were shown to overcome chemoresistance^{49, 50}. If blockade of lysosomal ion channels, namely TPC2, increases the sensitivity of drug-resistant cancer cells towards cytostatics, is unknown to date and was investigated in this study.

The concept of targeting lysosomes in general as well as lysosomal proteins in particular might represent a promising option to overcome chemoresistance in cancer therapy. It was reviewed as part of this work and published in the journal *Frontiers in Oncology – Section Molecular and Cellular Oncology* (Frontiers Media) in 2020⁵¹.

2.5 Histone Deacetylase 6 - an emerging drug target in cancer therapy

Cancer hallmark characteristics, such as proliferation and migration that were introduced in chapter **2.2**, are the consequences of genetic alterations, but also epigenetic mechanisms play a crucial role⁵². Since epigenetic changes, such as DNA methylation and histone modifications, are potentially reversible, reverting those alterations represents an opportunity for pharmacological intervention in tumor therapy.

Posttranslational modifications of lysines on histones include acetylation, catalyzed by histone acetylases (HATs), and deacetylation, catalyzed by histone deacetylases (HDACs)⁵². There are 18 HDAC members which can be classified into class I (HDAC1, 2, 3, 8), class II (HDAC4, 5, 6, 7, 9, 10) and class IV (HDAC11) HDACs⁵³. Whereas the substrates of most zinc-dependent HDACs are histones, the HDAC6 isozyme is unique in that it is predominantly localized in the cytoplasm and as a result mainly deacetylates non-histone proteins as α -tubulin in microtubules⁵⁴, the heat shock protein 90 (HSP90) chaperone⁵⁵ and cortactin⁵⁶, among others. By formation of complexes with its partner proteins, HDAC6 regulates many important cellular processes such as cell motility, cell spreading, misfolded protein degradation, transcription, cell proliferation and death, and stress or immune response⁵⁷. In consequence, misregulation of HDAC6 activity is associated with a variety of human diseases, which highlights it as a potential therapeutic target. HDAC6 is implicated in various neurodegenerative disorders, including Alzheimer's, Parkinson's, and Huntington's diseases⁵⁸ as well as autoimmune and inflammatory disorders⁵⁹. Moreover, high expression levels of HDAC6 seem to play a crucial role in the pathogenesis of cancer, for instance, as found in acute myeloid and myeloblastic leukemia, as well as in breast and ovarian cancer⁶⁰.

Until now, all approved HDAC inhibitors for cancer treatment target multiple HDACs. Their poor selectivity, however, can dose-dependently cause serious side effects^{53, 61}, which might limit their clinical use in oncology and beyond. Therefore, the development of inhibitors for the particular isoform of interest is of great relevance, and selective inhibition of HDAC6 may lead to fewer severe side effects⁶².

Various selective HDAC6 inhibitors have emerged over the years, mainly containing a hydroxamic acid as zinc-binding group (ZBG) (**Figure 4**). For instance, tubastatin A, a γ -carboline-based hydroxamic acid with a benzylic linker, was developed utilizing a structure-based drug design combined with homology modeling and displays high potency on HDAC6 with an IC_{50} of 15 nM and over 1000-fold selectivity over HDAC1⁶³. Tubastatin A showed neuroprotective effects without adverse toxicity and in recent preclinical tests in animal models, it reduced stroke-induced brain infarction and functional deficits⁶⁴ as well as reverted cognitive impairment in Alzheimer's disease transgenic mice⁶⁵. Ricolinostat, another potent but less selective inhibitor with at least 10-fold selectivity for HDAC6 relative to class I HDACs, possesses favorable characteristics for drug development. In combination with the proteasome inhibitor bortezomib, ricolinostat showed synergistic anti-multiple myeloma activity *in vitro*⁶⁶. Ricolinostat is the first HDAC6 inhibitor with reduced class I activity that has entered clinical trials and it is currently investigated in

patients with relapsed or refractory multiple myeloma in combination with lenalidomide and dexamethasone as well as with bortezomib and dexamethasone^{67, 68}.

A large number of HDAC inhibitors share common structural features, including the ZBG, the linker, and the cap group (**Figure 4**). A key point to gain subtype selectivity is the capping motif, which interacts with the surface of the wide basin surrounding the binding pocket of the enzyme⁶⁹. On the basis of the knowledge of the structural parameters essential for selective HDAC6 inhibitor activity, we chose to investigate and characterize new hydroxamate-based HDAC6 inhibitors that might gain the desired isoenzyme selectivity by their capping motif (lead structure: KV-46, **Figure 4**).

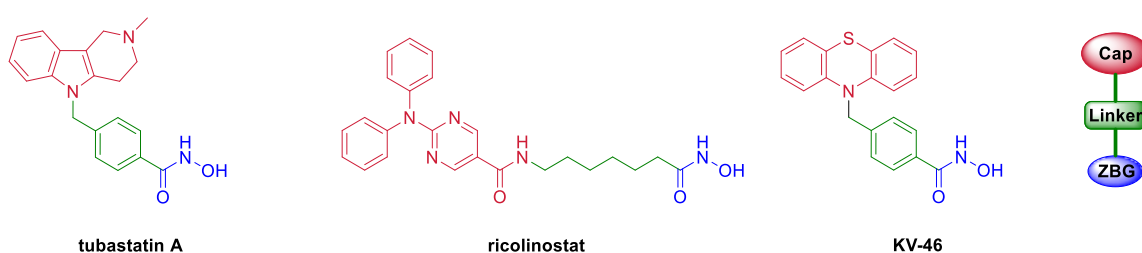


Figure 4 | Structures of known HDAC6 inhibitors (tubastatin A, ricolinostat) and the novel hydroxamate-based lead structure KV46. The general structure of these inhibitors consists of a cap group (in red), a linker (in green) and a zinc-binding group (ZBG, in blue).

2.6 Aims of the study

This study's main objectives were, on the one hand, to explore the suitability of TPC2 as target for tumor therapy and, concurrently, we aimed to develop efficacious TPC2 blockers. On the other hand, novel inhibitors of known, cancer-related targets, namely P-gp and HDAC6, should be identified and investigated.

Part I: TPC2, P-gp and tetrahydroisoquinolines

1. Elucidation of the role of the lysosomal ion channel TPC2 as suitable target for tumor therapy by studying the impact of genetic TPC2 knockout on proliferation, tumor growth and energy metabolism
2. Development of synthetically accessible TPC2 inhibitors with improved drug-like properties by simplification of the bisbenzylisoquinoline alkaloid tetrandrine
3. Studies on CYP3A4-mediated toxification of tetrandrine
4. Testing of advanced TPC2 blocker candidates for their potential to inhibit the efflux pump P-gp and to reverse chemoresistance
5. Determination of potential chemosensitizing effects of genetic TPC2 knockout on multidrug resistant leukemia cells
6. Biological characterization of the isoquinoline-benzylisoquinoline alkaloid muraricine

Part II: HDAC6 inhibitors

1. Functional characterization of the HDAC6 inhibitors KV-46, KV-70 and KV-181 (phenothiazine-based benzhydroxamic acids) in tumor cells concerning proliferation and apoptosis
2. Analysis of toxicity of KV-46, KV-70 and KV-181 to hepatocyte-like cells
3. Studies on the influence of KV-46, KV-70 and KV-181 on markers of the unfolded protein response and immune checkpoints

MATERIALS AND METHODS



3 Materials and Methods

3.1 Materials

3.1.1 Compounds

Compound	Producer/source
berbamine dihydrochloride	Sigma-Aldrich, Taufkirchen, Germany
cepharanthine	Carbosynth, Compton, Berkshire, UK
dauricine	Carbosynth, Compton, Berkshire, UK
elacridar	Sellekchem, Houston, USA
KV compounds	Katharina Vögerl (Prof. Bracher, LMU Munich)
oxyacanthine	abcr, Karlsruhe, Germany
<i>rac</i> -muraricine (muraricine)	Ramona Schütz (Prof. Bracher, LMU Munich)
<i>rac</i> -naringenin (naringenin)	Sigma-Aldrich, Taufkirchen, Germany
RMS compounds	Ramona Schütz (Prof. Bracher, LMU Munich)
SG compounds	Susanne Gerndt (Prof. Bracher, LMU Munich)
sorafenib	Enzo Life Sciences, Farmingdale, USA
tetrandrine	Prof. Peter Pachaly
TPCA1-N	Susanne Gerndt (Prof. Bracher, LMU Munich)
TPCA1-P	Susanne Gerndt (Prof. Bracher, LMU Munich)
<i>trans</i> -Ned-19 (Ned-19)	Tocris Bioscience, Bristol, UK
vincristine	Adipogen Corporation, San Diego, USA
Z compounds	Prof. Meinhart Zenk

Table 1 | Compounds

3.1.2 Reagents: Biochemicals, kits, inhibitors and cell culture reagents

Reagent	Producer
Amaya Nucleofector Kit C	Lonza, Basel, Switzerland
ATP (25 mM)	Lucigen, Wisconsin, USA
Bovine serum albumin (BSA)	Sigma-Aldrich, Taufkirchen, Germany
Bradford reagent Roti® Quant	Bio-Rad, Munich, Germany
Calcein-AM	Biomol GmbH, Hamburg, Germany
CellTiter-Blue® reagent	Promega, Mannheim, Germany
CellTiter-Glo® reagent	Promega, Mannheim, Germany
CellTrace™ CFSE Reagent	Thermo Fisher, Waltham, USA
Collagen G	Biochrom AG, Berlin, Germany
Complete®	Roche Diagnostics, Penzberg, Germany

Reagent	Producer
Corning® Cell-Tak™ Cell and Tissue Adhesive	Corning Inc., Corning, USA
CYP3A4 P450-Glo™ assay	Promega, Mannheim, Germany
Dimethylsulfoxide (DMSO)	Sigma-Aldrich, Taufkirchen, Germany
Dithiothreitol (DTT)	Sigma-Aldrich, Taufkirchen, Germany
Dulbecco's Modified Eagle Medium (DMEM)	PAA Laboratories, Pasching, Austria
Dulbecco's Modified Eagle Medium (DMEM) 5030-10X1L Powder	Sigma-Aldrich, Taufkirchen, Germany
EGCM Kit enhanced	PELO Biotech GmbH, Martinsried, Germany
Ethylendiaminetetraacetic acid (EDTA)	Sigma Aldrich, Taufkirchen, Germany
FastAP™ Thermosensitive Alkaline Phosphatase and buffers	Thermo Fisher, Waltham, USA
FastDigest restriction enzymes and buffer	Thermo Fisher, Waltham, USA
Fetal calf serum (FCS)	Biochrom AG, Berlin, Germany
G418 powder	Sigma-Aldrich, Taufkirchen, Germany
GlutaMAX™ Supplement	Life Technologies, Eugene, USA
Glycerol	Applichem, Darmstadt, Germany
HepaRG™ Maintenance/Metabolism Medium Supplement (5X)	Life Technologies, Eugene, USA
HepaRG™ Thaw, Plate, & General Purpose Medium Supplement (5X)	Life Technologies, Eugene, USA
High-Capacity cDNA Reverse Transcription Kit	Applied Biosystems, Waltham, USA
ibidiTreat µ-slides	Ibidi GmbH, Munich, Germany
JC-1	Thermo Fisher, Waltham, USA
L-Glutamine	Sigma-Aldrich, Taufkirchen, Germany
Lipofectamine™ 3000 transfection reagent	Thermo Fisher, Waltham, USA
Live Cell Imaging Solution	Life Technologies, Eugene, USA
LysoTracker-Red™ DND-99	Thermo Fisher, Waltham, USA
MicroAmp® Fast Optical 96-Well Reaction Plate, 0.1 mL	Applied Biosystems, Waltham, USA
MicroAmp® Optical Adhesive Film	Applied Biosystems, Waltham, USA
Millipore Express® PLUS membrane filter (0.22 µM)	Merck Millipore, Darmstadt, Germany
MitoTracker™ Green FM	Thermo Fisher, Waltham, USA
Nitrocellulose membrane (0.2 µM)	Hybond-ECL™, Amersham Bioscience, Freiburg, Germany
Non-fat dry milk powder	Carl Roth, Karlsruhe, Germany
Page Ruler™ Prestained Protein Ladder	Fermentas, St. Leon-Rot, Germany
Penicillin/Streptomycin 100x	PAA Laboratories, Pasching, Austria
peqGOLD agarose, universal	VWR international, Radnor, USA

Reagent	Producer
Phenylmethylsulfonyl fluoride (PMSF)	Sigma-Aldrich, Taufkirchen, Germany
Phusion Green Hot Start II High-Fidelity Polymerase	Thermo Fisher, Waltham, USA
PlasmidSafe buffer (10X)	Lucigen, Wisconsin, USA
PlasmidSafe Exonuclease	Lucigen, Wisconsin, USA
Polyacrylamide	Carl Roth, Karlsruhe, Germany
Poly-D-lysine hydrobromide (mol wt 70,000-150,000)	Sigma-Aldrich, Taufkirchen, Germany
Polyvinylidene difluoride (PVDF) membrane (0.2 µM)	Hybond-ECL™, Amersham Bioscience, Freiburg, Germany
PowerUp™ SYBR® Green Master Mix	Applied Biosystems, Waltham, USA
Primers	metabion, Planegg, Germany
Puromycin	Sigma-Aldrich, Taufkirchen, Germany
Q5® High-Fidelity DNA Polymerase	New England Biolabs, Ipswich, USA
QIAGEN Miniprep and Maxiprep kits	QIAGEN, Hilden, Germany
RNeasy® Mini Kit (250)	QIAGEN, Hilden, Germany
RPMI 1640	PAN Biotech, Aidenbach, Germany
RPMI 1640 without phenol red	PAN Biotech, Aidenbach, Germany
Seahorse XF Glycolysis Stress Test Kit	Agilent Technologies, Santa Clara, USA
Seahorse XFe96 FluxPaks (inc. mini)	Agilent Technologies, Santa Clara, USA
Sodium chloride	Carl Roth, Karlsruhe, Germany
Sodium fluoride (NaF)	Merck, Darmstadt, Germany
Sodium orthovanadate (Na ₃ VO ₄)	ICN, Biomedicals, Aurora, OH, USA
Sodiumdodecylsulfate (SDS)	Carl Roth, Karlsruhe, Germany
T4 DNA ligase and ligation buffer	Thermo Fisher, Waltham, USA
T7 DNA Endonuclease I and buffers	New England Biolabs, Ipswich, USA
Tris Base	Sigma-Aldrich, Taufkirchen, Germany
Trypsin	PAN Biotech, Aidenbach, Germany
Tween 20	Sigma-Aldrich, Taufkirchen, Germany
William's E Medium (1X)	Life Technologies, Eugene, USA

Table 2 | Reagents

3.1.3 Technical equipment

Device	Producer
BD FACS Canto II	BD Biosciences
ChemiDoc™ Touch Imaging System	Bio-Rad Laboratories GmbH
E plate 16 well	ACEA Biosciences
Ficoll-Paque™ PLUS density gradient medium and PLUS solution	GE Healthcare
Leica Dmil microscope	Leica Microsystems
Leica TCS SP8 confocal laser scanning microscope	Leica Microsystems
Millipore Express® PLUS membrane filter	Merck Millipore
Nanodrop® Spectrophotometer	PEQLAB Biotechnologie GmbH
Orion II microplate Luminometer	Berthold Detection Systems GmbH
Primus 25 advanced® Thermocycler	PEQLAB Biotechnologie GmbH
QuantStudio™ 3 Real-Time PCR System	Applied Biosystems
RTCA device	ACEA Biosciences
Seahorse XF®96 Analyzer	Agilent Technologies
SpectraFluor Plus™	Tecan

Table 3 | Technical equipment

3.2 Cell culture

3.2.1 Cell culture buffers and solutions

PBS (pH 7.4)		Trypsin/EDTA (T/E)	
NaCl	132.2 mM	Trypsin	0.05 %
Na ₂ HPO ₄	10.4 mM	EDTA	0.02 %
KH ₂ PO ₄	3.2 mM	PBS	
H ₂ O			

PBS+Ca ²⁺ /Mg ²⁺ (pH 7.4)		Thaw, plate and general medium (HepaRG™ cells)	
NaCl	137 mM	HepaRG™ Thaw, Plate, & General Purpose Medium Supplement	1 bottle
KCl	2.68 mM	GlutaMAX™ Supplement	5 mL
Na ₂ HPO ₄	8.10 mM	William's E Medium (1X)	500 mL
KH ₂ PO ₄	1.47 mM		
MgCl ₂	0.25 mM		
H ₂ O			

Growth medium		Maintenance and differentiation medium (HepaRG™ cells)	
DMEM/RPMI 1640	500 mL	HepaRG™ Maintenance/Metabolism Medium Supplement (5X)	1 bottle
FCSgold	50 mL	GlutaMAX™ Supplement	5 mL
		William's E Medium (1X)	500 mL
Freezing medium (HUH7 cells)		Collagen G	
DMEM/RPMI 1640	70 %	Collagen G	0.001 %
FCSgold	50 mL	PBS	
DMSO	10 %		

Table 4 | Cell culture buffers and solutions

3.2.2 Cell lines

HepG2, HEK293 (ACC 305) and MCF7 cells were obtained from German Research Centre of Biological Material (DSMZ). HCT-15 cells were purchased from ATCC. HUH7 cells were obtained from Japanese Collection of Research Bioresources (JCRB). RIL175 cells were kindly provided by Prof. Simon Rothenfußer (Center of Integrated Protein Science Munich (CIPS-M) and Division of Clinical Pharmacology, Department of Internal Medicine IV, Klinikum der Universität München, Munich, Germany). T24 cells were obtained from Dr. B. Mayer (Surgical Clinic, LMU, Munich). MDA-MB-231 cells were purchased from Cell Line Service Eppelheim. Vincristine-resistant (VCR-R) CEM cells were a kind gift from Prof. Maria Kavallaris (University of New South Wales, Australia). VCR-R CEM cells that are mainly resistant to vincristine, but also cross-resistant to a variety of other antitumor agents, were generated and described by Haber and coworkers⁷⁰. Sorafenib-resistant HUH7 cells were generated by Maximilian Ardelt and Martina Meßner (Prof. Pachmayr, PMU Salzburg).

HepG2, HUH7, MCF7, MDA-MB-231, RIL175 and T24 cells were cultured in Dulbecco's Modified Eagle Medium (DMEM), supplemented with fetal calf serum (FCS, 10 %, PAA Laboratories). HCT-15 and VCR-R CEM cells were cultured in RPMI 1640, supplemented with fetal calf serum (FCS, 10 %).

Human umbilical vein endothelial cells (HUVECs) were purchased from Promocell and cultivated with ECGM Kit enhanced (PELO Biotech) supplemented with 10% (FCS) and

1% penicillin/streptomycin/amphotericin B (all purchased from PAN Biotech). HUVECs were cultured for a maximum of six passages.

Between thawing and seeding, HepaRG[®] cells were cultivated in thaw, plate and general medium. For differentiation, HepaRG[®] cells were seeded in 6 well plates at a density of 0.5×10^6 cells per well in 2 mL of maintenance and differentiation medium for 7 days. Maintenance and differentiation medium was exchanged twice per week.

All cells were cultured at 37 °C at constant humidity with 5% CO₂. Before seeding of adherent cells, all culture flasks, multiwell plates and dishes were coated with collagen G (0.001 % in PBS).

PBMCs were isolated and cultured as described in **3.24**.

3.2.3 Passaging

When cells nearly reached confluency, they were split 1:2-1:10 and sub-cultured in 75 cm² culture flasks or seeded in multiwell plates or dishes for further experimental use. For passaging, culture medium was aspirated, cells were washed with pre-warmed PBS and detached by incubation with pre-warmed trypsin/ethylenediaminetetraacetic acid (EDTA) (T/E) solution for 3-5 min at 37 °C. Thereafter, culture medium was added to stop tryptic digestion and T/E solution was removed by centrifugation (1000 rpm, 5 min, 20 °C) and addition of new culture medium.

3.2.4 Freezing and thawing

Before freezing, cells were cultured to reach confluency in a 150 cm² flask. Washing and cell detachment was conducted as described in **3.2.3**. After centrifugation (1000 rpm, 5 min, 20 °C), cells were re-suspended in ice-cold freezing medium and transferred into cryovials at a cell density of 3×10^6 cells per 1.5 mL aliquot. Following an initial storage at - 80 °C for at least 24 h, cryovials were transferred into liquid nitrogen tanks (- 196 °C) for long-term storage.

For thawing, the cryovial content was mixed with pre-warmed culture medium. After DMSO removal by centrifugation (1000 rpm, 5 min, 20 °C), the cell pellet was re-suspended in culture medium and initially transferred into a 25 cm² flask for 24 h before cells were cultured in a 75 cm² flask.

3.3 Apoptosis assays

VCR-R CEM cells were seeded at a density of 0.125×10^6 cells per well of a 24 well plate and incubated for 4 h at 37 °C. Treatment was performed with the indicated concentrations for 48 h. Apoptosis was determined by propidium iodide staining as described before (Nicoletti et al.) on a BD FACS Canto II (BD Biosciences). Briefly, cell suspensions were transferred into pre-cooled FACS tubes, centrifuged for 5 min at 400 g, washed with an equal volume of ice-cold PBS, centrifuged again for 5 min at 400 g, and resuspended in 250 μ L ice-cold hypotonic fluorochrome solution (**Table 5**). Cells were kept in the dark at 4 °C for at least 30 min prior to flow cytometric analysis.

Hypotonic fluorochrome solution (HFS)	
sodium citrate	0.1 % (w/v)
Triton X-100	0.1 % (v/v)
propidium iodide	50 μ g/ml
H ₂ O	

Table 5 | Composition of the hypotonic fluorochrome solution.

3.4 Calcein-AM retention assay

Calcein-AM is a P-gp substrate and can be actively transported from the plasma membrane by P-gp. Once it has entered the cytosol, it is cleaved by cellular esterases and becomes fluorescent. Thus, calcein-AM can be used to monitor P-gp activity. The protocol was adapted from Robey and coworkers³⁴. VCR-R CEM cells were seeded at a density of 0.3×10^6 cells per 1 mL per well of a 12 well plate and incubated for 4 h at 37°C. Subsequently, calcein-AM (Biomol) (200 nM) and the potential P-gp inhibitors were added and incubated for 30 min at 37 °C. After incubation, cells were centrifuged (400 g, 5 min), washed with PBS and resuspended in 0.5 mL RPMI 1640 without phenol red (PAN Biotech) containing the respective concentration of the P-gp inhibitor. Following a 60 min incubation time at 37 °C, calcein fluorescence was analyzed by flow cytometry on a BD FACS Canto II (BD Biosciences) and fluorescence intensities were normalized to the DMSO control using FlowJo 7.6 (BD Biosciences).

3.5 Cellular uptake assay

Cellular uptake of tetrandrine, SG-005 and SG-094 were determined by HPLC-DAD. RIL175 WT and HUVECs were incubated with these compounds at 2 and 10 μ M. RIL175 WT and HUVEC cells were seeded at a density of 0.3×10^6 cells per well of a 6-well plate

and allowed to adhere overnight. Cells were treated with 2 and 10 μM of the respective compounds for 75 min. Before trypsinization with 2X T/E, cells were washed twice with PBS (2 mL). For normalization, cells were counted using a ViCell XR cell counter (Beckman). After harvesting, cell pellets were centrifuged (table centrifuge, 13,000 rpm, 5 min, 4 °C), washed with ice-cold PBS (1 mL), centrifuged (table centrifuge, 13,000 rpm, 5 min, 4 °C) and resuspended in 50 μL acetonitrile. For cell lysis by bead beating, glass beads (acid-washed, Sigma Aldrich) were added and cell lysis was conducted by shaking on an orbital shaker at 4 °C for at least 30 min. Reaction mixtures were centrifuged again (table centrifuge, 13,000 rpm, 5 min, 4 °C). The supernatants (40 μL) were subjected to analytical HPLC analysis, which was performed by Anna Niedrig and Christoph Müller (Prof. Bracher, LMU Munich). The supernatant was analyzed by HPLC-DAD using an Agilent Series 1100 HPLC system (Agilent Technologies) consisting of a quaternary pump system (G1311 A QuatPump), an autosampler (G1329 A ALS), a column oven (G1316 A ColComp) and a UV-DAD detector (G1315 A DAD). Chromatographic separation was carried out with an Agilent Zorbax Eclipse Plus C18 (150 \times 4.6 mm, i.d. 5.0 μm) column (Agilent Technologies) and a mobile phase of methanol and water (adjusted with 1 M sodium hydroxide solution to pH 9) 80:20 (v/v). The total run time was 18 min with an isocratic flow rate at 1.2 mL/min, and an injection volume of 10 μL . The column oven was set at 30 °C. The UV detection wavelength was set at 210 nm. Data analysis and instrument control was carried out with Agilent ChemStation[®] software Rev. B04.02 (Agilent Technologies). The retention time of tetrandrine was 4.5 min, of SG-005 was 10.4 min, and of SG-094 10.0 min. The concentration of each compound was determined according to an external standard calibration.

3.6 CYP3A4 P450-Glo[™] assay

Metabolic activity of CYP3A4-EGFP was confirmed using a CYP3A4 P450-Glo[™] assay (Promega, Madison, USA). HepG2 cells were seeded at a density of 0.75×10^6 cells per well into a 24 well plate and allowed to adhere overnight. On the following day, cells were transfected with either pcDNA3-CYP3A4-EGFP or pcDNA3-EGFP using the Lipofectamine[™] 3000 (Invitrogen, Waltham, USA) transfection reagent according to the manufacturer's instructions. On the subsequent day, cells were incubated with luciferin-IPA (3 μM) in the presence or absence of ketoconazole (Santa Cruz biotechnology, Dallas, USA) (10 μM) for 60 min. The non-lytic method was used as described by the manufacturer. Briefly, 150 μL of each well were transferred into to a plate suitable for

luminescence measurement. Luminescence at 560 nm was recorded with an Orion II Microplate Luminometer (Berthold Detection Systems).

3.7 Endolysosomal patch clamp method

All endolysosomal patch clamp experiments were conducted by Yu-Kai Chao (Prof. Grimm, LMU Munich) with the aim to either confirm genetic TPC2 knockout or to quantify the inhibitory potential of TPC2 blockers. For confirmation of loss of channel function in RIL175 cells, whole endolysosomal patch clamp recordings were conducted using modified conventional patch clamp. RIL175 cells were treated with YM201636 (800 nM) for at least 2 h. Intact endolysosomes were isolated and current recordings and data analysis were performed as described before⁷¹. For confirmation of loss of channel function in VCR-R CEM cells, cells were immobilized on microscope cover slips in a 24 well plate using Corning® Cell-Tak™ Cell and Tissue Adhesive (Corning) according to the absorption method protocol provided by the manufacturer. Briefly, approximately 3.5 µg/cm² (7 µg/well) Cell-Tak™ reagent were diluted in 250 µl 0.1 M bicarbonate buffer pH 8 per well. Prior to immobilization, cells were treated with 1 µM vacuolin-1 (Sigma Aldrich) overnight in order to enlarge lysosomes and 50,000 cells/well were seeded. For determination of the inhibitory effect of benzylisoquinolines on TPC2, human TPC2 (C-terminally fused to YFP) was transiently transfected into HEK293 cells TurboFect Transfection Reagent (Thermo Fisher). Isolation of intact endolysosomes from HEK293 cells after vacuolin treatment for at least 2 h, current recordings and data analysis were performed as described previously⁴. 10 µM of each inhibitor and 1 µM of PI(3,5)P₂ were applied. Inhibition percentage was calculated as follows: *inhibition percentage (%)* =

$$100 \% - \frac{\text{current (PI(3,5)P}_2\text{ + inhibitor)}}{\text{current (PI(3,5)P}_2\text{)}} \times 100 \%$$

3.8 Fura-2 Ca²⁺ imaging

Single cell Ca²⁺ imaging experiments were performed by Susanne Gerndt (Prof. Bracher, LMU Munich) using Fura-2. HEK293 stably expressing TPC2^{L11A/L12A}-RFP⁶ were cultured at 37 °C with 5 % of CO₂ in Dulbecco's modified Eagle medium (Thermo Fisher), supplemented with 10 % fetal bovine serum, 100 U/mL penicillin, and 0.1 mg/mL streptomycin. Cells were plated onto poly-L-lysine (Sigma Aldrich)-coated glass coverslips and grown for 2-3 days. For Ca²⁺ imaging experiments, cells were loaded for 1 h at room temperature with Fura-2 AM (4.0 µM) and 0.005 % (v/v) pluronic acid (both from Thermo Fisher) in HEPES-buffered solution 1 (HBS1) comprising 138 mM NaCl, 6 mM KCl, 2 mM

MgCl₂, 2 mM CaCl₂, 10 mM HEPES, and 5.5 mM D-glucose (adjusted to pH 7.4 with NaOH). After loading, cells were washed in HBS, and mounted in an imaging chamber. All recordings were performed in HBS1. Calcium imaging was performed using a Leica DMI8 live cell microscope. Fura-2 was excited at 340 nm/380 nm. Emitted fluorescence was captured using 515 nm long-pass filter. Compounds were pre diluted in DMSO and stored as 10 mM stock solutions not exceeding three months. Working solutions were prepared directly before using by dilution with HBS.

3.9 Fluo-4 Ca²⁺ imaging

Fluo-4 based calcium imaging experiments were performed by Nicole Urban (Prof. Schäfer, Leipzig University) using a custom-made fluorescence imaging plate reader built into a robotic liquid handling station (Freedom Evo 150, Tecan, Männedorf, Switzerland). HEK293 stably expressing TPC2^{L11A/L12A}-RFP⁶ were cultured at 37 °C with 5 % of CO₂ in Dulbecco's modified Eagle medium (Thermo Fisher), supplemented with 10 % fetal calf serum (Biochrom, Berlin, Germany), 2 mM L-glutamine, 100 U/mL penicillin, 0.1 mg/mL streptomycin, and 400-800 µg/mL G418. Cells were seeded on black-walled, clear-bottom 384-well plates (Greiner, Germany) and incubated with Fluo-4 AM (4 µM; Life Technologies, Eugene, OR) for 30 minutes at 37 °C, washed and resuspended in HEPES-buffered solution 2 (HBS2) comprising 132 mM NaCl, 6 mM KCl, 1 mM MgCl₂, 1 mM CaCl₂, 10 mM HEPES, and 5.5 mM D-glucose (adjusted to pH 7.4 with NaOH). For concentration-effect experiments cells were sequentially stimulated with different concentrations of inhibitor (0.1 to 100 µM) and the novel TPC2 activators TPC2-A1-N and TPC2-A1-P⁶ (10 µM each). Concentration-effect relationships were plotted using GraphPad Prism 5 and fitted to the Hill equation.

3.10 FLIM-FRET imaging

A Förster resonance energy transfer (FRET)-based fluorescent ATP probe, named GO-ATeam, was recently developed by Nakano et al and coworkers⁷² for ATP imaging in single living cells, in which the ε subunit of the bacterial F₀F₁-ATP synthase is sandwiched between a green fluorescent protein (GFP, cp173-mEGFP) and an orange fluorescent protein (OFP, mKOκ) that are used as a FRET pair⁷². Specific binding of ATP to the ε subunit 13 in GO-ATeam induces the conformational change of the ε subunit from extended to retracted form, and thereby FRET efficiency in GO-ATeam increases, enabling the monitoring of ATP concentrations in living cells at a subcellular spatial resolution⁷². The use of the current GO-ATeam probe⁷² offers several advantages over

the originally developed ATeams⁷³. Specifically, the signal is more stable against acidification, which allows ATP imaging inside acidic intracellular compartments⁷². Also, the GO-ATeam longer excitation wavelength is much less phototoxic to cells, making the probe suitable for longer times of observation⁷². The dynamics of intracellular ATP levels in RIL175 hepatocellular carcinoma cells transfected with the GO-ATeam probe were successfully visualized. In these experiments, higher ATP levels correspond to higher FRET efficiency as defined by the differences in the lifetime of the GO-ATeam probe. Furthermore, sequential false colour Heatmap images for each time point showing the distribution of ATP, via FRET efficiency, inside the cells were generated. Specifically, two separate data sets comparing the differences in ATP levels were collected, one between RIL175 WT and RIL175 TPC2 KO cells and the other between SG-005 pre-treated or non-treated RIL175 WT cells. For that purpose, RIL175 WT and TPC2 KO cells were seeded at different densities ranging from 0.5 to 2×10^4 cells per well of ibidi 8 well μ -slides with glass bottoms (ibidi) and incubated overnight. Before imaging, cells were supplemented with new DMEM (PAN Biotech), supplemented with 10 % fetal calf serum (FCS) (PAA Laboratories). To determine the influence of SG-005 on ATP levels, RIL175 WT cells were treated with SG-005 (2 μ M) or vehicle for 1 h prior to imaging. For the comparison of RIL175 WT and TPC2 KO cells, cells were left untreated. FLIM (fluorescence lifetime imaging)-FRET measurements were performed by Themistoklis Zisis (Prof. Vollmar, LMU Munich) on a Leica TCS SP8 SMD microscope combined with a Picoquant LSM Upgrade Kit using a 470 pulse laser at 40 MHz frequency and a time-correlated single-photon counting (TCSPC) approach (SI). For all measurements, a 63x Zeiss water immersion lens was used. A complete FLIM image of single cells was recorded until an average of 1000 photon counts per pixel was collected. The fluorescence decay curve was calculated from the recorded FLIM image that was then analyzed by deconvolution fit using the instrument response function (IRF). This process was repeated for twelve different timepoints (0, 10, 20, 30, 35, 40, 45, 60, 75, 90, 105 and 120 min) with 5 mM of 2-deoxy-D-glucose (2-DG) (Sigma Aldrich) being added after the 30 min timepoint measurement. Data acquisition and analysis was performed using the Picoquant SymPhoTime 64 (V2.1). In control experiments, the fluorescence decay time of the donor in absence of the acceptor (τ_D) was determined by applying a single-exponential decay function. For the FRET samples, a bi-exponential fit function was assumed. Here, the first time component was fixed according to τ_D previously obtained from the control experiments and reflecting the non-interacting donor fraction and the second time component τ_{DA} was freely fitted reflecting the donor fraction interacting with the acceptor. The quality of the fit was

assessed by randomly distributed residuals and by low χ_R^2 values. From the interacting fraction, the FRET efficiency (E) was calculated according to: $E = 1 - \frac{\tau_{DA}}{\tau_D}$.

3.11 Generation of a RIL175 TPC2 knockout cell line using CRISPR-Cas9

3.11.1 sgRNA design and cloning of constructs

The knockout of *TPCN2* in murine RIL175 cells with the CRISPR-Cas9 system was conducted as described earlier^{74, 75}. As a strategy, we aimed to delete exon 2 of *TPCN2* after having sequenced the region of interest (*TPCN2* sequencing primer: 5'-CCACATTTACCTCATGACATCC-3'). As a template, genomic DNA from RIL175 WT cells which was isolated using the QuickExtract™ DNA Extraction Solution (Lucigen) according to the manufacturer's instructions was used. Then, single guide RNAs (sgRNAs) were designed as described previously⁷⁶. Three sgRNAs upstream (5') of exon 2 (**Table 6**) were used for cloning into the eCas9(1.1)-2A-Puro backbone (cloned by introducing the T2A puromycin resistance cassette from PX549 into eSpCas9(1.1) via FseI and NotI; both plasmids were a gift from Feng Zhang, addgene plasmids #62988 and #71814, respectively). Similarly, two sgRNAs downstream (3') of exon 2 (**Table 6**) were designed to be cloned into the eSpCas9_2A_Blasti plasmid (provided by Lars König, Klinikum der Universität München, Munich, Germany).

Name	Sequence (5'-3')
5' TPC2_676/rev_top	CACCGTCTACTAACAGGGCACGTGC
5' TPC2_676/rev_bottom	AAACGCACGTGCCCTGTTAGTAGAC
5' TPC2_794/rev_top	CACCGTAGAGGCAGCGCTAGTCCA
5' TPC2_794/rev_bottom	AAACTGGACTAGCGCTGCCTCTAC
5' TPC2_857/rev_top	CACCGCCGGGCCAGAGTCCCAATC
5' TPC2_857/rev_bottom	AAACGATTGGGACTCTGGCCCGGC
3' TPC2_237/fw_top	CACCGACAGTCTTAGCCCGTGCCAA
3' TPC2_237/fw_bottom	AAACTTGGCACGGGCTAAGACTGTC
3' TPC2_386/rev_top	CACCGCTGTACCAGCACACTACATG
3' TPC2_386/rev_bottom	AAACCATGTAGTGTGCTGGTACAGC

Table 6 | sgRNA sequences/cloning oligomers

Before cloning, oligomers were annealed using a PCR cycler (5 min at 95 °C, ramp down to 25 °C) and diluted (1:100 in RNase-free H₂O) (**Table 7**).

Reagent	Volume [μ l]
sgRNA_top (100 μ M)	1
sgRNA_botom (100 μ M)	1
T4 ligation buffer	1
RNase-free H ₂ O	7

Table 7 | Oligo annealing reaction mix.

For insertion of the annealed oligos into the respective Cas9 plasmid, the Cas9 plasmids were digested using FastDigest (FD) Bpil (Thermo Fisher) for 30 min at 37 °C (**Table 8**).

Reagent	Volume [μ l]
Cas9 plasmid (150 ng)	x
FD Buffer colorless (10X)	1.5
FD Bpil	1
RNase-free H ₂ O	ad 15

Table 8 | Digestion of Cas9 plasmids.

Annealed oligos and digested Cas9 plasmids were ligated using the T4 DNA ligase (Thermo Fisher) for 30 min at room temperature (**Table 9**).

Reagent	Volume [μ l]
digested Cas9 plasmid	10
annealed oligos (1:100 dilution)	2
T4 ligation buffer (10X)	2
T4 DNA ligase	1
RNase-free H ₂ O	5

Table 9 | Ligation of annealed oligos and Cas9 plasmids.

Non-ligated plasmid was removed using the PlasmidSafe ATP-dependent DNase (Lucigen) by incubation for 30 min at 37 °C and for 30 min at 70 °C (**Table 10**).

Reagent	Volume [μ l]
Ligation reaction	11
PlasmidSafe buffer (10X)	1.5
ATP (25 mM)	0.6
PlasmidSafe Exonuclease	1
H ₂ O	ad 15

Table 10 | Components used for digestion of non-ligated plasmid.

Subsequently, the constructs were transformed into competent DH5 α -E. coli (prepared in-house) (3-10 μ L construct per 100 μ L E. coli). After addition of plasmid DNA, E. coli were first kept on ice for 10 min before being heat-shocked at 42 °C for 45 s and returned to ice for 2 min. Bacterial suspensions were then plated on agar plates containing ampicillin and incubated overnight at 37 °C. On the next day, 3-5 colonies were picked per plasmid and amplified in 5 mL LB(+) medium containing 100 μ g/ml ampicillin. Then plasmids were prepared using the QIAGEN Plasmid Miniprep and Maxiprep Kits (QIAGEN) according to the manufacturer's instructions. Correct insertions were confirmed by restriction digestion and by Sanger sequencing starting from the U6 promoter.

3.11.2 Transfection and evaluation of genome targeting efficiency

Before being transfected with the respective plasmids, RIL175 WT cells were cultured in 6 well plates to a confluence of 60-70 %. Subsequently, RIL175 WT cells were transfected with three pairs of sgRNAs using Lipofectamine™ 3000 (Invitrogen) transfection reagent according to the manufacturer's instructions (7.5 μ L Lipofectamine™ 3000 reagent). 24 h later, selection was performed with puromycin (2 μ g/mL) and blasticidin S (6 μ g/mL) for 72 h. After removal of puromycin and blasticidin S, cells were allowed to recover until reaching sufficient confluency. By applying the T7 DNA Endonuclease I assay (New England Biolabs), the sgRNA pair with the highest editing efficiency was determined (5' TPC2_676/rev and 3' TPC2_237/fw, data not shown) according to the manufacturer's instructions (primers used for PCR: TPC2_5'_T7_FW: 5'-ATTCTGGCTGAACAGGAGGC-3', TPC2_5'_T7_RV: 5'-ACAGACAGCACAGCCTCATC-3', TPC2_3'_T7_FW: 5'-ACACATGAAGCCAGCTCTCC-3', TPC2_3'_T7_RV: 5'-GTCTCTCCACATCTCGCTCG-3',) and used for subsequent single cell dilution and clonal expansion. For single cell dilution, cells were detached, cell aggregates were separated with a cell strainer and adjusted to a cell density of 0.6 cells/well before being seeded into 96 well plates. Subsequently, cells were transferred into 24 well plates for upscaling before isolation of DNA.

3.11.3 Single cell dilution, clonal expansion and knockout verification

Successful exon 2 deletion was confirmed by standard PCR (Thermo Scientific Phusion Green Hot Start II High-Fidelity Polymerase, Thermo Fisher), agarose gel analysis (peqGOLD agarose, universal, VWR International) and sequencing (**Table 11**).

Name	FW primer (5'-3')	RV primer (5'-3')
TPC2 within ex2	AGGGTCTCTGGCTGCAGACA	ACCTAGCACAGGGTAGCCCA
TPC2 spanning ex2	GGTGTTGTAGCTTGGCTAGGT	AGCATCCATGCGGTGGTA
TPC2 sequencing	CCACATTTACCTCATGACATCC	-

Table 11 | Primers used for PCR analysis of exon 2 deletion.

3.11.4 Off-target screening

The ten predicted off-target sequences present in exons or introns with the highest cutting frequency determination (CFD) scores according to the CRISPOR TEFOR *in silico* tool⁷⁶ for each sgRNA were amplified by PCR (Thermo Scientific Phusion Green Hot Start II High-Fidelity Polymerase, Thermo Fisher or Q5[®] High-Fidelity DNA Polymerase, New England Biolabs), analyzed by Sanger sequencing and compared with the WT control. The investigated off-targets, sequences and the used primer pairs and polymerases are listed in **Supplementary Table 1** and **Supplementary Table 2**. Cloning oligos and sequencing services were provided by Eurofins Genomics. Primers were purchased from Metabion.

3.12 Generation of a VCR-R CEM TPC2 knockout cell line using CRISPR-Cas9

An InDel mutation was introduced near the human TPC2 M484L SNP⁷⁷ in VCR-R CEM cells. *In silico* design and cloning into the eCas9(1.1)-2A-Puro plasmid were performed as described in **3.11.1 (Table 12)**.

Name	Sequence (5'-3')
sgRNA3_top	CACCGACCCCAGCAACGTGTTTGAC
sgRNA3_bottom	AAACGTCAAACACGTTGCTGGGGTC

Table 12 | hTPC2 sgRNA top and bottom sequences.

VCR-R CEM cells were transfected with the plasmid construct using nucleofection (Amaxa Nucleofector Kit C, VACA-1004, Lonza) using the program X-005 and 6 µg of the plasmid construct according to the manufacturer's instructions. To increase transfection efficiency, a 10 min post-incubation step at room temperature was included. Selection was performed with puromycin (2.5 µg/ml) for 72 h. After a recovery of 5 days, single cell dilution and clonal expansion was performed as described in **3.11.3**. Standard PCR (Thermo Scientific Phusion Green Hot Start II High-Fidelity Polymerase, Thermo Fisher), agarose gel analysis (peqGOLD agarose, universal, VWR International) and sequencing were performed to detect InDel mutations (**Table 13**).

Target	FW primer (5'-3')	RV primer (5'-3')
hTPC2_PCR	TCGGCCACTACTACTTTGAC	GTAGAAACCCAGCCTCCTAA
hTPC2 sequencing	TCGGCCACTACTACTTTGAC	-

Table 13 | Primers used to detect InDels.

The screening for potential off-targets is described in Franz Geisslinger's Master Thesis (Prof. Vollmar, LMU Munich).

3.13 *In vivo* experiments

All animal experiments were performed by Carina Ortler and Kerstin Loske (Prof. Vollmar, LMU Munich), and approved by the District Government of Upper Bavaria, in accordance with institutional guidelines and the German Animal Welfare. C57Bl/6-Tyr mice could be used as RIL175 cells originate from them. To enable *in vivo* bioluminescence imaging of RIL175 cells that contain a stable luciferase knock-in, the albino phenotype was necessary.

Dissemination assay. 20 C57Bl/6-Tyr mice (Envigo), female, 6 weeks old, were used for intravenous injection of either 2×10^5 RIL175 WT or TPC2 KO cells into the tail vein. Bioluminescence imaging using the IVIS Lumina system (PerkinElmer) was conducted on day 3 after intraperitoneal injection of 6 mg/mL luciferin per mouse. Previously, mice were put under anesthesia with 3 % isoflurane in oxygen. Imaging of mice was performed in ventrodorsal position and mice were kept under narcosis with 2 % isoflurane in oxygen. Hypothermia was prevented by a heating plate (37°C). The tumor signal per defined region of interest was calculated as photons/second/cm² (total flux/area) using the Living Image 4.4 software (Perkin Elmer).

Dose-finding test. Initially, for determination of the doses of SG-005 and SG-094, 12 female C57Bl/6-Tyr mice (Envigo), 6 weeks old, were used. SG-005 was applied at 38 nmol/kg and 57 nmol/kg and SG-094 at 59 nmol/kg and 90 nmol/kg daily on three consecutive days. Compounds were dissolved in a solvent consisting of 5 % DMSO, 10 % solutol and 85 % PBS and they were injected intraperitoneally (100 μ L injection volume). Due to the known toxicity problems of tetrandrine in the literature, the compound was not used *in vivo*.

Ectopic tumor model. 40 C57Bl/6-Tyr mice (Envigo), female, 5 weeks old, were injected with either 2×10^6 RIL175 WT or TPC2 KO cells into the flank. Treatment of mice with vehicle control, SG-005 (57 nmol/kg) or SG-094 (90 nmol/kg) was performed on day 0, 2, 4, 7 and 9 after implantation of cells. Compounds were dissolved as described for the

dose-finding test. Tumor volumes were measured by caliper on day 4, 7, 9 and 10 and calculated with the formula $\pi/6 \times L \times W \times H$. Bioluminescence imaging was performed on day 2, 4, 7 and 10 after implantation of cells following intraperitoneal injection of 6 mg/mL luciferin per mouse. Anesthesia, narcosis and calculation of tumor signal per defined region were performed as described for the dissemination assay. Tumors were resected and stored at -80 °C.

Immunoblotting of tumors. For Western blot analysis, 100 μ l RIPA buffer (**3.19, Table 17**) without additives were added per 10 mg of tumor tissue derived from the ectopic tumor model. Samples were homogenized using a potter homogenizer (Carl Roth) on ice. Then, samples were centrifuged (table centrifuge, 14,000 rpm, 10 min, 4 °C) and supernatants were isolated for determination of protein concentration as determined in **3.19**. For dephosphorylation, 50 μ l FastAP™ Thermosensitive Alkaline Phosphatase (1 U/ μ L) (Thermo Fisher) and 10 μ L 10X FastAP™ buffer (Thermo Fisher) were used per 20 μ g protein. The reaction mixtures were incubated for 1 h at 37 °C before dephosphorylation was stopped by addition of 20 μ L 5X sample buffer (**3.19, Table 17**) and heat denaturation for 5 min at 95 °C. Gel electrophoresis and immunoblotting were performed as described in chapter **3.19**.

3.14 Lysosomal uptake assay

Lysosomal uptake of tetrandrine, SG-005 and SG-094 was determined by LysoTracker-Red™ DND-99 (Thermo Fisher) staining and flow cytometry as described previously⁵⁰. Briefly, RIL175 WT, RIL175 TPC2 KO and HUVEC cells were seeded at a density of 0.06×10^6 cells per well of a 24-well plate and allowed to adhere overnight. On the subsequent day, cells were treated with 2 and 10 μ M of the respective compounds (or with 10 nM of the V-ATPase inhibitor concanamycin, Santa Cruz Biotechnology) for 60 min. LysoTracker-Red™ DND-99 (25 nM) was present during the last 15 min. Fluorescence was determined on a BD FACS Canto II (BD Biosciences) and fluorescence intensities were normalized to the DMSO control using FlowJo 7.6 (BD Biosciences).

3.15 Mitochondrial mass

To determine mitochondrial mass, RIL175 WT cells were seeded at a density of 0.1×10^6 cells per well of a 24-well plate and allowed to adhere overnight. Cells were either treated with the respective compounds for 1 h or for 24 h at the indicated concentrations. After detachment with 2X T/E, cells were incubated with 250 μ L MitoTracker™ Green FM (Thermo Fisher) in DMEM (PAN Biotech) without supplements for 3 min at 37 °C.

Subsequently, medium was discarded and cells were resuspended in 250 μ L PBS and analyzed by flow cytometry. Forward *versus* side scatter (FSC vs. SSC) gating was used to exclude cell debris as shown below using FlowJo 7.6 (BD Biosciences). MitoTracker™ Green fluorescence was analyzed in the Alexa Fluor 488-A channel on a FACS Canto II (BD Biosciences).

3.16 Mitochondrial membrane potential

The cationic dye JC-1 (Thermo Fisher) was used to monitor mitochondrial health and, more specifically, to measure mitochondrial membrane potential ($\Delta\Psi_m$). When $\Delta\Psi_m$ is intact, JC-1 accumulates in mitochondria, yielding a red fluorescence. In contrast, mitochondrial depolarization is indicated by a decrease in the red/green fluorescence intensity. RIL175 WT cells were seeded at a density of 0.1×10^6 cells per well of a 24-well plate and allowed to adhere for at least 6 h. Subsequently, cells were treated for 1 h or 24 h with the indicated concentrations of the respective compounds. Then, JC-1 (1 μ g/mL) was added and incubated for 1 h. For 1 h treatment with compounds, staining with JC-1 was performed simultaneously. Cells were harvested with 2X T/E, washed with PBS and resuspended in PBS for flow cytometric analysis on a BD FACS Canto II (BD Biosciences). In parallel, compensation samples were prepared using Anti-Mouse Ig, κ /Negative Control (FBS) Compensation Particles Set (BD Biosciences) and a BD PE Mouse IgG1, κ / Isotype Control (BD Biosciences #555749) and a BD Alexa Fluor® 488 Mouse IgG1 κ Isotype Control (BD Biosciences #557721) as described by the manufacturer. Prior to analysis of cellular samples, compensation of spectral overlap was performed on a BD FACS Canto II (BD Biosciences) as indicated below. The percentage of PE-A (orange) and of Alexa-Fluor-488-A positive populations was determined using FlowJo 7.6 (BD Biosciences) as shown in Figure 5.

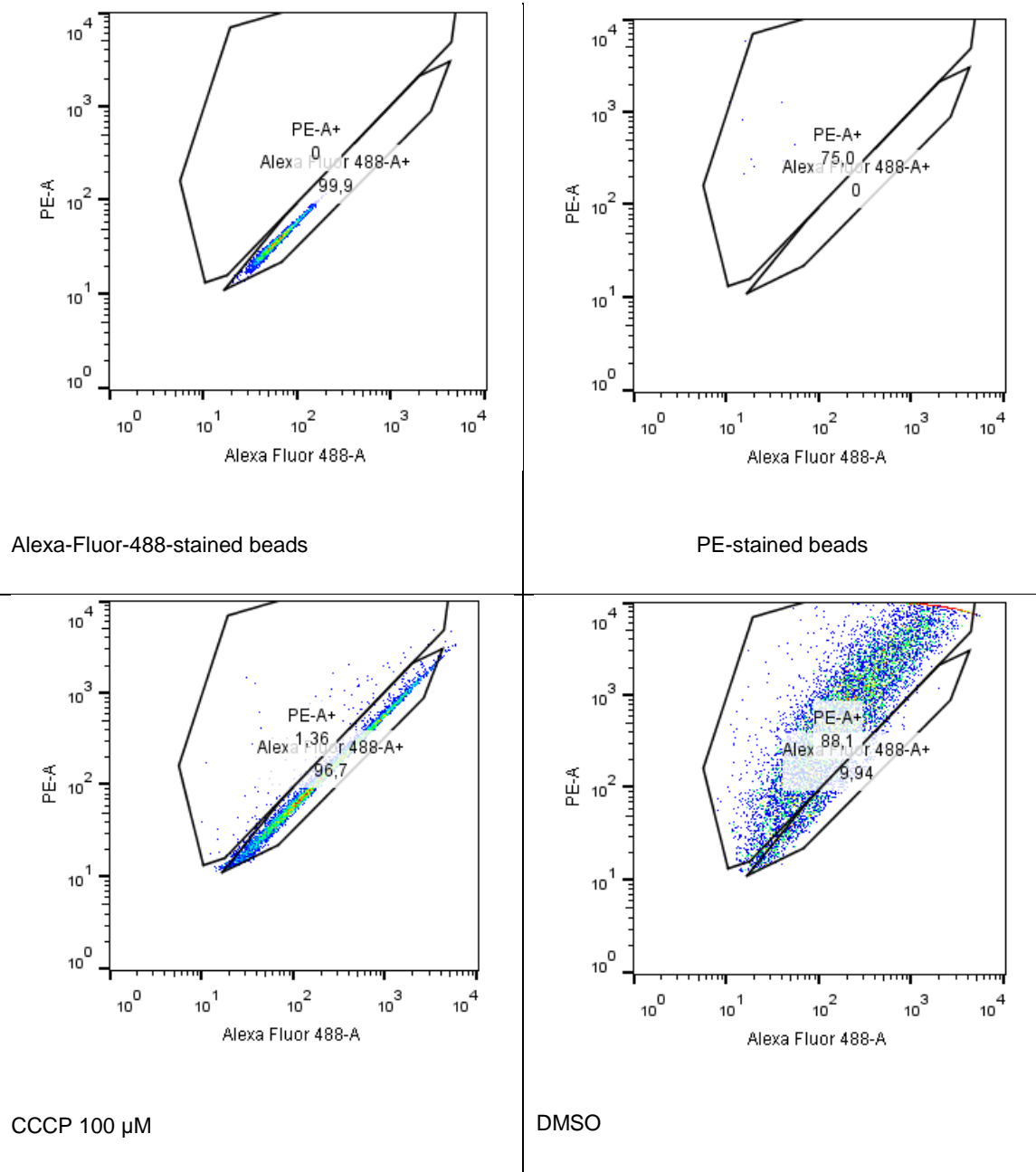


Figure 5 | Gating for PE-A positive and Alexa-Fluor-488-A positive populations after staining with JC-1.

3.17 Molecular cloning of pcDNA3-CYP3A4-EGFP

The cDNA template was generated by isolation of mRNA from HepaRG™ progenitor cells (QIAGEN RNeasy Mini Kit, QIAGEN) and subsequent reverse transcription (High Capacity cDNA Reverse Transcription Kit, Applied Biosystems) as described in 3.22. cDNA was amplified by PCR (Thermo Scientific Phusion Green Hot Start II High-Fidelity Polymerase, Thermo Fisher) (CYP3A4-FW: 5'-ATATATGGTACCGCCACCATGGCTCTCATCCCA-3', CYP3A4-RV: 5'-ATCTCGAGGGCTCCACTTACGGTGCCA-3'). The obtained PCR

product was digested using FastDigest (FD) KpnI, FD XhoI and T4 DNA Ligase (all purchased from Thermo Fisher) as indicated in **Table 14**. The digestion reaction mix was incubated for 30 min at 37 °C and the reaction was stopped by heat denaturation for 15 min at 65 °C.

Reagent	Volume [μ l]
CYP3A4 insert	3
FD Buffer colorless 10X	2
FD KpnI	1
FD XhoI	1
H ₂ O (ad 20 μ L)	13

Table 14 | Restriction digestion mix of CYP3A4 insert.

The pcDNA3-EGFP vector was a gift from Doug Golenbock (Addgene plasmid #13031; <http://n2t.net/addgene:13031>; RRID:Addgene_13031). The vector was digested and dephosphorylated as indicated in **Table 15**. The digestion reaction mix was incubated for 30 min at 37 °C and the reaction was stopped by heat denaturation for 15 min at 65 °C.

Reagent	Volume [μ l]
vector (addgene #13031)	1.2
FD Buffer colorless 10X	2
FD KpnI	1
FD XhoI	1
Fast AP Thermosensitive Alkaline Phosphatase	1
H ₂ O (ad 20 μ L)	14.3

Table 15 | Simultaneous plasmid vector linearization and dephosphorylation

Vector and insert digestion reactions were pooled and then purified using the QIAquick Gel Extraction Kit (QIAGEN) as indicated by the manufacturer and finally eluted with 26 μ L RNase-free water. Ligation of linearized, dephosphorylated pcDNA3.1 and CYP3A4 insert was performed at a 5:1 insert:vector ratio and 200 ng of vector overnight at room temperature as indicated in **Table 16**.

Reagent	Volume [μ l]
mix of digestion reactions	26
T4 ligation buffer (10X)	3
T4 DNA Ligase	1
H ₂ O (ad 30 μ L)	0

Table 16 | Ligation of linearized, dephosphorylated pcDNA3.1 and CYP3A4 insert.

Transformation into competent DH5 α -E.coli and preparation of plasmids was conducted as described in 3.11.1. Correct insertion of the insert was confirmed by PCR, restriction digestion and Sanger sequencing (sequencing primer: hCYP3A4_1_F: 5'-GTATGGAAAAGTGTGGGGCT-3'). Sequencing services were provided by Eurofins Genomics. Primers were purchased from Metabion.

3.18 Proliferation assays

Cellular proliferation of RIL175 WT and TPC2 KO cells was assessed by impedance measurement and by CellTrace™ CFSE staining. Cellular proliferation of VCR-R CEM WT vs. TPC2 KO cells was quantified by cell counting using trypan blue staining on a ViCell XR cell counter (Beckman). Antiproliferative effects of the compounds from the library were determined by CellTiter-Blue® assay.

Impedance measurement. With the xCELLigence RTCA device (ACEA Biosciences), the cell index, a dimensionless parameter that is proportional to the cell number, can be determined through impedance measurement. RIL175 WT and TPC2 KO cells were seeded at a density of 2×10^3 cells per well into an equilibrated 16-well E-plate. Slopes were calculated using the xCELLigence RTCA software (ACEA Biosciences) for each cell line until reaching the plateau phase using the following equation: $Slope \left(\frac{1}{h} \right) = \frac{\text{Cell Index} - \text{intercept}}{\text{time (h)}}$.

CellTrace™ CFSE staining. Additionally, the CellTrace™ CFSE Cell Proliferation Kit (Invitrogen) was used to assess proliferation visually. It relies on a fluorescent CellTrace™ reagent that diffuses into cells and binds covalently to intracellular amines. Cell proliferation can be followed by flow cytometry for several generations. Labelling of the cells was conducted as indicated by the manufacturer using 10 μ M CFSE. CFSE fluorescence was analyzed directly after labelling and after a 72 h incubation time by flow cytometry on a BD FACS Canto II (BD Biosciences). Forward *versus* side scatter (FSC vs. SSC) gating was used to exclude cell debris using FlowJo 7.6 (BD Biosciences). CFSE fluorescence was analyzed visually in the FITC-A channel.

Cell counting with trypan blue staining. Concentration of VCR-R CEM WT and TPC2 KO cells was adjusted to 0.1×10^6 cells/ml on day 0 and cells were cultured in 75 cm² flasks. Cell number and viability were determined every 24 h by trypan blue staining over a period of 6 days using a ViCell XR cell counter (Beckman).

Compound screening by CellTiter-Blue® assay. Antiproliferative effects of compounds were determined by CellTiter-Blue® cell viability assay (Promega). Adherent cells were

seeded at the indicated cell densities (HCT-15: 3×10^3 cells, HepG2: 5×10^3 cells, RIL175: 2×10^3 cells, HUH7: 5×10^3 cells, MDA-MB-231: 5×10^3 cells, MCF7: 5×10^3 cells, T24: 5×10^3 cells per well) into wells of a 96 well plate and allowed to adhere overnight. 4 h after seeding, initial metabolic activity was determined and used as zero value. Treatment was performed for 72 h at the indicated concentrations. VCR-R CEM cells were seeded at a density of 20×10^3 cells per well of a 96-well plate, incubated for 4 h before stimulation with the indicated concentrations of compounds for 48 h. 2 h before the end of stimulation time, 20 μ L CellTiter-Blue[®] reagent was added to each well and fluorescence at 590 nm was detected with a SpectraFluor Plus[™] (Tecan). Half-maximal inhibitory concentrations (IC_{50}) values were calculated by nonlinear regression using GraphPad Prism 8.4.0 software (GraphPad Software).

3.19 Western Blot analysis

Western Blot analysis was conducted in order to examine protein levels of interest.

Impairment of proangiogenic signaling. HUVECs were seeded at a density of 0.5×10^6 cells per well of a 6-well plate and allowed to adhere overnight. After serum starvation for 4 h using ECGM medium (PELO Biotech) without supplements, cells were treated with vehicle, tetrandrine, SG005 or SG-094 (10 μ M) for 1 h. Subsequently, cells were either stimulated with VEGF-A₁₆₅ (0.1 μ g/mL) (Peprotech) or left untreated for 15 min before cell lysis.

Blotting of apoptosis markers (VCR-R CEM). VCR-R CEM cells were seeded at a density of 2.0×10^6 cells per well of a 6-well plate and incubated for 4 h. Subsequently, cells were treated with vincristine (0.1 μ M), with or without tetrandrine, SG005 or SG-094 (1 μ M) for 48 h before cell lysis.

PD-L1 and GRP78 expression after HDAC6 inhibition. T24 cells were seeded at a density of 0.8×10^6 cells per well of a 6-well plate and allowed to adhere overnight. Cells were treated with KV-46, KV-70 or KV-181 (10 μ M) for 48 h before cell lysis.

Cell lysis and immunoblotting. After cells were washed with ice-cold PBS, 100 μ L of radioimmunoprecipitation (RIPA) lysis buffer were added and cell lysates were frozen at -80 °C. After the removal of cell debris by centrifugation (14,000 rpm, 10 min, 4 °C), protein concentrations were determined by Bradford assay as described previously⁷⁸. For that purpose, 5 μ L of protein solution were diluted with 45 μ L of H₂O. 10 μ L of the obtained dilutions were mixed with 190 μ L of a 1:5 dilution Bradford reagent Roti[®] Quant (Bio-Rad) in water and incubated for 5 min. Absorbance of each sample at 592 nm was determined by photometric measurement using a SpectraFluor Plus[™] (Tecan) and linear regression

was conducted with bovine serum albumin (BSA) dilutions as protein standards. Protein concentrations were adjusted with 1X SDS (sodium dodecyl sulfate) sample buffer. Proteins were denatured at 95 °C for 5 min after addition of 5X SDS sample buffer. Equal amounts of protein were separated by sodium dodecyl sulfate polyacrylamide gel electrophoresis (SDS-PAGE) in electrophoresis buffer (100 V, 21 min then 200 V, 43 min) on discontinuous polyacrylamide gels, consisting of a gradient separation (6 -12 %) and a stacking gel. Afterwards, proteins were transferred to either nitrocellulose or polyvinylidene difluoride (PVDF) membranes that have been equilibrated in 1X tank buffer, *via* tank blotting (100 V, 90 min, 4 °C). After tank blotting, membranes were blocked with 5 % non-fat dry milk powder in PBS (Blotto) for 2 h. Incubation with the primary antibody was performed overnight at 4 °C. After 4 washing steps with TBS-T for 5 min each, the secondary, HRP-coupled antibody was added and incubated for 2 h. Following another 4 washing steps with TBS-T for 5 min each, the membranes were incubated with ECL solution and chemiluminescence was detected with a ChemiDoc™ Touch Imaging System (Bio-Rad). The bands were assigned by comparison with the Page Ruler™ Plus Prestained Protein Ladder (Fermentas). Data processing was performed with the Image Lab™ software (Bio-Rad).

RIPA lysis buffer		Separation gel 6-12 %	
Tris/HCl	50 mM	Rotiophorese™ Gel 30	40 - 80 %
NaCl	150 mM	Tris (pH 8.8)	375 mM
Nonidet NP-40	1 %	SDS	0.1 %
Sodium deoxycholate	0.25 %	TEMED	0.1 %
SDS	0.10 %	APS	0.05 %
H ₂ O			
added before use:			
Complete®EDTAfree	4 mM		
PMSF	0.5 mM		
activated Na ₃ VO ₄	2 mM		

5X SDS sample buffer		Electrophoresis buffer	
Tris/HCl pH 6.8	3.125 M	Tris	4.9 mM
Glycerol	50 %	Glycine	38 mM
SDS	5 %	SDS	0.1 %
DTT	2 %	H ₂ O	
Pryonin Y	0.025 %		
H ₂ O			

TBS-T (pH 7.6)		Tank buffer	
Tris/HCl	50 mM	Tris base	48 mM
NaCl	150 mM	Glycine	39 mM
Tween 20	0.05 %	Methanol	20 %
		H ₂ O	

Stacking gel	
Rotiophorese™ Gel 30	17 %
Tris (pH 6.8)	125 mM
SDS	0.1 %
TEMED	0.2 %
APS	0.1 %
H ₂ O	

Table 17 | Buffers and solutions for Western Blot analysis

Antigen	Product nr.	Provider	Dilution	In
BiP/GRP78	610978	BD Biosciences	1:1000	BSA 5 %
caspase 3, active	C8487	Sigma Aldrich	1:1000	BSA 5 %
hexokinase II (C64G5)	2867	CST	1:1000	BSA 5 %
PARP	9542	CST	1:1000	BSA 5 %
PD-L1 (E1L3N®) XP®	13684	CST	1:1000	BSA 5 %
phospho-Akt (Ser473)	9271	CST	1:1000	BSA 5 %
phospho-Cofilin (Ser3) (77G2)	3313	CST	1:1000	BSA 5 %
phospho-eNOS (Ser1177)	9571	CST	1:1000	BSA 5 %
phospho-p44/p42 MAPK (Thr202/Tyr204)	9106	CST	1:1000	BSA 5 %
phospho-p54/p46 SAPK/JNK (Thr183/Tyr185)	9251	CST	1:1000	BSA 5 %

Table 18 | Primary antibodies for Western Blot analysis

Antigen	Product nr.	Provider	Dilution	In
goat anti-mouse IgG1, HRP	BZL07046	Biozol	1:1000	BSA 5 %
goat anti-rabbit IgG (H+L)-HRP conjugate	172-1019	Bio-Rad	1:1000	BSA 5 %

Table 19 | Secondary antibodies for Western Blot analysis

3.20 Wound healing assay

2.5×10^4 RIL175 WT and TPC2 KO cells were seeded into the wells of a 96-well plate. A wound was scratched into the cell monolayer with a 96-well scratching device when cells reached confluency. PBS (containing Mg^{2+} and Ca^{2+}) was used to remove detached cells and each scratch was examined under a light microscope. After incubation at 37 °C for 18 h, cells were stained with crystal violet, which was performed by aspiration of medium, washing with PBS, fixation with methanol for 10 min and addition of crystal violet solution for min. Crystal violet solution was carefully removed and washed with water. The plate was dried overnight before images were taken with a LeicaDmil microscope with 4x magnification. Cells that were incubated with medium without FCS served as negative control. Wound closure was quantified with ImageJ software (NIH) and it was calculated with the following equation: Wound closure (%) = $100\% - \frac{\text{wound area (18 h)}}{\text{wound area (0 h)}} \times 100\%$.

3.21 Seahorse XF⁹⁶: Metabolic profiling

3.21.1 Purpose and measurement principle

In order to investigate differences in glycolysis and oxidative phosphorylation in RIL175 WT *versus* (vs.) TPC2 KO cells, the Seahorse Glycolysis Stress Test Kit and the Seahorse XF⁹⁶ FluxPaks (inc. mini) were used together with the Seahorse XF⁹⁶ Analyzer (all from Agilent Technologies). The analyzer measures two parameters, Extracellular Acidification Rate (ECAR) in mpH/min and Oxygen Consumption Rate (OCR) in pmol/min, simultaneously in real-time utilizing dual-florescent biosensors for protons and molecular oxygen. For metabolic profiling, cells are glucose-starved first in assay medium without glucose and pyruvate for 1 h. As first injection, a saturating concentration of glucose is injected. Secondly, oligomycin, which inhibits F_1F_0 -ATP synthase and thereby impairs mitochondrial ATP production, is injected and forces the cells to shift their energy production towards glycolysis in order to maintain ATP production and thereby energy homeostasis. Thirdly, the hexokinase II inhibitor 2-deoxy-D-glucose (2-DG) is injected to reveal that the increased ECAR was caused by glycolysis and not by other biochemical processes. In order to compare metabolic activities of different cell lines, the OCR/ECAR ratio can be used⁷⁹ or a normalization based on cell number has to be conducted as ECAR and OCR reflect both metabolic activity and total cell number.

3.21.2 Hydration of the Seahorse XF^e96 sensor cartridge

Each well of the utility plate (Agilent Technologies) was filled with 200 µL sterile H₂O and the sensors of the Seahorse XF^e96 cartridge (Agilent Technologies) were submerged into the H₂O. The plate was placed in a non-CO₂ incubator overnight together with an aliquot (20-50 mL) of XF Calibrant (Agilent Technologies). On the next day, H₂O was replaced with XF Calibrant, followed by 45-60 min of incubation in a non-CO₂ incubator prior to the assay.

3.21.3 Coating of the Seahorse XF^e96 microplate

Each well of the XF^e96 microplate (Agilent Technologies) was filled with 15 µL of poly-D-lysine (Sigma-Aldrich) coating solution (**Table 20**), followed by 5 minutes of incubation at room temperature. After incubation, poly-D-lysine solution was discarded and the wells were rinsed twice with sterile H₂O (100 µL per well). The XF^e96 microplate was subsequently dried for 2 hours in the laminar flow hood before collagen G coating solution (0.001% in PBS, Biochrom) was added. The plate was incubated with collagen G coating solution for 30 min at 37 °C prior to seeding of cells

Poly-D-lysine coating solution	
Poly-D-lysine hydrobromide	5 mg
H ₂ O (sterile)	50 mL

Table 20 | Poly-D-lysine coating solution

3.21.4 Seeding and treatment of cells in the XF^e96 microplate

For comparison of RIL175 WT and TPC2 KO cells, cells were seeded at a density of 1×10^4 cells per well of the XF^e96 microplate plate and allowed to adhere overnight. For determining the influence of TPC2 inhibitors, RIL175 WT cells were seeded at a density of 2×10^4 cells per well and allowed to adhere for at least 6 h. Cells were either pre-treated for 24 h in culture medium or for 1 h in assay medium without glucose as indicated prior to the assay.

3.21.5 Preparation of assay medium

Assay medium was prepared by dissolving the content of one vial of DMEM 5030-10X1L powder (Sigma-Aldrich, Taufkirchen, Germany), 26.7 mL L-Glutamine (Sigma-Aldrich, Taufkirchen, Germany) stock solution (150 mM in PBS) and 1.85 g NaCl (Carl Roth,

Karlsruhe, Germany) in 950 mL of H₂O. Following pH adjustment to 7.35 ± 0.05 at 37 °C, the assay medium was diluted ad 1000 mL with H₂O and sterile-filtered with a Millipore Express® PLUS membrane filter (0.22 µM, Merck Millipore, Darmstadt, Germany).

Assay medium (pH 7.35, 37 °C)	
DMEM 5030 powder	1 vial
L-Glutamine	4 mM
NaCl	143 mM
H ₂ O	ad 1000 mL

Table 21 | Seahorse assay medium

3.21.6 Washing of cells in the XF^e96 microplate

After two washing steps with pre-warmed (37 °C) assay medium (100 µL per well), 175 µL of assay medium with or without the respective compounds were added to each well and the XF^e96 microplate was placed in a non-CO₂ incubator for 60 min prior to the assay.

3.21.7 Loading of the XF^e96 sensor cartridge with injection compounds

The hydrated XF^e96 sensor cartridge ports were loaded with 25 µL of each injection compound, dissolved in assay medium (**Table 22**).

Port solutions for Glycolysis Stress Test (standard)	
D-Glucose (8X)	80 mM
Oligomycin (9X)	9 µM
2-Deoxy-D-glucose (10X)	500 mM
Assay medium (pH 7.35, 37 °C)	

Table 22 | Port solutions for metabolic profiling

3.21.8 Seahorse run

The assay template was designed with Wave 2.6.1 software and the run was performed with a Seahorse XF^e96 Analyzer (both from Agilent Technologies). Following calibration and equilibration, basal measurements of ECAR and OCR in assay medium without glucose and pyruvate were performed (4 measurement cycles, 20 min in total). Firstly, D-glucose was injected (10 mM final well concentration, 4 measurement cycles, 16 min in total). Secondly, oligomycin was injected, resulting in final well concentrations of 1 µM (4

measurement cycles, 16 min in total). Thirdly, 2-deoxy-D-glucose (2-DG) was injected, giving final well concentrations of 50 mM (6 measurement cycles, 24 min in total).

3.22 Quantitative real-time PCR analysis

mRNA was isolated from cell samples using the RNeasy® Mini Kit (250) (QIAGEN, Hilden, Germany) as described by the manufacturer. mRNA concentration was subsequently determined using a Nanodrop® Spectrophotometer (PEQLAB Biotechnologie, Erlangen, Germany). Reverse transcription was performed with the High-Capacity cDNA Reverse Transcription Kit (Applied Biosystems, Waltham, USA) according to the manufacturer's instructions. For the quantitative real-time polymerase chain reaction (qPCR), a QuantStudio™ 3 Real-Time PCR System (Applied Biosystems, Waltham, USA) was used. Primers were purchased from metabion (Planegg, Germany). They were designed using the NCBI database or the ThermoFisher Cloud OligoPerfect tool and the corresponding nucleotide codes are listed in Table 23. 100 ng of cDNA (2 µL), 6.25 µL PowerUp™ SYBR® Green Master Mix (Applied Biosystems, Waltham, USA), 3.75 µL RNase-free water and 0.025 mol of each primer (0.25 µL) were used for each well of the MicroAmp® Fast Optical 96-Well Reaction Plate, 0.1 mL (Applied Biosystems, Waltham, USA). The $\Delta\Delta C_T$ method was used to quantify changes in mRNA levels as described earlier⁸⁰ and actin was used as housekeeping gene. Previously, primer efficiency was determined for each primer pair using 500 ng, 50 ng and 5 ng of cDNA per well.

Target Name	FW/RV Primer	Sequence (5'-3')
actin (human)	FW Primer	CCAACCGCGAGAAGATGA
actin (human)	RV Primer	CCAGAGGCGTACAGGGATAG
actin (mouse)	FW Primer	CCACCATGTACCCAGGCATT
actin (mouse)	RV Primer	AGGGTGTAAAACGGAGCTCA
CYP3A4 (human)	FW Primer	GTATGGAAAAGTGTGGGGCT
CYP3A4 (human)	RV Primer	GACCATCTCCTTGAGTTTTCCA
TPC2 ex2 #1 (mouse)	FW Primer	GAAGAGCAGCCCCTTCTGG
TPC2 ex2 #1 (mouse)	RV Primer	GGAGCGGTACTTTATGGCGT
TPC2 ex2 #2 (mouse)	FW Primer	GAGCTCTGCATAGACCAGGC
TPC2 ex2 #2 (mouse)	RV Primer	GAGCTCTGCATAGACCAGGC
TPC2 5' (mouse)	FW Primer	GAAGAGCAGCCCCTTCTGG
TPC2 5' (mouse)	RV Primer	CCAGCGGTAAAGCCACAATG
TPC2 (human)	FW Primer	TGCATTGATCAGGCTGTGGT
TPC2 (human)	RV Primer	GAAGCTCAAAGTCCGTTGGC

Table 23 | Primers with nucleotide codes used for qPCR analysis

In some cases, PCR products were analyzed on an agarose gel (peqGOLD agarose, universal, VWR International) after quantitative real-time PCR. GeneRuler 1 kb Plus DNA Ladder (Thermo Fisher) was used as molecular size marker. GelRed (Biotium) was used to detect DNA.

3.23 Statistical analyses

All the listed experiments were conducted at least three times unless otherwise indicated in the figure legends. The given data are presented as means \pm SEM. Statistical differences between groups were assessed with a t-test (with or without Welch's correction as indicated) or with an ordinary one-way ANOVA and the indicated multiple comparisons test. Statistical analyses were performed with GraphPad Prism software version 8.4.0 (GraphPad Software).

3.24 Toxicity assays

For assessing the toxicity of muraricine, KV compounds as well as with tetrandrine and its analogues, several cellular models and approaches were used: HUVECs, PBMCs, differentiated HepaRGTM cells without transfection, differentiated HepaRGTM cells with transient transfection and HepG2 cells with stable transfection.

HUVECs. HUVECs were seeded at a density of 10×10^3 cells/well of a 96 well plate and allowed to adhere overnight. On the following day, cells were treated with the indicated concentrations of the respective compounds for 6 h. Cellular ATP content was quantified by CellTiter-Glo[®] cell viability assay (Promega). Therefore, 100 μ L CellTiter-Glo[®] reagent were added to 200 μ L medium in each well. Cell lysis was induced on an orbital shaker for 2 min, followed by 10 min incubation at room temperature in the dark. Subsequently, contents of each well were transferred to a plate suitable for luminescence measurement. Luminescence at 560 nm was recorded with an Orion II Microplate Luminometer (Berthold Detection Systems).

PBMCs. Peripheral blood mononuclear cells (PBMCs) were isolated from anticoagulated whole blood from healthy donors by density gradient centrifugation using Ficoll-PaqueTM PLUS density gradient medium (GE Healthcare) as described by the manufacturer. Blood samples were diluted with the same amount of Hanks balanced salt solution (HBSS) prior to application of Ficoll-PaqueTM PLUS solution. Cells were extracted from the PBMC layer with syringe and needle. Subsequently, the triple volume of HBSS (**Table 24**) was added to PBMCs.

HBSS (pH 7.2)			
CaCl ₂	1.26 mM	MgSO ₄ x 7 H ₂ O	0.41 mM
D-glucose	5.56 mM	Na ₂ HPO ₄	0.34 mM
KCl	5.33 mM	NaCl	137.9 mM
MgCl ₂ x 6 H ₂ O	0.49 mM	NaHCO ₃	4.17 mM
KH ₂ PO ₄	0.44 mM		
H ₂ O			

Table 24 | HBSS buffer.

The cell suspension was centrifuged and isolated PBMCs were cultivated in RPMI 1640 supplemented with 20 % FCS and 1 % penicillin/streptomycin (all purchased from PAN Biotech). 4 hours after seeding, cells were treated as indicated for 48 h. Cell death was analyzed by propidium iodide (5 µg/mL in PBS) staining and flow cytometry using a BD FACS Canto II (BD Biosciences). For evaluation, cell debris was excluded and propidium iodide positive cells were determined using FlowJo 7.6 (BD Biosciences) as shown in **Figure 6**. Assays with PBMCs were performed by Franz Geisslinger (Master Thesis, Prof. Vollmar, LMU Munich).

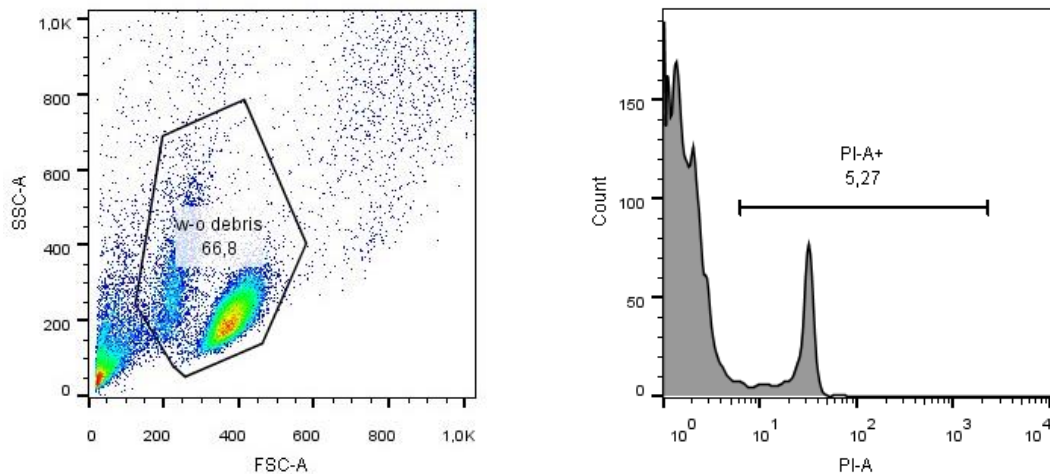


Figure 6 | Gating strategy used to determine viability of PBMCs.

Differentiated HepaRG™ cells without transfection. HepaRG™ cells were differentiated in Williams' medium E supplemented with GlutaMAX and HepaRG Maintenance/Metabolism Medium Supplement (Maintenance/Metabolism Working Medium) (all purchased from Life Technologies) as indicated by the manufacturer. After 24 h treatment with the respective compound concentrations, cell viability was determined by CellTiter-Blue® cell viability assay as described by the manufacturer.

Differentiated HepaRG™ cells with transient transfection with pcDNA3-CYP3A4-EGFP. HepaRG™ cells were differentiated as described above. 16 h prior to stimulation, cells were transfected with either pcDNA3-CYP3A4-EGFP or pcDNA3-EGFP using Lipofectamine™ 3000 (Invitrogen) transfection reagent according to the manufacturer's instructions. Cells were treated as indicated for 24 h. Cell death was assessed by propidium iodide (5 µg/mL in PBS; Carl Roth, Karlsruhe, Germany) staining and flow cytometry using a BD FACS Canto II (BD Biosciences). Data were analyzed using FlowJo 7.6 (BD Biosciences). No FSC/SSC gating was performed. Determination of the percentage of PI-A positive cells was conducted as stated below. Specific cell death was calculated as follows: $specific\ cell\ death\ (\%) = cell\ death\ (x)\ \% - cell\ death\ (control)\ \%$.

HepG2 cells with stable transfection with CYP3A4-EGFP. HepG2 cells were transfected with either pcDNA3-CYP3A4-EGFP or pcDNA3-EGFP using Lipofectamine™ 3000 (Invitrogen) transfection reagent according to the manufacturer's instructions. Transfected cells were constantly cultivated in the presence of 0.5 mg/mL G418 (Sigma Aldrich, St. Louis, USA) for four weeks. Presence of plasmids was confirmed by PCR (pcDNA3-forward: 5'-TACATCAATGGGCGTGGATAG-3', pcDNA3-reverse: 5'-AGGAAGGGAAGAAAGCGAAAG-3'). Primers were purchased from metabion. HepG2 cells stably expressing either CYP3A4-EGFP or pcDNA3-EGFP were seeded at a density of 0.1×10^6 cells per well of a 24-well plate and allowed to adhere overnight. Treatment, flow cytometry and data analysis were performed as described for HepaRG™ cells.

RESULTS



4 Results

4.1 Part I: Tetrahydroisoquinolines as inhibitors of TPC2 and P-gp

4.1.1 Functional effects of TPC2 knockout on liver cancer cells

4.1.1.1 Generation and validation of a TPC2 knockout cell line using CRISPR-Cas9

To test whether TPC2 is involved in cancer cell proliferation *in vitro* and tumor growth *in vivo*, the channel was knocked out using the CRISPR-Cas9 system in murine RIL175 hepatocellular carcinoma (HCC) cells. Successful deletion of exon 2 was confirmed by agarose gel analysis, Sanger sequencing of PCR products at DNA level (**Supplementary Figure 1 a**) and quantitative real-time PCR (qPCR) at mRNA level (**Supplementary Figure 1 b**). Furthermore, strongly reduced 5' mRNA levels indicated the presence of nonsense-mediated decay (NMD) as a response to the deletion (**Supplementary Figure 1 c**). In accordance with the agarose gel and qPCR analyses, PI(3,5)P₂-induced currents of enlarged lysosomes obtained from TPC2 knockout (KO) cells were strongly reduced, confirming loss of channel function (**Figure 7 a,b**). All endolysosomal patch clamp experiments were conducted by Yu-Kai Chao (Prof. Grimm, Walther Straub Institute of Pharmacology and Toxicology, LMU Munich). The ten predicted off-target sequences with the highest cutting frequency determination (CFD) scores⁷⁶ for each sgRNA were analyzed by Sanger sequencing and no insertions or deletions were detected for the clone of interest as compared with the WT control (**Supplementary Table 1, Supplementary Table 2**). Due to the lack of a suitable antibody, deletion of the protein was not investigated by immunoblotting. TPC2 KO cells in fact showed an impaired ability to migrate *in vitro* and to disseminate into the lungs of mice (**Figure 7 c,d**), both confirming as well as extending our knowledge of the effect of TPC2 on tumor cell migration¹².

Results

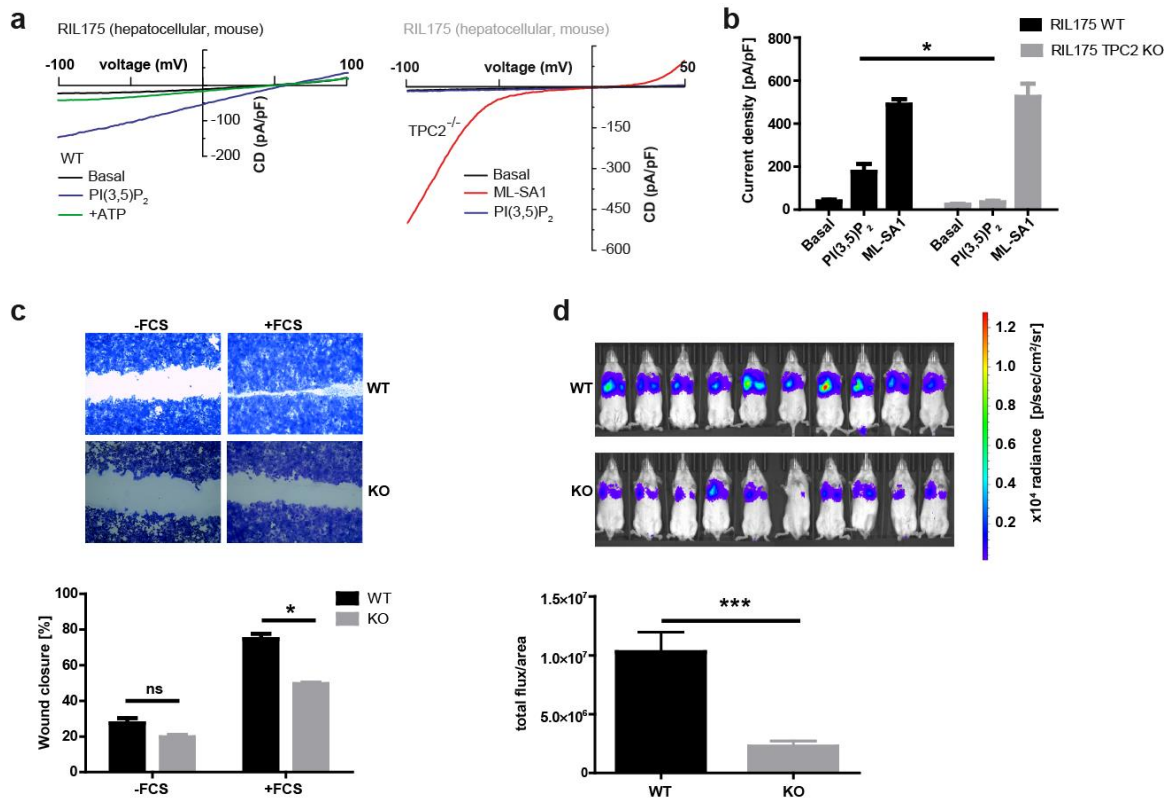


Figure 7 | Generation of a TPC2 knockout cell line and validation of loss of channel function by migration and dissemination assays. (a,b) Successful loss of TPC2 function was confirmed by measuring PI(3,5)P₂-evoked TPC2 currents on isolated, enlarged endolysosomes of RIL175 cells. Patch clamp experiments were performed by Yu-Kai Chao (Prof. Grimm, LMU Munich). The endogenous TPC2 inhibitor ATP⁸¹ and the TRPML1 activator ML-SA1⁶ were used as controls to ensure that TPC2 currents were elicited by PI(3,5)P₂ and that functional endolysosomes were used for measurements, respectively. (a) Representative patch clamp recordings of YM201636-enlarged acidic vesicles of WT and KO cells are shown. (b) Statistical analysis of PI(3,5)P₂-induced current densities of TPC2 WT versus (vs.) KO cells is shown as mean ± SEM of three independent experiments (Two-Way ANOVA, **P* < 0.05). (c) Reduced migration of TPC2 KO cells was determined using a scratch assay. Wound closure of RIL175 WT and TPC2 KO cells was determined 18 h after the scratch was performed. Cells were stained with crystal violet. Data are expressed as mean ± SEM, performed in triplicate (unpaired t-test with Welch's correction, **P* < 0.05). (d) TPC2 KO impairs tumor cell dissemination into the lungs of C57Bl/6-Tyr mice. Images of tumor-bearing mice 3 days after intravenous injection of RIL-175 WT and TPC2 KO cells are shown. The bar graph displays the quantified signal intensities as mean ± SEM of 10 mice per group (*n* = 10, unpaired t-test with Welch's correction, ****P* < 0.001). The dissemination assay was performed by Carina Ortler and Kerstin Schmid (Prof. Vollmar, LMU Munich).

4.1.1.2 TPC2 KO reduces proliferation and prevents tumor growth of HCC cells

Next, we aimed to investigate if TPC2 affects cell proliferation and tumor growth. Cell proliferation *in vitro* was monitored using real-time impedance measurements (Figure 8 a) and staining with the fluorescent dye CFSE (Figure 8 b), which can be used to monitor cell divisions. As evident from a reduced slope over a period of four days as well as from the presence of two CFSE-positive populations after three days, proliferation of TPC2 KO cells was considerably reduced (Figure 8 a,b). Remarkably, TPC2 KO completely abrogated tumor growth in an ectopic *in vivo* model using syngeneic C57Bl/6-Tyr mice

(Figure 8 c,d). Similar bioluminescence signals of WT and TPC2 KO tumors on day 2 ensured equivalent amounts of viable engrafted cells among both arms (Figure 8 c), whilst average signal intensity of TPC2 KO tumors was reduced by 99 % on day 10 ($P = 0.0006$) (Figure 8 c,d). Thus, this study emphasizes that interfering with TPC2 as a single target is sufficient to suppress tumor growth *in vivo*.

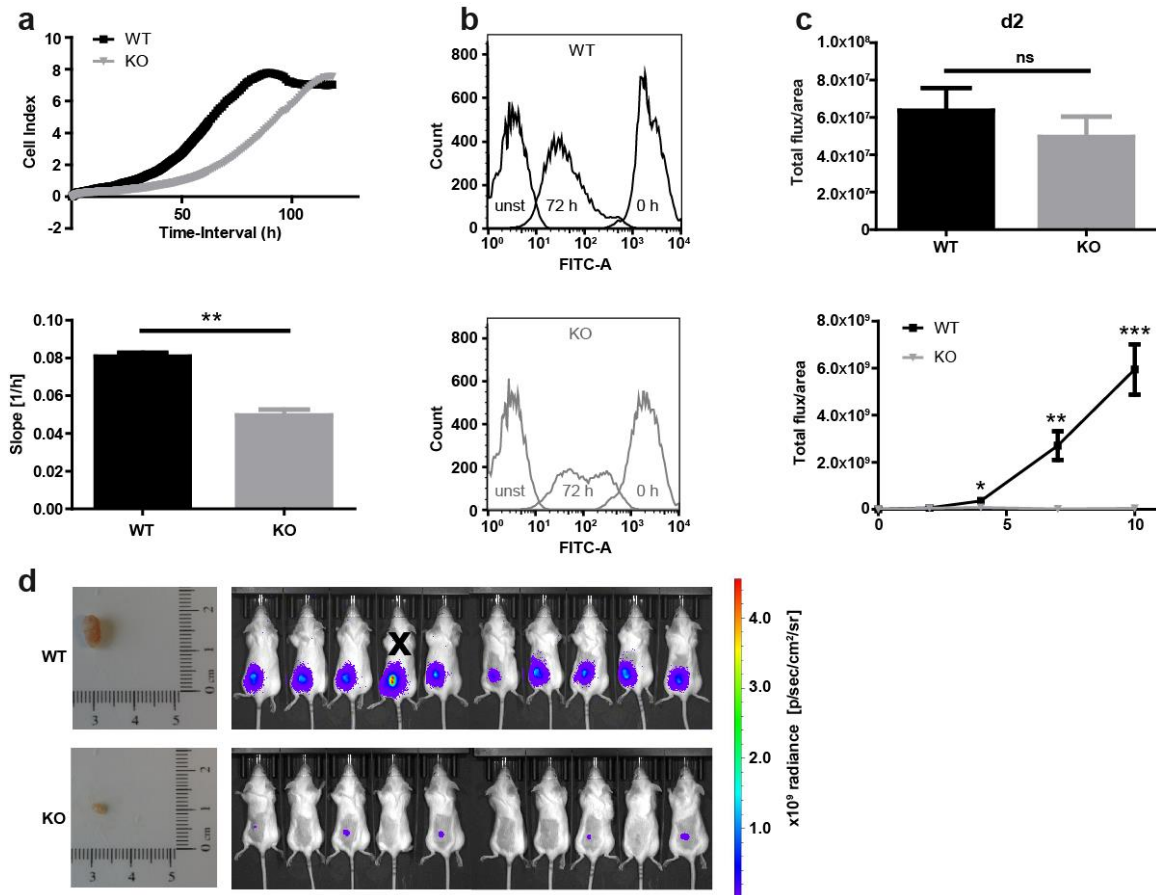


Figure 8 | TPC2 knockout impairs cancer cell proliferation and tumor growth. (a) Proliferation of RIL175 WT and TPC2 KO cells is shown as cell index over time from a representative experiment performed in triplicate. Statistical analysis of the slope is displayed as mean \pm SEM of three independent experiments (unpaired t-test with Welch's correction, $**P < 0.01$). (b) CFSE stainings of RIL175 WT and TPC2 KO cells are presented upon initial staining and after 72 h of incubation in comparison to the corresponding unstained (unst) control. Two populations, visible for TPC2 KO cells, indicate a reduced number of cell divisions after 72 h. Fluorescence (FITC-A) was detected by flow cytometry. The experiment was performed in triplicate and one representative experiment is shown. (c,d) RIL175 WT and TPC2 KO cells were implanted into the flanks of C57Bl/6-Tyr mice and TPC2 KO suppressed tumor growth. (c) The bar graph indicates similar levels of viable cells among both groups on day 2 (d2) after implantation. The line chart displays bioluminescence signal intensities of tumors over time as mean \pm SEM ($n = 10$ for RIL175 TPC2 KO, $n = 9$ for RIL175 WT, outlier identified with Grubbs' test and $\alpha = 0.05$, unpaired t-test with Welch's correction, $*P < 0.05$, $**P < 0.01$, $***P < 0.001$). (d) Bioluminescence images taken on day 10 are shown. The outlier is marked with an x. One excised tumor is exemplarily shown for each group.

4.1.1.3 TPC2 KO influences cellular energy metabolism

To support sustained proliferation, cancers often reprogram their energy metabolism¹⁴. As a result of the Warburg effect, listed as a cancer hallmark¹⁴, cancer cells derive their cellular ATP predominantly from glycolysis to fuel their high energy demand, regardless of oxygen availability⁸². The alkaloid dauricine, which we identified as TPC2 inhibitor in this study (4.1.2.1, **Figure 12 b**), is known to suppress glycolysis in HCC cells⁸³. Hence, we investigated if TPC2 is implicated in energy metabolism of RIL175 cells. Metabolic profiling on a Seahorse Extracellular Flux Analyzer revealed that, following 1 h of glucose starvation, TPC2-deficient RIL175 cells displayed a less glycolytic phenotype as indicated by an increased OCR/ECAR ratio (OCR: oxygen consumption rate, parameter for oxidative phosphorylation; ECAR: extracellular acidification rate, parameter for glycolytic activity) (**Figure 9 a**). This effect was abolished when saturating concentrations of D-glucose were injected (**Figure 9 a**). Despite being glucose-dependent, glucose deprivation is a common feature of solid tumors due to poor vascularization^{84, 85}, among others, and the OCR/ECAR ratio can be used to decipher the reliance of cells on glycolysis or oxidative phosphorylation⁷⁹. To further assess the role of TPC2 in energy metabolism, we applied a Förster resonance energy transfer (FRET) biosensor, that consists of a subunit of the bacterial F₀F₁-ATP-synthase and which can be used for real-time visualization of ATP levels inside single live cells⁷². Stressing the glycolytic pathway using the glycolysis inhibitor 2-deoxy-D-glucose (2-DG) resulted in a stronger drop of cellular ATP levels in WT cells, whereas TPC2 KO cells remained unaffected (**Figure 9 b,c**). Taken together, extracellular flux analysis and FRET live cell imaging indicated that loss of TPC2 function promotes a switch towards oxidative phosphorylation in HCC cells *in vitro*. Increased glycolysis, but also decreased mitochondrial function and respiration are hypothesized to promote tumor growth⁸⁶. As TPC2 KO favors the opposite effect, this study suggests that the metabolic implication of TPC2 contributes to the reduced proliferation rate *in vitro* and tumor growth *in vivo*.

Results

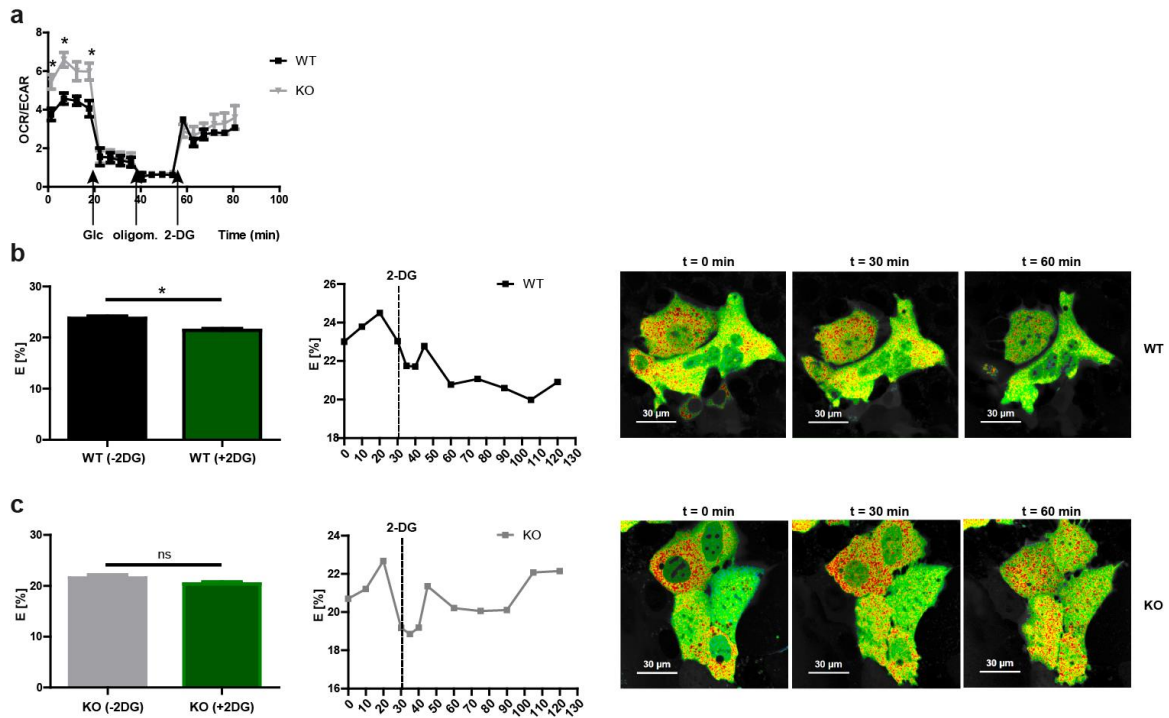


Figure 9 | TPC2 knockout alters the metabolic phenotype of cancer cells. (a) RIL175 WT and TPC2 KO cells were subjected to extracellular flux analysis on a Seahorse device. Metabolic profiling was performed after 1 h of glucose starvation to assess basal glycolytic and respiratory activity, which was followed by sequential injection of D-glucose (Glc) and oligomycin (oligom.) to determine glycolysis and respiratory activity after injection of saturating concentrations of glucose and glycolytic reserve upon inhibition of oxidative phosphorylation, respectively. The last injection of the glycolysis inhibitor 2-deoxy-D-glucose (2-DG) served as control. The OCR (oxygen consumption rate)/ECAR (extracellular acidification rate) ratio is displayed over time as mean \pm SEM, performed in triplicate (unpaired t-test with Welch's correction, $*P < 0.05$). An increase of the OCR/ECAR ratio, indicating a decreased reliance on aerobic glycolysis of TPC2 knockout cells, is visible. ATP levels of (b) RIL175 WT and (c) TPC2 KO cells were monitored in real-time using a FRET (Förster resonance energy transfer) biosensor before and after injection of 2-DG (5 mM, $t = 30$ min), suggesting a higher dependence on aerobic glycolysis for energy production of WT cells. ATP is sandwiched between the FRET pair, consisting of a green fluorescent protein (GFP) and an orange fluorescent protein (OPF), and corresponds to higher FRET efficiency (E). FLIM-FRET imaging was performed by Florian Gegenfurtner and Themistoklis Zisis (Prof. Vollmar, LMU Munich). Bar graphs, line charts and images from a representative experiment performed in triplicate are shown (unpaired t-test with Welch's correction, $*P < 0.05$).

4.1.2 Development and biological investigation of novel cytostatic TPC2 inhibitors

4.1.2.1 Screening of a library of (bis)benzyltetrahydroisoquinolines

After having shown that genetic ablation of the channel is sufficient to induce antitumor effects (Figure 8), we aimed to identify pharmacological TPC2 inhibitors, derived from the known inhibitor tetrandrine^{12, 24}, with potent anticancer properties. High micromolar concentrations of known TPC2 inhibitors, synthetic compounds Ned-19 ($\geq 100 \mu\text{M}$) and natural flavonoid naringenin ($\geq 75 \mu\text{M}$) were required to inhibit proliferation of RIL175 cells (Supplementary Figure 2 a,b). Thus, these compounds were not studied further. Instead,

we screened tetrandrine and related compounds, including commercially available bisbenzyltetrahydroisoquinoline (BBTHIQ) alkaloids, such as oxyacanthine and berbamine (**Figure 10 a**), and, additionally, a library of synthesized truncated variants (**Figure 10 b**) for their potential to inhibit cancer cell growth and TPC2 function. Hence, BBTHIQs bearing two tetrahydroisoquinoline moieties, as well as monomeric 1-benzyltetrahydroisoquinolines (BTHIQs, simplified tetrandrine congeners) were included in the screening. Synthesis of truncated tetrandrine variants (SG compounds, **Supplementary Figure 3**) was performed by Susanne Gerndt (Prof. Bracher, Department of Pharmacy, LMU Munich). Some simplified tetrandrine congeners were previously probed by Iturriaga-Vásquez *et al.* for their affinities to α_1 -adrenergic receptors and L-type Ca^{2+} channels⁸⁷.

Firstly, the antiproliferative properties of our compound library were evaluated using RIL175 cells. Thereby, numerous molecules with increased potency as compared with tetrandrine (half-maximal inhibitory concentration/ IC_{50} : 9.1 μM) were identified, including truncated variants with IC_{50} values in the low micromolar range (**Figure 10 a,b**). To analyze structure-activity relationships, different positions of the tetrahydroisoquinoline scaffold were modified and the antiproliferative effect was examined. To make a long story short, monomeric BTHIQs bearing additional aromatic residues (phenyl or benzyl ethers) at both benzenoid rings were found to have outstanding properties. When modifying the amino group, antiproliferative activity remained in a similar range (IC_{50} : 2.4-4.8 μM) when *N*-alkyl residues of different lengths (*NH* (Z3), *N*-methyl (SG-005, SG-159), *N*-ethyl (SG-158) were used, provided that the nitrogen atom retained its basicity. *N*-Acyl variants lost their antiproliferative properties (SG-089, SG-145, IC_{50} : $\geq 33.0 \mu\text{M}$). Variations at C-6 and C-7 of the isoquinoline unit had only slight effects. In most cases, loss of the aromatic substituents (aryl- or benzyl ethers) in C-7 position slightly decreased antiproliferative activity (SG-083, SG-127, SG-157, IC_{50} : 7.6-11.0 μM). The same applied if the 1-benzyl group was changed into a phenyl group (SG-122 vs. SG-157), whereas shifting a benzyloxy residue from position C-7 to C-6 had no influence (Z3 vs. Z5). Furthermore, the impact of modifications of the 1-benzyl residue was investigated. Variation of substitution patterns, mostly differing in *meta* or *para* position, did not markedly affect antiproliferative activity (SG-005, SG-159, Z6, Z11, Z13, Z15, Z18, Z20, IC_{50} : 1.2-4.8 μM). Miscellaneous diaryl ethers at the 1-benzyl residue were synthesized bearing both electron-donating and -releasing substituents, mainly in *meta* or *para* position (SG-153, SG-154, SG-155, SG-161, SG-162, SG-164, SG-165). In most cases, no changes in antiproliferative potency were observed (IC_{50} : 3.9-5.6 μM). However, cyano and chlorine substituents slightly (SG-

Results

164, SG-165, IC₅₀: 8.5-9.1 μM) and the pyridine moiety strongly reduced it (SG-163, IC₅₀: 22.0 μM). Further, deletion of both benzyl or diaryl ether moieties resulted in significant reduction (SG-132, IC₅₀: 11.0 μM) or complete loss of activity (SG-089, SG-121, SG-121-NP, IC₅₀: > 50 μM). Summarizing, all BTHIQs carrying two aryl or benzyl ether groups and a basic amine inhibited proliferation of RIL175 cells to a similar extent or stronger than tetrandrine.

Results

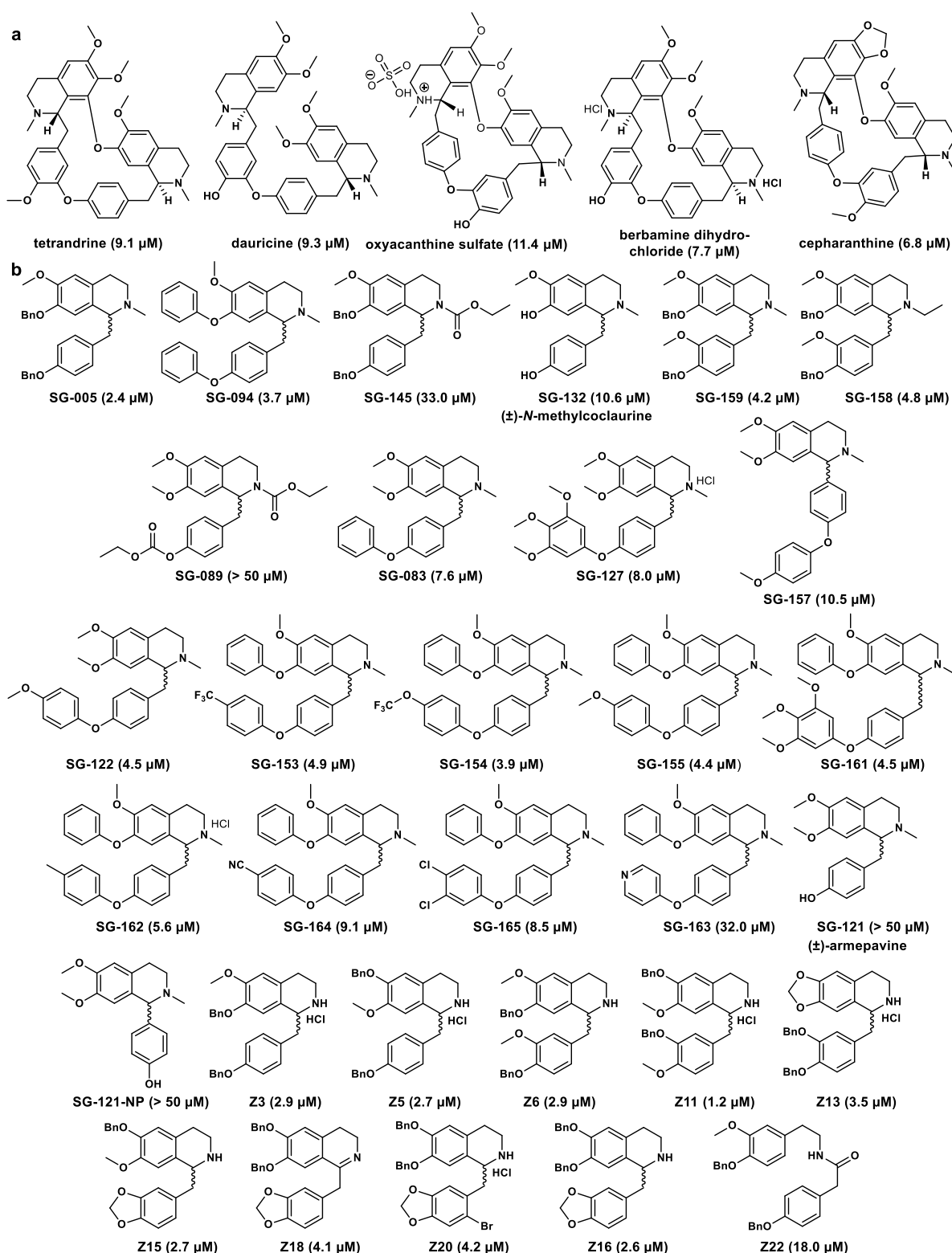


Figure 10 | Structures of the (bis)benzyltetrahydroisoquinoline library. **(a)** Bisbenzyltetrahydroisoquinoline alkaloids and derivatives, which were applied in enantiopure form, are listed. **(b)** Structures of monomeric 1-benzyltetrahydroisoquinolines, consisting of synthesized tetrandrine congeners (SG compounds) and substances from other sources (Z compounds), which were used in racemic form, are shown. SG compounds were synthesized by Susanne Gerndt (Prof. Bracher, LMU Munich).

Thus, the two simplest BTHIQs, SG-005 and SG-094, either bearing two unsubstituted benzyl (SG-005) or two phenyl (SG-094) ethers, were subjected to further investigation. SG-005 (IC₅₀: 2.4 μM) and SG-094 (IC₅₀: 3.7 μM) both displayed markedly enhanced antiproliferative effects against RIL175 cells, compared with tetrandrine (**Figure 11 a**). Furthermore, SG-005 exerted similar or increased antiproliferative potencies against various other cancer cell lines, including human hepatocellular carcinoma (HUH7, HepG2), human breast cancer (MCF7), human colorectal adenocarcinoma (HCT-15) and human vincristine-resistant acute lymphoblastic leukemia (VCR-R CEM) (**Figure 11 b-f**). Except for HUH7 cells (**Figure 11 b**), SG-094 inhibited proliferation of the other tested cancer cell lines to a similar or higher extent than tetrandrine (**Figure 11 d-f**).

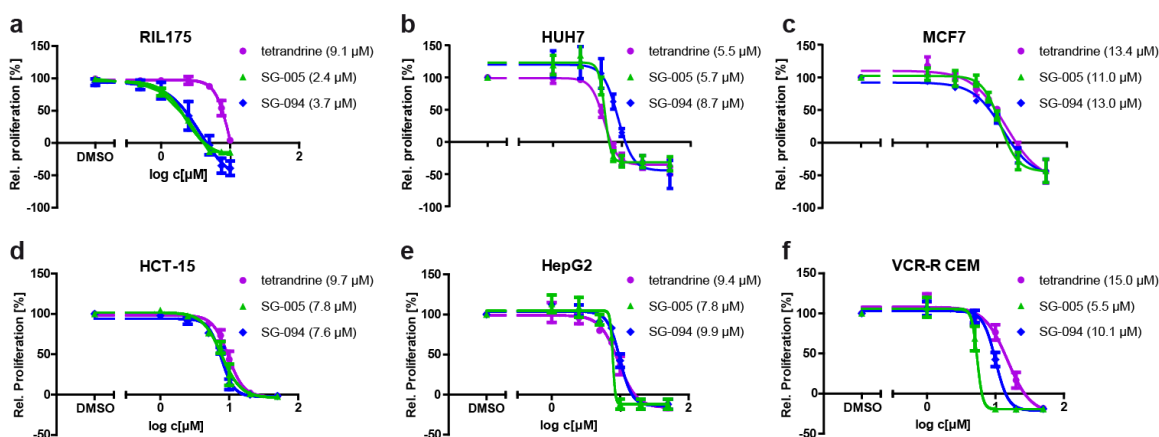


Figure 11 | Effects of tetrandrine and the truncated analogues SG-005 and SG-094 on various cancer cell lines. Antiproliferative effects of the respective compounds were assessed by CellTiter-Blue[®] cell viability assays. (a) RIL175, (b) HUH7, (c) MCF7, (d) HCT-15, (e) HepG2 and (f) VCR-R CEM cells. (a-e) Adherent cancer cells were treated for 72 h, (f) VCR-R CEM cells were treated for 48 h and IC₅₀ values were calculated by nonlinear regression. (a-f) Fluorescence intensities were normalized to vehicle control and are displayed as mean ± SEM of three independent experiments.

By applying the endolysosomal patch clamp technique⁷¹ (performed by Yu-Kai Chao, Prof. Grimm, LMU Munich), we analyzed their potential to block PI(3,5)P₂-elicited TPC2 currents. Notably, the bis-phenyl ether SG-094 significantly increased the percentage of channel inhibition (75 %) as against tetrandrine (54 %), whereas SG-005 was virtually equipotent (44 %) with tetrandrine, the related bisbenzylisoquinoline alkaloid cepharanthine and the natural *seco*-analogue dauricine (**Figure 12 a,b**). The inhibitory effect of tetrandrine, SG-005 and SG-094 on TPC2 was further confirmed by single cell Ca²⁺ imaging (**Figure 12 c**, performed by Susanne Gerndt, Prof. Bracher, LMU Munich). As recently shown by Gerndt *et al.*⁶, TPC2 inhibitors can be screened by Ca²⁺ imaging taking advantage of a plasma membrane version of TPC2 using the small molecule activator TPC2-A1-N. In contrast, SG-132 and SG-145, either lacking both essential

aromatic substituents or a basic nitrogen, respectively, were not able to inhibit TPC2 activation (**Figure 12 d**).

To identify potential eutomers, the racemates SG-005 and SG-094 were separated by semi-preparative chiral HPLC (Susanne Gerndt, Prof. Bracher, LMU Munich). The absolute configuration of the enantiomers was determined using ECD spectra and confirmed by computational calculations (performed by Aaron Gerwien, Prof. Dube, LMU Munich, data not shown). Notably, Ca^{2+} imaging revealed that both enantiomers of SG-005 and SG-094 inhibit TPC2 upon activation (**Supplementary Figure 4**, performed by Nicole Urban, Prof. Schäfer, Leipzig University). Consequently, the racemates were used for all following experiments. Due to the strong dependence of channel activation on the transfection level, single cell Ca^{2+} imaging rather represents a qualitative than a quantitative approach. Obviously, the presence of a simplified, monomeric BTHIQ structure bearing two aryl ethers (the additional phenyl rings most likely mimicking parts of the second benzyloisoquinoline unit of tetrandrine) appears to be sufficient to induce inhibitory effects on TPC2 and cell proliferation, while both effects are at least as strong as those of the more complex lead structure tetrandrine.

Results

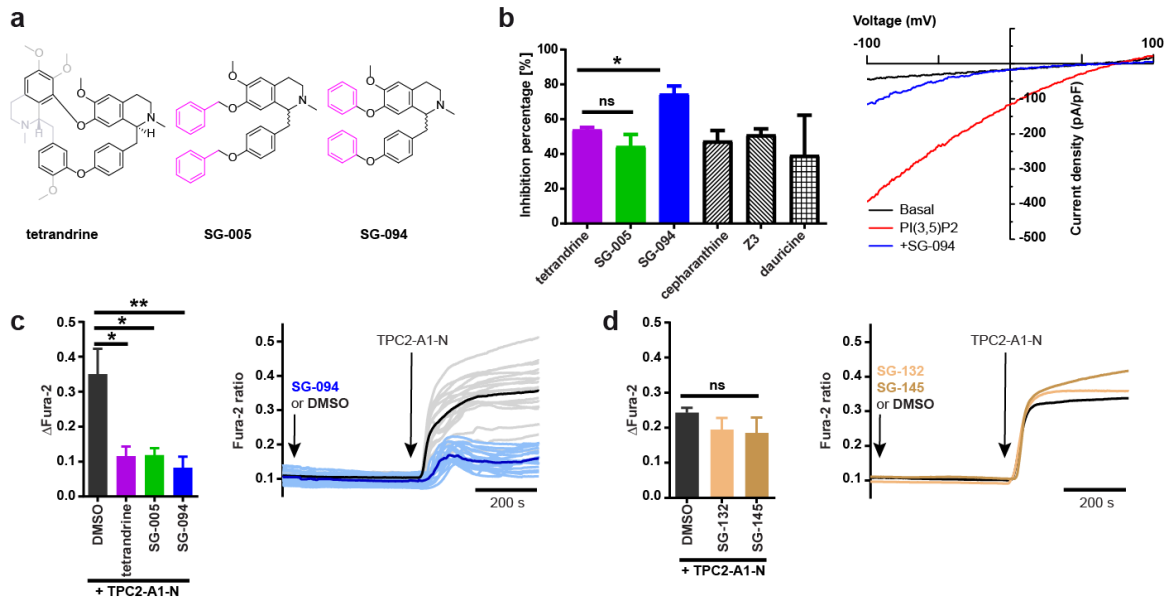


Figure 12 | Identification of novel TPC2 inhibitors. (a) Chemical structures of tetrandrine, SG-005 and SG-094 are presented. Dispensable substructures for biological activity of tetrandrine are shaded. Benzyl and phenyl moieties of SG-005 and SG-094 at the western half of the molecules, respectively, are highlighted in purple. (b) The inhibition percentage of several TPC2 blockers is displayed. 10 μM of inhibitors were applied upon activation with 1 μM of PI(3,5)P₂ on isolated and vacuolin-enlarged endolysosomes from HEK293 cells expressing TPC2-EGFP. The bar graph indicates mean \pm SEM of at least two independent experiments (unpaired t-test, * $P < 0.05$). Additionally, a representative current density – voltage relation is shown for a recording of the most potent TPC2 inhibitor of the study, SG-094. Patch clamp experiments were performed by Yu-Kai Chao (Prof. Grimm, LMU Munich). (c) Ca²⁺ imaging results of tetrandrine, SG-005, SG-094 and a DMSO control using the TPC2 activator TPC2-A1-N⁶ are displayed. For Ca²⁺ imaging of inhibitors, HEK293 cells stably expressing TPC2^{L11A/L12A}-RFP⁶ were used. After applying the inhibitors (10 μM each) and monitoring the signal for 400 s, cells were stimulated with the activator TPC2-A1-N (10 μM) and further recorded for 400 s. Experiment was performed at least in sextuplicate and statistical analysis of the maximal change in Fura-2 ratio for activation is shown (mean \pm SEM, unpaired t-test, * $P < 0.05$, ** $P < 0.01$). Representative Ca²⁺ signals showing the direct comparison of SG-094 ($n = 18$ single cells) and DMSO ($n = 17$ single cells). Means are represented as highlighted lines, while single cell traces of each experiment are visualized as shaded lines. (d) Experiments were performed as in (c), investigating SG-132 ($n = 4$) and SG-145 ($n = 4$) as for their potential to inhibit TPC2 in comparison to vehicle control after activation with TPC2-A1-N (10 μM). Experiment was performed at least in triplicate and statistical analysis of the maximal change in Fura-2 ratio (mean \pm SEM, unpaired t-test, ns, not significant) is shown. Representative Ca²⁺ signals depicting the mean of SG-132, SG-145 and a DMSO control and stimulation of each with TPC2-A1-N (10 μM) are displayed. Ca²⁺ imaging was performed by Susanne Gerndt (Prof. Bracher, LMU Munich).

4.1.2.2 Functional characterization of the tetrandrine congeners SG-005 and SG-094

As stated above, SG-005 and SG-094 were identified as advanced candidates from the screened (B)BTHIQ library in our effort to identify TPC2 blockers with potent anticancer properties. Next, we endeavored to characterize these compounds in more detail in a cellular setting by validating known biological effects of TPC2 inhibition and by determining their cellular and lysosomal uptake and their effects on glucose metabolism, all in direct comparison to tetrandrine.

Firstly, we wanted to confirm their on-target activities by investigating their capabilities of impairing the VEGFR2/NAADP/TPC2/Ca²⁺ signaling pathway. The involvement of TPC2-mediated Ca²⁺ release in neoangiogenesis of endothelial cells was described by others by applying anti-TPC2 shRNA¹³, the NAADP antagonist Ned-19¹³ and the TPC2 inhibitor naringenin¹⁵. Impaired TPC2 function reduced VEGF-evoked activation of eNOS, JNK, MAPK and AKT¹³ in human umbilical vein endothelial cells (HUVECs). We used SG-132 and SG-145, which do not block TPC2 (**4.1.2.1, Figure 12 d**), as negative controls. Western blot analysis revealed that only SG-005 and SG-094 were capable of significantly reducing VEGF-induced phosphorylation levels of several downstream targets, including eNOS, JNK and AKT, indicating that both molecules also act as TPC2 inhibitors in a cellular setting (**Figure 13 a,b**). As expected, SG-132 or SG-145 did not result in reduced phosphorylation of the investigated VEGFR2 downstream targets. Surprisingly, also tetrandrine had no effect under the chosen treatment conditions.

As tetrandrine and SG-005 displayed a similar inhibitory effect on TPC2 in patch clamp analysis (**4.1.2.1, Figure 12 b**), the question arose if they differ in their pharmacokinetic properties. Therefore, we investigated the cellular uptake of tetrandrine, SG-005 and SG-094 by analytical HPLC. Of all three tested compounds, detectable amounts were taken up by HUVECs within a 75 min incubation time at both tested concentrations (2 and 10 μ M) (**Supplementary Figure 5 a**). Incorporation of SG-005 into HUVECs was slightly higher than that of tetrandrine and SG-094 at 2 μ M (**Supplementary Figure 5 a**). For the higher concentration (10 μ M), which was previously used for western blot analysis of the VEGF-dependent signaling pathway, however, no significant differences were found (**Supplementary Figure 5 a**). These data indicate that the driver for improved efficacy of SG-005 or SG-094 to hinder VEGF-induced phosphorylation of eNOS, JNK and AKT, as compared to tetrandrine, is not an altered uptake into the cells. In a next step, we determined the uptake of the TPC2 blockers into RIL175 cells. Neither SG-005 nor SG-094 were internalized to a greater extent at both concentrations, as compared with tetrandrine (**Supplementary Figure 5 b**). Of note, when comparing their uptake into primary endothelial and cancerous liver cells, all three molecules of interest showed a preference for RIL175 cells vs. HUVECs (**Figure 13 c**).

Thereafter, their uptake into lysosomes was examined by their propensity to diminish fluorescence of LysoTrackerTM Red, as shown by others for basic compounds^{50, 88}. Interestingly, reduction of LysoTrackerTM Red fluorescence by SG-005 and SG-094 was larger than that caused by tetrandrine in HUVECs and RIL175 cells, indicating stronger accumulation of the new synthetic compounds in acidic vesicles (**Figure 13 d,e**). This

Results

decrease was similarly observed in RIL175 TPC2 KO cells (**Supplementary Figure 6**). Taken together, analysis of VEGFR2 downstream targets suggested improved on-target activity on TPC2 for the tetrandrine congeners SG-005 and SG-094. While initial cellular uptake does not markedly differ, accumulation of SG-005 and SG-094 in their intended cellular target organelles is enhanced compared to tetrandrine.

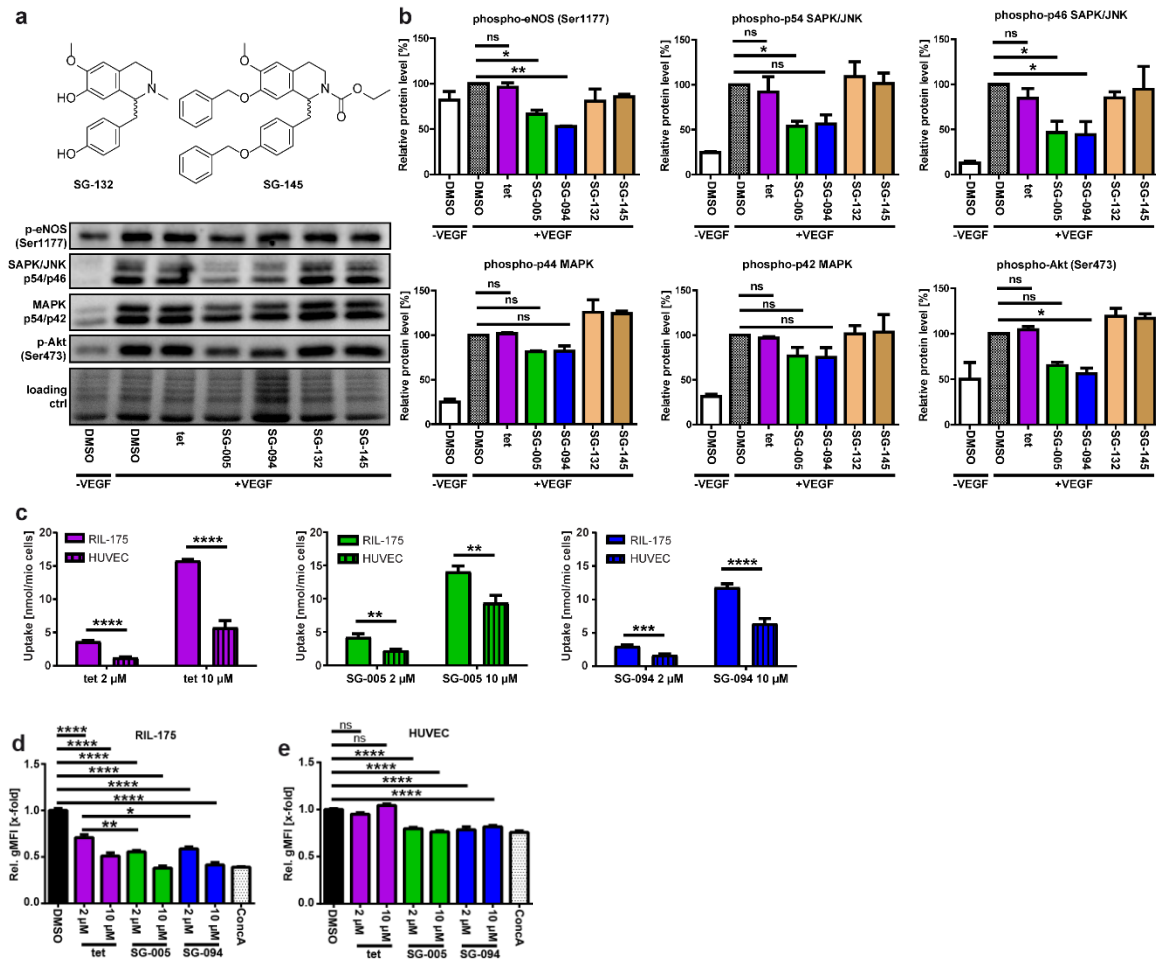


Figure 13 | SG-005 and SG-094 impair VEGFR2 downstream signaling and are preferably taken up by cancer vs. endothelial cells. (a,b) Only SG-005 and SG-094 impair phosphorylation of VEGFR2 downstream targets. (a) After serum starvation for 4 h, HUVECs were pre-treated with 10 μ M of the TPC2 inhibitors tetrandrine, SG-005 and SG-094 or with the non-TPC2 inhibitors SG-132 and SG-145 (chemical structures are shown) before stimulation with VEGF-A₁₆₅ (0.1 μ g/mL) for 15 min. Phosphorylated proteins were analyzed by western blotting. The experiment was performed in triplicate and a representative experiment is shown. tet, tetrandrine. (b) Quantitative evaluation of protein levels from (a) is shown. Proteins of interest were normalized to whole lane protein and are presented as percentage relative to vehicle control. The bar graphs indicate mean \pm SEM of three independent experiments (One-Way ANOVA followed by Dunnett's multiple comparison test, * $P < 0.05$, ** $P < 0.01$, ns, not significant). (c) Tetrandrine, SG-005 and SG-094 are preferably taken up by RIL175 cells. The amount of incorporated compounds within 75 min was determined by analytical HPLC and was normalized to cell number. Bar graphs indicate mean \pm SEM from three independent experiments (unpaired t-test with Welch's correction, ** $P < 0.01$, *** $P < 0.001$, **** $P < 0.0001$). (d,e) Reduction of LysoTracker™ Red fluorescence indicates lysosomal uptake of tetrandrine, SG-005 and SG-094 into (d) RIL175 WT cells and (e) HUVECs within 60 min. (d,e) Geometric means of fluorescence intensity (gMFI) were determined by flow cytometry and normalized to DMSO control. Concanamycin A (ConcA, 10 nM) served as control. Bar graphs indicate mean \pm SEM of three independent experiments (One-Way ANOVA followed by Tukey's multiple comparison test, * $P < 0.05$, ** $P < 0.01$, **** $P < 0.0001$, ns, not significant).

Next, we aimed to test the inhibitors for their implications on glucose metabolism, which we identified as one pathway that is altered as a result of TPC2 deficiency (**4.1.1.3, Figure 9**). Metabolic profiling revealed that, upon short-term pre-treatment (1 h) with low micromolar doses of tetrandrine, SG-005 and SG-094, a shift towards higher oxygen consumption after glucose starvation occurred (**Figure 14 a**). Applying higher concentrations of tetrandrine (10-50 μ M, 1 h) and extending treatment duration (24 h) also caused a metabolic shift towards lower glycolysis, whereas the opposite effect was observed for SG-005 and SG-094 (**Supplementary Figure 7 a,b**). We partly linked this to a non-TPC2-related impairment of mitochondrial function, indicated by mitochondrial membrane depolarization, which was most evident after SG-005 treatment (**Supplementary Figure 7 c**). Loss of mitochondrial membrane potential results in a decoupling of the respiratory chain⁸⁹, whereas cytosolic glycolysis is likely to remain unaffected. Additionally, strong compensatory upregulation of mitochondrial mass was detected for longer incubation times and high micromolar doses of SG-005 and SG-094 (**Supplementary Figure 7 d**), a phenomenon described in the literature as a response to mitochondrial dysfunction⁹⁰. To further decipher the effects of pharmacological TPC2 inhibition on cellular energy metabolism, ATP levels were visualized by FRET-based live cell monitoring. As observed for genetic TPC2 ablation, SG-005-treated (2 μ M, 1 h) RIL175 cells were less susceptible to inhibition of the glycolytic pathway (**Figure 14 c**). In contrast, ATP levels in untreated WT cells were significantly decreased after addition of 2-DG (**Figure 14 b**), suggesting a stronger dependence on glycolysis for energy production. Consequently, pharmacological inhibition of TPC2 can lead to a metabolic shift towards a less glycolytic phenotype.

Results

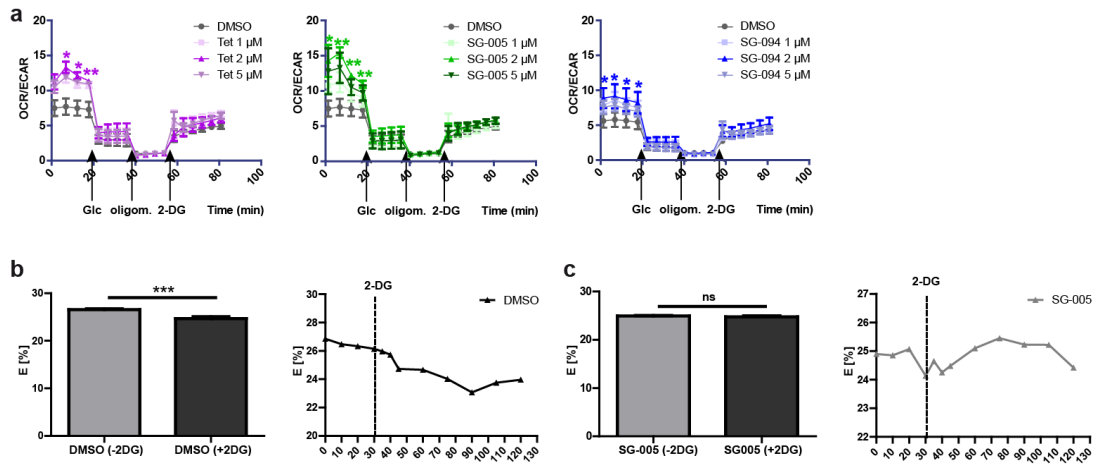


Figure 14 | Tetrandrine, SG-005 and SG-094 affect energy metabolism of RIL175 cells. (a) Tetrandrine, SG-005 and SG-094 pre-treatments (1, 2 and 5 μM) increase OCR/ECAR ratios of RIL175 WT cells after glucose starvation. Metabolic profiling was performed as described for **Figure 9 a**. The OCR/ECAR ratios are displayed over time as mean ± SEM, performed in triplicate and statistical analyses are shown for 2 μM (repeated measures ANOVA followed by Dunnett's multiple comparison test, * $P < 0.05$, ** $P < 0.01$). (b,c) Real-time monitoring of ATP levels in RIL175 WT cells after pre-treatment with (b) DMSO or (c) SG-005 (2 μM) as described in **Figure 9 b,c**. (b,c) Bar graphs, line charts and images from a representative experiment performed in triplicate are shown (unpaired t-test with Welch's correction, *** $P < 0.001$, ns, not significant). E, FRET efficiency.

4.1.2.3 SG-005 and SG-094 are less toxic to non-cancerous cells than tetrandrine

Tetrandrine treatment can be harmful to lungs²⁷ and liver^{28, 91, 92, 93} *in vivo*, which was related to metabolic activation by CYP enzymes^{27, 92, 94} or mitochondrial pathways⁹³. As we sought to cope with this drawback by simplification to the relevant pharmacophores, we probed tetrandrine and its congeners SG-005 and SG-094 for their toxic effect on the non-cancerous hepatic stem cell line HepaRGTM. Firstly, HepaRGTM progenitor cells, which possess various characteristics of primary human hepatocytes⁹⁵, were exposed to 24 h treatment to assess acute toxicity. Tetrandrine treatment caused the strongest decrease of cell viability at 10 and 20 μM (10 μM: 88 % viability, 20 μM: 63 % viability), compared with SG-005 (10 μM: 104 % viability, 20 μM: 93 % viability) and SG-094 (10 μM: 104 % viability, 20 μM: 98 % viability) (**Figure 15 a**). Secondly, differentiated HepaRGTM cells were used after seven days in culture, characterized by peak levels of CYP activities^{96,97}. Following treatment with 10 μM, tetrandrine induced a stronger effect on cell viability (63 %), as compared with SG-005 (84 %) and SG-094 (90 %), whereas 20 μM caused similar cytotoxicities (61-72 % viability) (**Figure 15 b**). Toxicity was also probed against peripheral blood mononuclear cells (PBMCs). At 10 μM, the strongest impact on cell viability was observed for tetrandrine (86 %) in comparison to the congeners (SG-005: 92 %, SG-094: 95 %) (**Figure 15 c**). Following treatment with 20 μM, SG-094 had the least influence on cell viability (91 %) (**Figure 15 c**). To study whether the observed elevated

toxicity of tetrandrine to non-cancerous liver cells is primarily caused by metabolic toxification through CYP3A4-mediated oxidation, as proposed by others²⁷, HepaRGTM cells were transiently transfected with CYP3A4-EGFP following seven days of culture. CYP3A4 overexpression did not increase cell death for any of the tested benzylisoquinolines (**Figure 15 d**). In line with the cell viability assays, tetrandrine triggered the highest specific cell death (10 %) of HepaRGTM cells, whilst SG-005 had a smaller and SG-094 had no effect (**Figure 15 d**). Additionally, toxicity to transgenic HepG2 cells, a cancerous model cell line for recombinant CYP overexpression and hepatotoxicity studies^{98, 99, 100, 101}, was evaluated. Both stable (**Figure 15 e**) and transient overexpression (**Figure 15 f**) of CYP3A4-EGFP did not significantly affect cell death following treatment with the three compounds (**Figure 15 e,f**). Likewise, combination with the CYP3A4 inhibitor ketoconazole (KCZ)⁹⁹ had no protective effect against cell death (**Figure 15 e,f**), suggesting that metabolic activation by CYP3A4 is not a primary cause of the increased cytotoxicity of tetrandrine *in vitro*. Metabolic toxification of tetrandrine by CYP3A4 was investigated in more detail in chapter 4.1.4. In accordance with the enhanced antiproliferative potency of SG-005 against cancerous HepG2 cells (4.1.2.1, **Figure 11 e**), cell death induction was most evident upon SG-005 treatment (**Figure 15 e,f**). Together, our data highlight decreased toxicities of the tetrandrine congeners SG-005 and SG-094 to non-cancerous liver and blood cells, which is most likely not primarily related to reduced susceptibility to toxification by CYP3A4. Thus, removal of substructures from tetrandrine slightly (SG-005) or substantially (SG-094) improves the toxicity profile for healthy cells.

Results

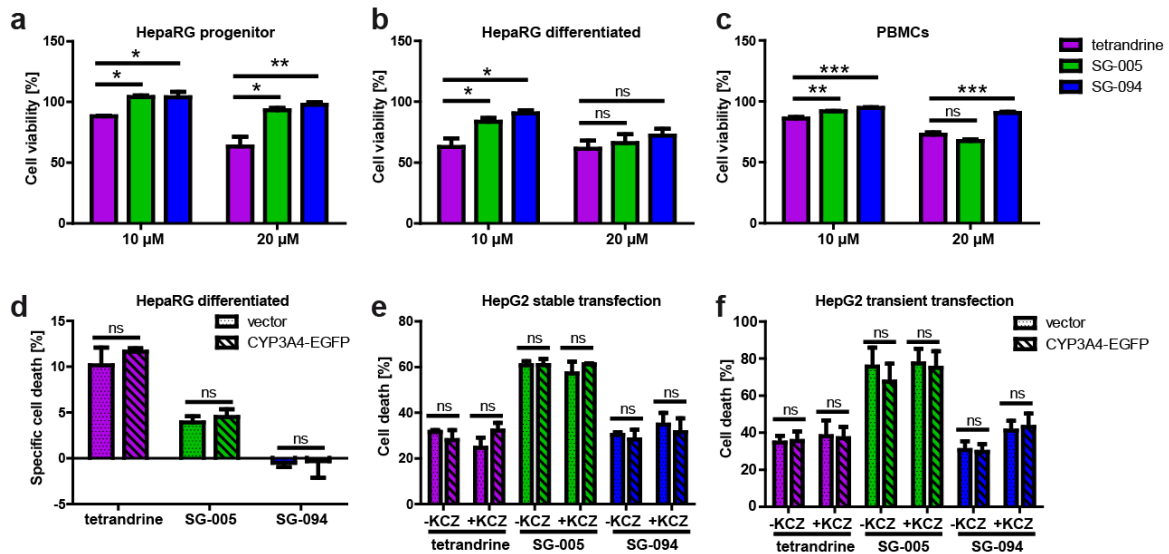


Figure 15 | Evaluation of toxicity of tetrandrine, SG-005 and SG-094. (a-d) Toxicity of tetrandrine, SG-005 and SG-094 to non-cancerous cells was probed by treating (a) HepaRG progenitor, (b) differentiated HepaRG and (c) peripheral blood mononuclear cells (PBMCs) with 10 μ M and 20 μ M of the corresponding compound for 24 h. (a,b) Cell viability was assessed by CellTiter-Blue[®] cell viability assay and was normalized to vehicle control. Bar graphs indicate mean \pm SEM of three independent experiments (One-Way ANOVA followed by Tukey's multiple comparison test, * P < 0.05, ** P < 0.01). (c) Cell viability was quantified by propidium iodide staining and flow cytometry after treatment of peripheral blood mononuclear cells (PBMCs) with 10 μ M and 20 μ M of the corresponding compound for 48 h. Bar graphs indicate mean \pm SEM of three different donors (One-Way ANOVA followed by Tukey's multiple comparison test, ** P < 0.01, *** P < 0.001). PBMCs were isolated, cultivated and treated by Franz Geisslinger (Master Thesis). (d) Differentiated HepaRG cells were transfected with CYP3A4-EGFP or an empty vector control using Lipofectamine[™] 3000 reagent before treatment with 10 μ M of tetrandrine, SG-005 and SG-094 for 24 h. Specific cell death was assessed by propidium iodide staining and flow cytometry. (e,f) HepG2 cells (e) stably or (f) transiently expressing CYP3A4-EGFP or an empty vector control were treated with 10 μ M of tetrandrine, SG-005 and SG-094 alone or in combination with the CYP3A4 inhibitor ketoconazole (KCZ) for 24 h. (e,f) Cell death was assessed by propidium iodide staining and flow cytometry. Data in (d-f) are displayed as mean \pm SEM of three independent experiments (One-Way ANOVA followed by Tukey's multiple comparison test, ns, not significant).

4.1.2.4 SG-094 reduces tumor growth in a murine HCC model

Apart from the outlined toxicity issues, *in vivo* use of tetrandrine is limited due to its poor solubility and some authors describe the need for dissolving it in acidified solutions before dosage^{24, 27, 102, 103}. Hence, the tetrandrine congeners SG-005 and SG-094 were evaluated for their therapeutic potential in an ectopic mouse model using C57Bl/6-Tyr mice and RIL175 HCC cells. Dosing was adapted from a published dose of 100 mg/kg bodyweight (161 nmol/kg) for tetrandrine²⁷ and adjusted by their reduced IC₅₀ values, plus a second regimen with a 50 % higher dose (SG-005: 38 nmol/kg and 57 nmol/kg, SG-094: 59 nmol/kg and 90 nmol/kg). As mouse weight remained constant among all groups over the initial dose-finding period (**Supplementary Figure 8**) and no solubility issues without acidification of the injection solutions occurred, SG-005 was finally administered intraperitoneally (i.p.) at 57 nmol/kg and SG-094 at 90 nmol/kg every 2-3 days over a 10-day timescale (**Figure 16 a-d**). Due to the known toxicity problems, tetrandrine was not

Results

used *in vivo*. To exclude effects of SG-005 or SG-094 treatment on accumulation of D-luciferin in the engrafted tumors related to altered blood supply, tumor volume was measured simultaneously using a caliper (**Figure 16 b**) in addition to bioluminescence imaging (**Figure 16 a,d**). Notably, 10 days post engraftment of RIL175 cells, average bioluminescence signals in the SG-094 arm were decreased by 42 % (not significant) (**Figure 16 a,d**) and average tumor volume in the SG-094 arm was decreased by 33 % (significant) (**Figure 16 b**). Concurrently, no weight loss (**Figure 16 c**) or changes in health or behavior of the mice were observed and no acidification of the injection solution was required. In contrast, the administered dose of SG-005 was not sufficient to markedly suppress tumor growth (**Figure 16 a,b**).

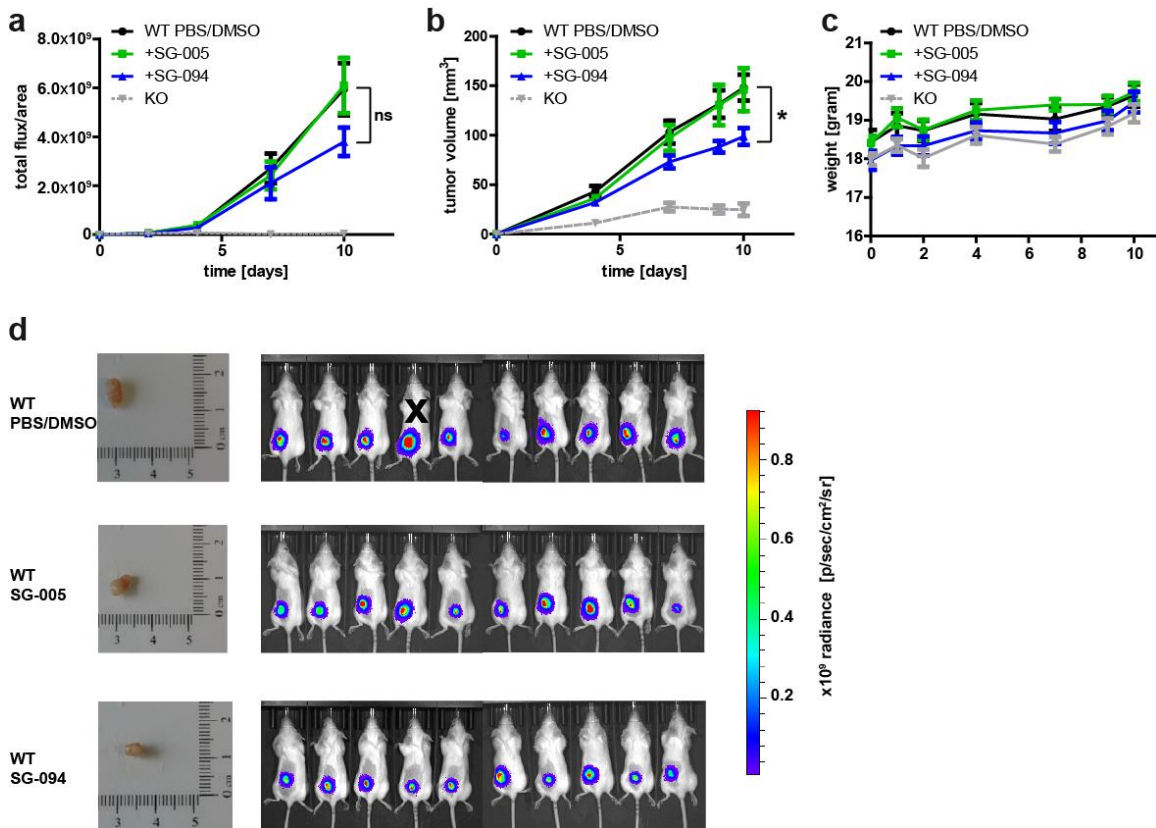


Figure 16 | SG-094 reduces tumor growth *in vivo*. (a-d) RIL175 WT cells were implanted into the flanks of C57Bl/6-Tyr mice. SG-005 and SG-094 were administered intraperitoneally (i.p.) at 57 nmol/kg and at 90 nmol/kg, respectively, every 2-3 days over a 10-d period, starting on the day of implantation. Line graphs indicate (a) bioluminescence signal intensities and (b) tumor volumes over time. (a,b) Engrafted tumors derived from TPC2 KO cells are displayed as dashed line for comparison. (a) Data are presented as mean \pm SEM ($n=9$ for WT PBS/DMSO, $n=10$ for other treatment arms, outlier identified with Grubbs' test and $\alpha=0.05$, One-Way ANOVA followed by Dunnett's multiple comparison test, ns, not significant). (b) Data are presented as mean \pm SEM ($n=9$ for SG-094, $n=10$ for other treatment arms, outlier identified with Grubbs' test and $\alpha=0.05$, One-Way ANOVA followed by Dunnett's multiple comparison test, $*P < 0.05$). (c) Mouse weight from (a,b) is shown over time as mean \pm SEM ($n=10$). (d) Bioluminescence images taken on day 10 are shown. The outlier is marked with an x. One excised tumor is exemplarily shown for each group.

4.1.3 TPC2 knockout or inhibition impairs phosphorylation of Akt and hexokinase II *in vivo*

As shown above, TPC2 KO and inhibition favor oxidative phosphorylation instead of glycolysis (**Figure 9, Figure 14**). Hexokinase II (HK II) has a key role in regulating glycolytic flux in cancer⁸² and, thus, we investigated whether the enzyme is involved in the observed metabolic switch. Apart from transcriptional activation⁸², glycolysis can be regulated by phosphorylation of HK II, resulting in increased protein stability and mitochondrial binding, which in turn promotes glycolysis, proliferation and cell survival of cancer cells as well as tumor growth¹⁰⁴. By immunoblotting, two bands were detected for HK II, of which the upper one was assigned to the phosphorylated form by comparison with the lysate after dephosphorylation (**Figure 17 a,b**). Levels of phosphorylated HK II were strongly reduced in tumors formed by TPC2 KO cells. Translocation and phosphorylation of HK II can be facilitated by growth factors via PI3K-AKT signaling^{105, 106}, a pathway that can be impaired by TPC2 knockdown or inhibition (**Figure 13 a,b** and literature^{13, 107}). Indeed, protein levels of p-AKT were reduced in tumors from SG-094-treated mice and from TPC2 KO tumors (**Figure 17 a,b**). We propose that TPC2 affects important metabolic circuits in cancer cells by posttranslational modification of HK II via reduced AKT signaling and thus provide important information on mechanistic pathways linking TPC2 and cellular metabolism.

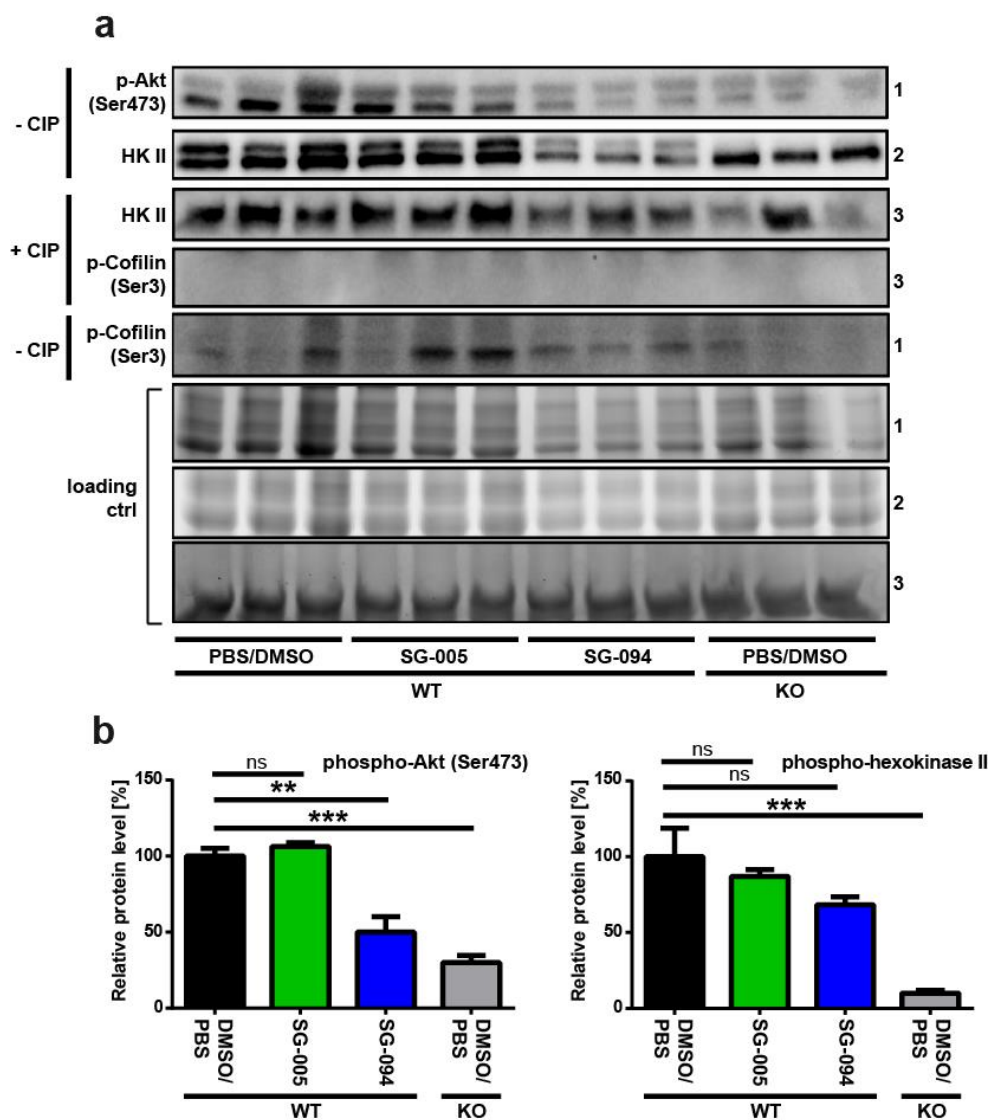


Figure 17 | TPC2 knockout reduces phosphorylation of Akt and hexokinase II *in vivo*. (a,b) C57Bl/6-Tyr mice were implanted with RIL175 WT or RIL175 TPC2 KO cells and treated as described for **Figure 8** and **Figure 16**. Protein levels of p-Akt (Ser473) and hexokinase II in the tumors were analyzed by western blotting. (a) Except for the TPC2 KO tumors, two bands were detected for hexokinase II, which converged into one band after dephosphorylation of the protein lysates with calf intestinal phosphatase (CIP), indicating that the upper band is the phosphoprotein. P-Cofilin (Ser3) served as control for the dephosphorylation reaction. (b) Quantitative evaluation of protein levels from (a) in the absence of CIP is shown. Proteins of interest were normalized to whole lane protein and are presented as percentage relative to vehicle control. The experiment was performed in triplicate and the bar graphs indicate mean \pm SEM (One-Way ANOVA followed by Dunnett's multiple comparison test).

4.1.4 Tetrandrine toxicity is independent of CYP3A4 expression *in vitro*

Several studies in the literature suggest that the hepatotoxicity and pulmonary toxicity of tetrandrine^{27, 94} (4.1.2.3) and related bisbenzylisoquinoline alkaloids, such as dauricine¹⁰⁸ and berbamine¹⁰⁹, is partly caused by metabolic activation by CYP3A4 and CYP3A5. More specifically, the authors proposed that through CYP3A4/5 oxidation, electrophilic

Results

metabolites (*para*-quinone methides) are generated (**Figure 18**), which they considered as major cause for cytotoxicity *in vitro* and pulmonary or hepatic damage in mice or rats^{27, 94, 108, 109}.

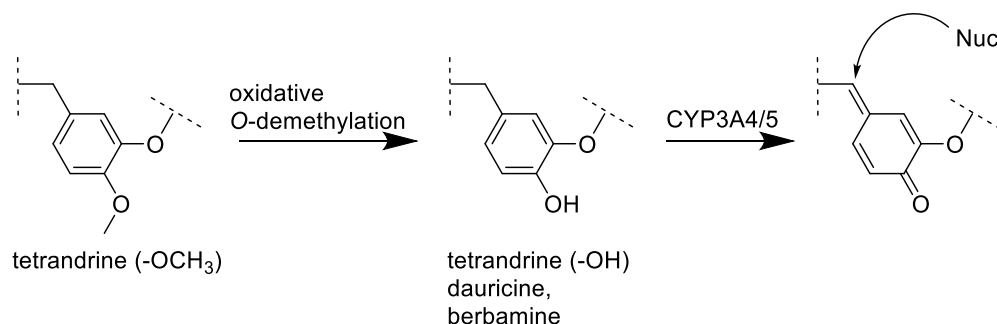


Figure 18 | Postulated metabolic activation and toxification of tetrandrine, dauricine and berbamine, according to Jin *et al.*²⁷, Jin *et al.*¹⁰⁸ and Sun *et al.*¹⁰⁹. Following oxidative O-demethylation by Cytochrome P450 (P450s) enzymes (not specified in more detail), CYP3A4 and CYP3A5 are hypothesized to equally oxidize the phenol to form a *para*-quinone methide, which is prone to attack bio-nucleophiles (Nuc). The phenols dauricine and berbamine do not require the demethylation step.

In a combined medicinal chemistry and cell biology approach we evaluated if a reduction of the discussed CYP3A4-mediated toxicity of tetrandrine can be achieved by replacing or eliminating the hypothesized metabolically instable 12-methoxy group. We designed analogues of tetrandrine, in which this methoxy group is either deleted (RMS1-2) or replaced by metabolically stable trifluoromethoxy (RMS3-4) or chlorine substituents (RMS9-10) (**Figure 19**). Further, we replaced the methoxybenzyl residue by a thienylmethyl (RMS5-6) and by a non-aromatic butylidene unit (RMS7-8). Chemical synthesis was conducted by Ramona Schütz (Prof. Bracher, LMU Munich). Subsequently, the effects of the obtained tetrandrine analogues RMS1-RMS10 on HepaRG™ and HepG2 cells, with or without overexpression of CYP3A4, were investigated.

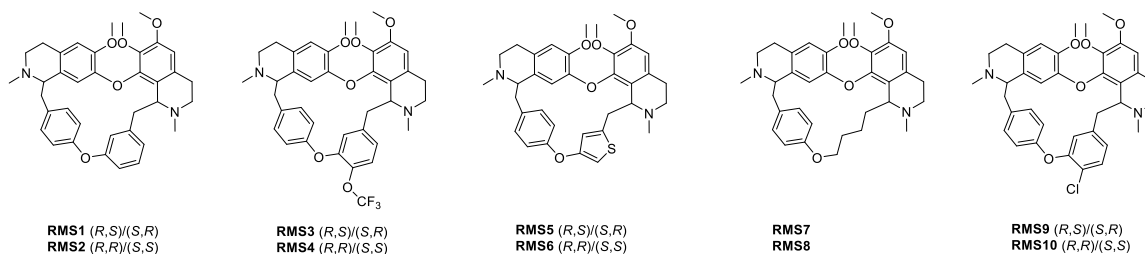


Figure 19 | Chemical structures of RMS1-RMS10. Various tetrandrine analogues (RMS1-RMS10) containing metabolically stable substituents were synthesized by Ramona Schütz (Prof. Bracher, LMU Munich).

To start with, differentiated HepaRG™ cells having high P450 activity^{96, 97}, were treated with 10 and 20 μM of tetrandrine and RMS1-10. Unlike expected, none of the new compounds was less toxic to HepaRG™ cells than tetrandrine at 10 μM (**Figure 20 a**). In

contrast, RMS4 and RMS10 slightly, but RMS2 strongly decreased cell viability. Similarly, at 20 μ M, RMS2, RMS4 and RMS10 were significantly more toxic to HepaRGTM cells than tetrandrine (**Figure 20 b**). Of note, 20 μ M of RMS6 and RMS7 were significantly less toxic than tetrandrine, whereas toxic effects of the other compounds did not substantially differ from those of tetrandrine (**Figure 20 b**). It should be noted that, depending on the substituent at C-12 of ring C, oxidation to a *para*-quinone methide cannot be excluded for 12-unsubstituted compounds RMS1/RMS2 (*via* initial CYP-mediated ring hydroxylation), whereas in trifluoromethoxy compounds RMS3/RMS4 and chloro compounds RMS9/RMS10 oxidation processes are prevented by metabolically stable substituents. To specifically determine the influence of CYP3A4 activity on toxicity *in vitro*, CYP3A4 with a C-terminal EGFP tag was cloned (CYP3A4-EGFP) and its physiological function was successfully validated by conversion of a proluminogetic CYP3A4 substrate in transiently transfected HepG2 cells, which was strongly reduced by the CYP3A4 inhibitor ketoconazole⁹⁹ (**Supplementary Figure 9 a**). Of note, treatment of CYP3A4 overexpressing HepaRGTM cells with respective compounds did not significantly increase cell death (**Figure 20 c**). As observed for the non-transfected HepaRGTM cells, RMS2 still had the strongest effect on cell viability.

Next, transgenic HepG2 cells, a liver cancer cell line frequently used for recombinant expression of CYP enzymes and hepatotoxicity studies^{98, 99, 101}, were generated. Stable transfection and overexpression of CYP3A4 were confirmed by PCR methods (**Supplementary Figure 9 b,c**). Again, no correlation between the level of cellular CYP3A4 expression and cytotoxicity was observed (**Figure 20 d**). Interestingly, most tetrandrine analogues (RMS1, RMS2, RMS3, RMS4, RMS5, RMS9, RMS10) exerted generally increased cytotoxicities against cancerous HepG2 cells, mostly independent of their stereochemistry, in comparison to tetrandrine (**Figure 20 d**). Surprisingly, the diastereomers RMS9 and RMS10 slightly, while RMS5 and RMS6 substantially differed in their cytotoxic potencies. Of note, RMS3 and RMS5 influenced cell viability of HepaRGTM cells similarly to tetrandrine (**Figure 20 a,b**), but they exerted strongly increased cytotoxicities to cancerous HepG2 cells (**Figure 20 d**).

To exclude that the observed similar cytotoxic effects on vector and CYP3A4-EGFP transfected cells were caused by insufficient initial demethylation that is required for tetrandrine for being oxidized to a putatively toxic *para*-quinone methide (**Figure 18**), related alkaloids berbamine and dauricine were also tested. Both alkaloids bear a *para*-hydroxybenzyl moiety at the region of interest (**Figure 10 a, Figure 18**), which theoretically can be oxidized directly by CYP3A4 to a *para*-quinone methide with no need for previous

O-demethylation. Similarly, for both berbamine and dauricine, cell death was not significantly increased by cellular CYP3A4 overexpression (**Figure 20 d**).

Taken together, the toxicity of tetrandrine was not considerably decreased or even increased by variation of the *para*-methoxybenzyl moiety in several cellular models. However, no influence of the level of cellular CYP3A4 expression was found. Consequently, we conclude that the proposed CYP3A4-mediated generation of a *para*-quinone methide¹¹⁰ does not substantially contribute to the hepatotoxicity of tetrandrine. This piece of work is intended to be published in the European Journal of Medicinal Chemistry (Elsevier) (accepted).

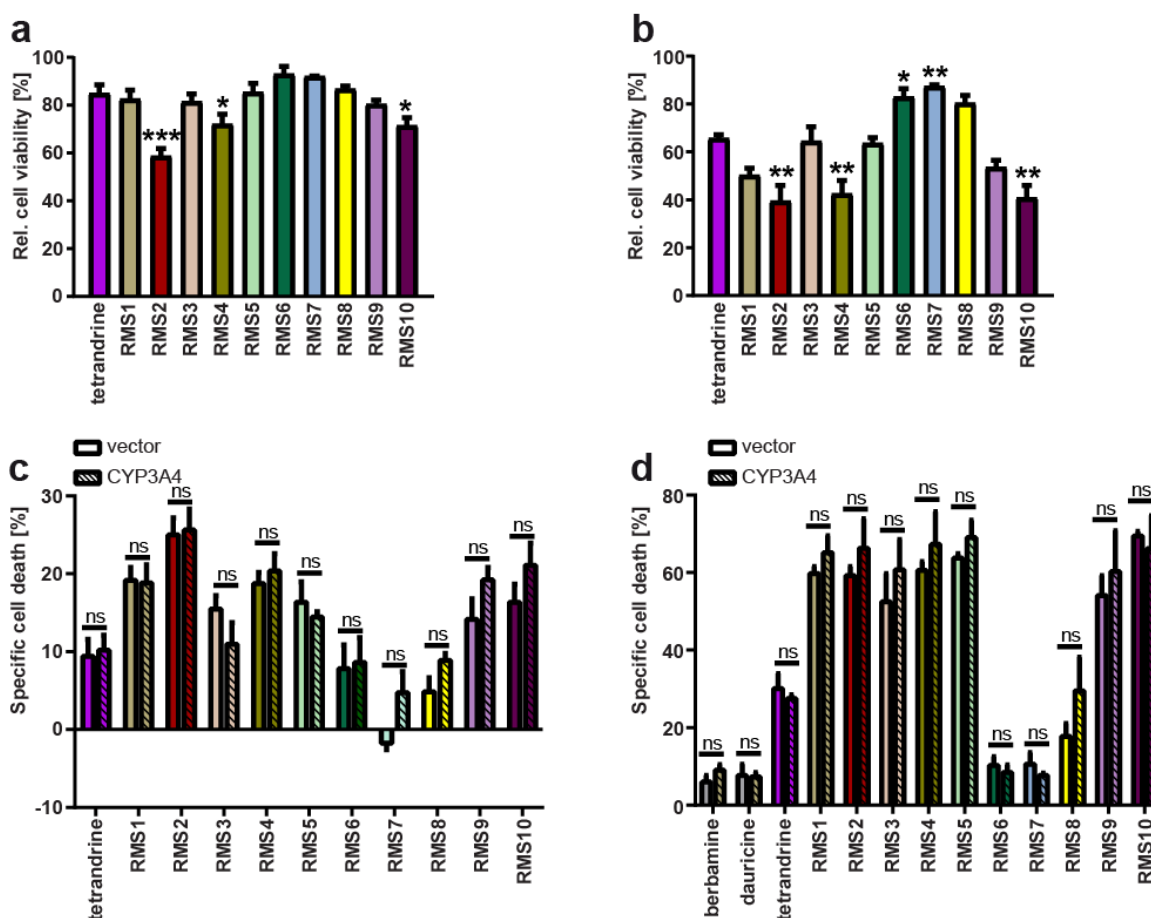


Figure 20 | Evaluation of toxicity of tetrandrine and the tetrandrine analogues RMS1-RMS10. (a,b) Toxicity of tetrandrine, SG-005 and SG-094 to non-cancerous cells was probed by treating differentiated HepaRG cells with (a) 10 μM and (b) 20 μM of the corresponding compound for 24 h. (a,b) Cell viability was assessed by CellTiter-Blue® cell viability assay and was normalized to vehicle control. Bar graphs indicate mean ± SEM of three independent experiments (One-Way ANOVA followed by Dunnett's multiple comparison test, * $P < 0.05$, ** $P < 0.01$, *** $P < 0.001$). (c) Differentiated HepaRG cells were transfected with CYP3A4-EGFP or an empty vector control using Lipofectamine™ 3000 reagent before treatment with 10 μM of tetrandrine or RMS1-RMS10 for 24 h. (d) HepG2 cells stably expressing CYP3A4-EGFP or an empty vector control were treated with 15 μM of berbamine, dauricine, tetrandrine, or RMS1-RMS10 for 24 h. (c,d) Specific cell death was assessed by propidium iodide staining and flow cytometry. Bar graphs indicate means ± SEM of three independent experiments (One-Way ANOVA followed by Tukey's multiple comparison test, ns, not significant).

4.1.5 TPC2 blockers also act as P-gp inhibitors and *vice versa*

4.1.5.1 Simplified tetrandrine congeners inhibit P-gp

Apart from TPC2 inhibition, numerous other biological activities and molecular targets are described for tetrandrine¹¹¹. By inhibiting the efflux pump P-gp, it was shown to sensitize resistant tumor cells to cytostatics³³ and, thus, it has entered early phase clinical studies under the brand name CBT-1^{®34, 35}. Therefore, we investigated the influence of the tetrandrine congeners SG-005 and SG-094 on the accumulation of the P-gp model substrate calcein-AM (**Figure 21 a**) in vincristine-resistant CEM (VCR-R CEM) cells, leukemia cells that overexpress P-gp⁷⁰. Similar to tetrandrine and the positive control verapamil, SG-005 and SG-094 dose-dependently increased calcein fluorescence, suggesting that they act as direct P-gp inhibitors (**Figure 21 b**). Accordingly, combination of the P-gp substrate VCR with tetrandrine, SG-005 and SG-094 sensitized VCR-R CEM cells towards VCR when analyzing proliferation (**Figure 21 c**) and cell death dose-response curves (**Figure 21 d**). Additionally, immunoblotting confirmed enhanced apoptosis, indicated by cleavage of poly (ADP-ribose) polymerase (PARP) and activation of caspase 3 (**Figure 21 d**). Consequently, tetrandrine and its simplified congeners SG-005 and SG-094 share TPC2 and P-gp as mutual targets.

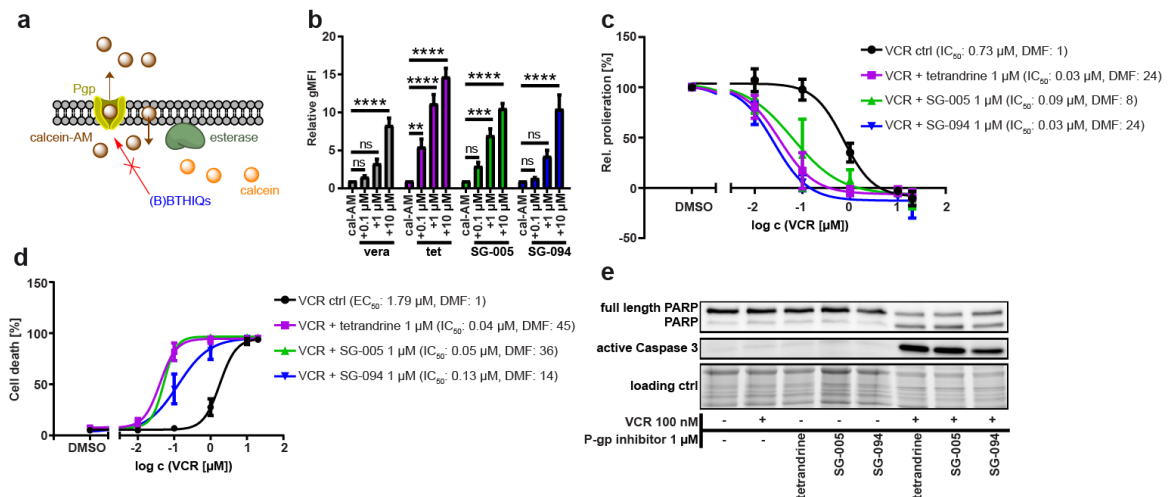


Figure 21 | Tetrandrine, SG-005 and SG-094 inhibit P-gp and sensitize VCR-R CEM cells to VCR. (a) Scheme illustrating the calcein-AM retention assay. (b) Retention of the P-gp model substrate calcein-AM in vincristine-resistant CEM (VCR-R CEM) cells was determined by flow cytometry. Cells were incubated with calcein-AM, in presence or absence of increasing concentrations of tetrandrine, SG-005, SG-094 and the positive control verapamil (vera) (0.1, 1, 10 μM). Bar graph displays means ± SEM of three independent experiments (One-Way ANOVA followed by Tukey's multiple comparison test, ns, not significant, ** $P < 0.01$, *** $P < 0.001$). (c,d) Dose-response curves of VCR-R CEM cells, treated with VCR alone or in combination with 1 μM of tetrandrine, SG-005 and SG-094 for 48 h are shown. (c) Antiproliferative effects were determined by CellTiter-Blue[®] cell viability assay and (d) cell death was assessed by propidium iodide staining and flow cytometry. (e) Cleavage of PARP and activation of caspase 3 in VCR-R CEM cells, treated with either VCR (100 nM) alone or in combination with tetrandrine, SG-005 or SG-094 (1 μM) were analyzed by western blotting.

4.1.5.2 Third generation P-gp inhibitor elacridar is a potent TPC2 blocker

As the newly identified TPC2 blockers, SG-005 and SG-094, were found to also inhibit P-gp (4.1.5.1), we investigated whether elacridar, a third generation P-gp and BCRP (breast cancer resistance protein) inhibitor that was co-administered with topotecan and doxorubicin in clinical phase I trials^{41, 42}, is a TPC2 antagonist. Elacridar bears a tetrahydroisoquinoline moiety, but, unlike all bisbenzylisoquinolines and truncated variants that were used in this study, elacridar lacks the 1-benzyl or 1-phenyl substituent and a chiral center (**Figure 22 a**). Of note, elacridar strongly reduced PI(3,5)P₂-evoked TPC2 currents in TPC2-EGFP-transfected HEK293 cells (**Figure 22 b**). When compared with tetrandrine, elacridar treatment led to a significantly increased channel inhibition (75 % vs. 54 %) (**Figure 22 c**). Hence, the effect of elacridar on cancer cell proliferation was investigated. While colon adenocarcinoma cells (HCT-15) were barely affected, elacridar moderately inhibited proliferation of hepatocellular carcinoma (HepG2, IC₅₀: 17.1 μM) and bladder carcinoma (T24, IC₅₀: 24.6 μM) cells (**Figure 22 d**). Thus, an extensively investigated P-gp inhibitor with minimal side effects in humans⁴¹ could be repurposed as a potent TPC2 blocker with moderate antiproliferative properties. Further, due to the low structural similarities with known TPC2 antagonists, elacridar was identified as new chemical lead structure.

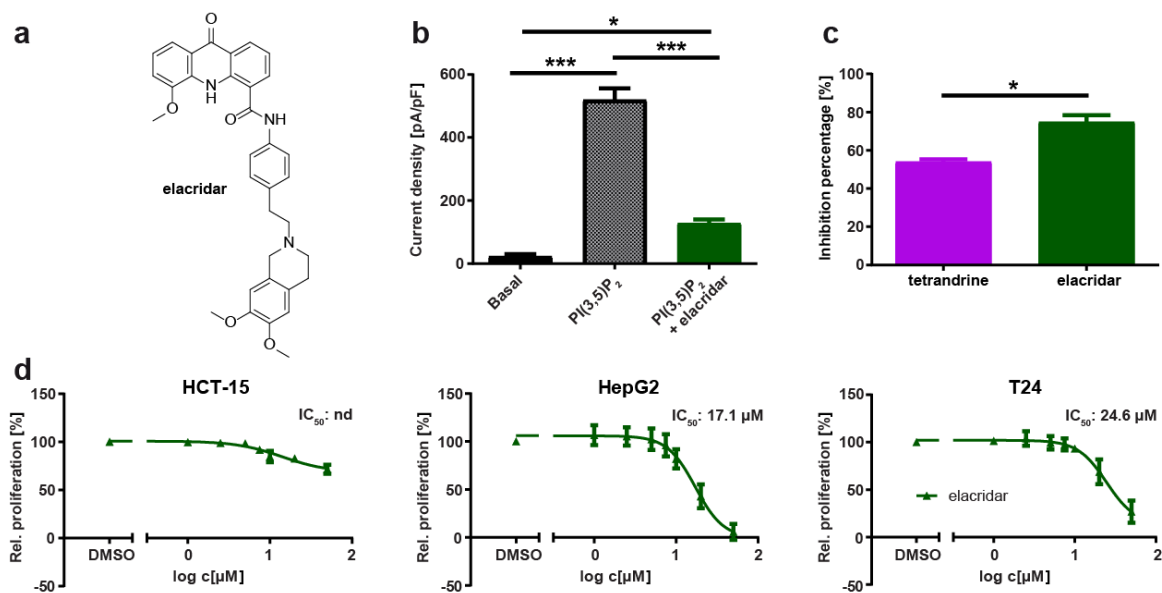


Figure 22 | Elacridar is a potent TPC2 antagonist and a moderate inhibitor of cancer cell proliferation. (a) The chemical structure of elacridar is shown. (b,c) 10 μM of tetrandrine or elacridar were applied upon activation with 1 μM of PI(3,5)P₂ on isolated and vacuolin-enlarged endolysosomes from HEK293 cells expressing TPC2-EGFP. (b) Elacridar strongly blocks PI(3,5)P₂-elicited TPC2 currents. Bar graph presents means ± SEM of at least three independent experiments (One-Way ANOVA followed by Tukey's multiple comparison test, *P < 0.05, ***P < 0.001). (c) The inhibition percentage of tetrandrine and elacridar is displayed. The bar graph indicates means ± SEM of at least two independent experiments (unpaired t-test, *P < 0.05). Patch clamp experiments were performed by Yu-Kai Chao (Prof. Grimm, LMU Munich). (d) Antiproliferative effects of elacridar on colorectal adenocarcinoma (HCT-15), hepatocellular carcinoma (HepG2) and bladder carcinoma (T24) cell lines were determined by CellTiter-Blue[®] assay. Cells were incubated with for 72 h and proliferation is shown as percentage of vehicle control. Line graphs display means ± SEM of three independent experiments.

4.1.6 TPC2 function impacts chemoresistance of P-gp overexpressing cells

As outlined in chapter 4.1.5, there is a clear overlap between pharmacological TPC2 and P-gp inhibitors. Since Al-Akra and coworkers⁴⁶, among others, recently suggested that P-gp can be trafficked to the endolysosomal system to promote the lysosomal safe house effect, we investigated whether or not there is a functional connection between TPC2 and P-gp. As RIL175 cells failed to markedly retain calcein-AM *via* P-gp (**Supplementary Figure 10 a**), P-gp overexpressing VCR-R CEM cells⁷⁰ were chosen as capable model to study the implication of TPC2 in P-gp-mediated drug resistance. Firstly, elevated TPC2 mRNA expression in VCR-R CEM cells in comparison to parental, non-resistant CCRF CEM cells was determined by qPCR, indicating that TPC2 plays a role in multidrug resistance (**Figure 23 a**). Secondly, we aimed to delete TPC2 in VCR-R CEM cells using CRISPR-Cas9 and a single sgRNA approach. An InDel (insertion or deletion of bases) in exon 16 (thymidine insertion) was detected by Sanger sequencing (**Supplementary Figure 10 b**), leading to a pre-mature stop codon (**Supplementary Figure 10 c**). 5' mRNA levels were decreased by ~82 %, suggesting NMD as a response to the InDel formation

(**Supplementary Figure 10 d**). In patch clamp experiments, PI(3,5)P₂-elicited currents of enlarged lysosomes obtained from TPC2 KO cells were decreased, suggesting loss of channel function (**Supplementary Figure 10 e**). All seven predicted off-target sequences for each sgRNA were analyzed by Sanger sequencing and no InDels were found for the investigated clone (Master Thesis Franz Geisslinger, data not shown). Theoretically, despite the presence of NMD and the observed reduced channel activation by PI(3,5)P₂, a minimal residual PI(3,5)P₂ activity cannot be fully excluded as the binding site of the phosphoinositide is located to an earlier exon. Therefore, it remains to be verified if the described thymidine insertion leads to a successful KO or a stable knockdown, e.g. by additional recordings of channel currents upon activation with synthetic TPC2 activators⁶. Nonetheless, TPC2-deficient cells are referred to as KO cells in this work and they were studied further. In agreement with the impact of loss of TPC2 function in RIL175 cells, proliferation of TPC2-deficient VCR-R CEM cells was strongly impaired, as evident by counting of cell numbers over time (**Figure 23 b**) and an increase in doubling time from 23 h to 31 h (**Figure 23 c**). Notably, TPC2 KO led to an increased sensitivity towards VCR-induced apoptosis (WT EC₅₀: 3.0 μM, KO EC₅₀: 1.7 μM, **Figure 23 d**). Likewise, they were more responsive to VCR treatment than their WT counterpart, as evident by a reduced IC₅₀ value (WT IC₅₀: 3.3 μM, KO IC₅₀: 1.6 μM) in a cell proliferation assay (**Figure 23 e**). Thus, these data indicate that interfering with TPC2 function reduces proliferation not only of solid cancer cells, but also of leukemic cells, and that it contributes to the reversal of P-gp-mediated drug resistance.

Results

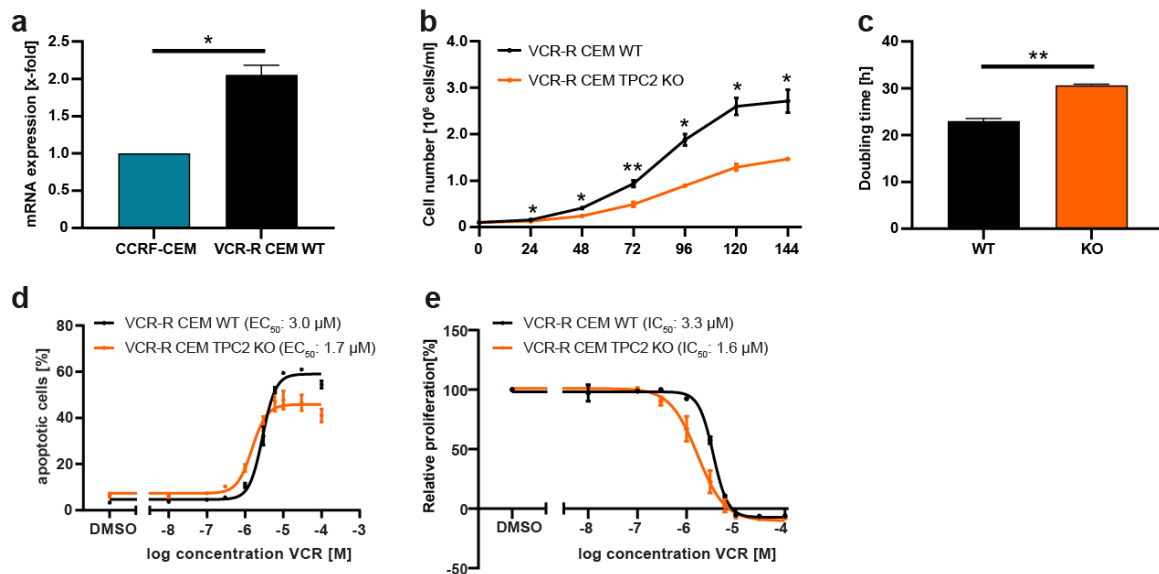


Figure 23 | Loss of TPC2 function decreased proliferation of VCR-R CEM cells and sensitized them to VCR treatment. (a) Increased mRNA expression of TPC2 in VCR-R CEM WT vs. non-resistant, parental CCRF CEM cells was detected by qPCR. (b,c) Counting of cells over 144 h indicated reduced proliferation rate of VCR-R CEM TPC2 KO vs. WT cells. (c) Calculation of the doubling time from (b). (a-c) Bar and line graphs display means \pm SEM of three independent experiments (unpaired t-test with Welch's correction, * $P < 0.05$, ** $P < 0.01$). (d,e) TPC2-deficient cells are more sensitive towards vincristine (VCR). (d) Apoptosis of VCR-R CEM WT vs. KO cells was quantified by propidium iodide staining and flow cytometry following 48 h of VCR treatment. (e) The impact of VCR treatment on proliferation of VCR-R CEM WT and KO cells was assessed by CellTiter-Blue® assay. Cells were incubated with VCR for 72 h and proliferation is shown as percentage of vehicle control. (d,e) Line graphs display means \pm SEM of three independent experiments. (a-e) Experiments were conducted by Franz Geisslinger (Master Thesis).

4.1.7 Combination with benzylisoquinolines is beneficial in sorafenib-resistant hepatocellular carcinoma cells

Since genetic TPC2 KO and pharmacological TPC2/P-gp inhibition successfully sensitized VCR-R CEM cells to VCR (4.1.5, 4.1.6), tetrandrine, SG-005 and SG-094 were investigated in another cell model, sorafenib-resistant HUH7 cells. The orally administered multi-kinase inhibitor sorafenib was the first worldwide approved systemic therapy for unresectable HCC¹¹². However, resistance to sorafenib remains a problem to date and, therefore, Meßner *et al.* (Prof. Pachmayr, PMU Salzburg) have generated sorafenib-resistant HUH7 cells (HUH7-R) which tolerate clinically relevant peak concentrations of sorafenib (8.5–15.7 μ M¹¹³). As we have described earlier, those HUH7-R cells are broadly cross-resistant to various other cytostatic and cytotoxic agents, which is independent of P-gp activity¹¹⁴. Characterization of HUH-R cells has revealed, among others, a higher glycolytic phenotype, increased lysosomal volume and elevated cytosolic Ca²⁺ levels in comparison to HUH7 WT¹¹⁴. This invited us to test if a combination treatment with tetrandrine, SG-005 or SG-094 was able to reverse resistance of HUH-R cells to sorafenib. Notably, low micromolar concentrations of all three tested compounds were able to

considerably reduce HUH-R cell growth in combination with 10 μM sorafenib (**Figure 24 a**). SG-005 (IC_{50} : 0.7 μM) and SG-094 (IC_{50} : 2.1 μM) achieved significant reduction of cell proliferation at lower concentrations than tetrandrine (IC_{50} : 5.8 μM), while SG-005 showed the most potent effect (**Figure 24 b,c**). Real-time impedance measurements were performed by Martina Meßner (Prof. Pachmayr, PMU Salzburg). Whether or not this effect is predominantly mediated by TPC2 inhibition remains to be elucidated by gene silencing or knockout experiments.

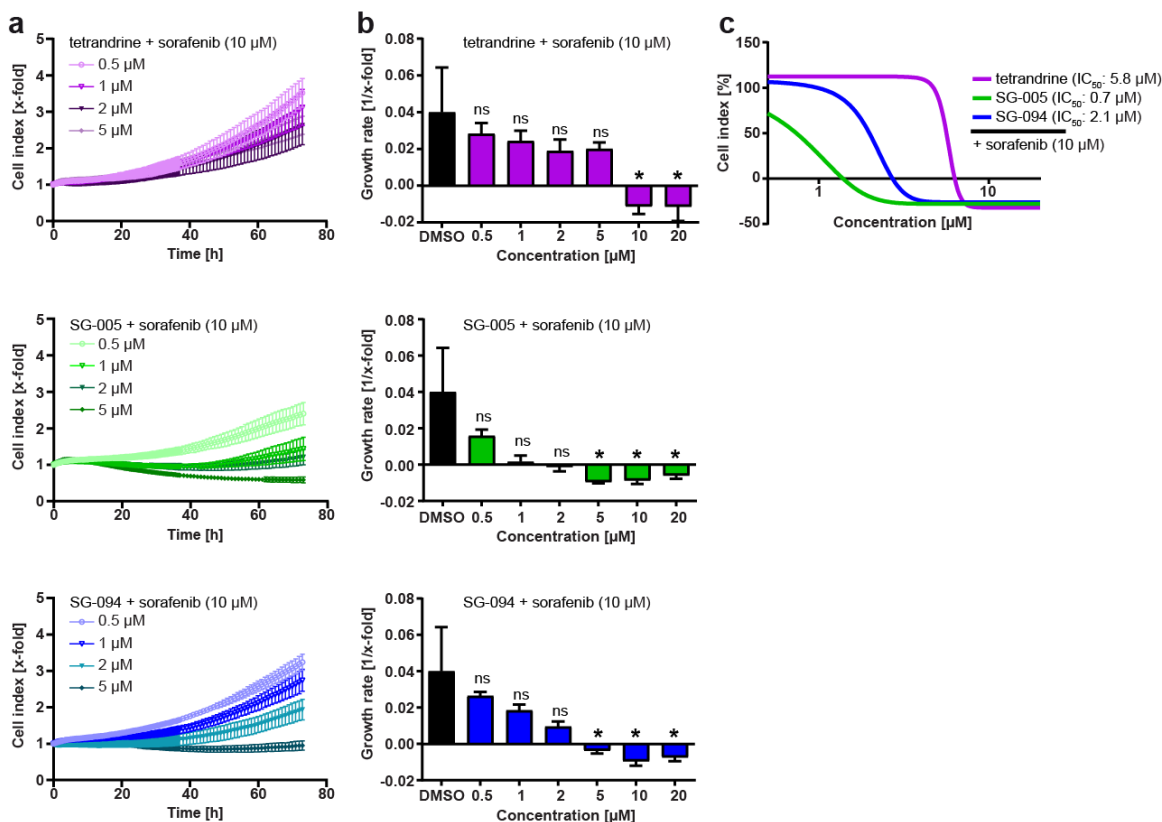


Figure 24 | Combination of sorafenib with tetrandrine, SG-005 and SG-094 re-sensitized sorafenib-resistant HUH7 (HUH7-R) cells. (a-c) Proliferation of HUH7-R cells, treated with sorafenib (10 μM) and increasing concentrations of tetrandrine, SG-005 and SG-094, was observed by real-time impedance measurements. Experiments and data analysis were conducted by Martina Meßner (Prof. Pachmayr, PMU Salzburg). (a) Cell growth of HUH7-R cells is shown as cell index over time as means \pm SEM of three independent experiments. Cell index was normalized to the treatment start. (b) The dose-dependent inhibition of growth rate by increasing concentrations of tetrandrine, SG-005 and SG-094 is displayed (One-Way ANOVA followed by Dunnett's multiple comparison test, * $P < 0.05$). (c) Dose-response curves, calculated from (a,b), are shown.

4.1.8 Biological characterization of the isoquinoline-benzylisoquinoline alkaloid muraricine

Based on the findings of this work, it is clearly obvious that bisbenzylisoquinolines and analogues thereof are highly interesting molecules. Thus, the discovery and characterization of novel bisbenzylisoquinolines can help to decipher their structure-

activity relationships and related targets. Recently, a novel bisbenzylisoquinoline alkaloid, muraricine, was isolated from *Berberis vulgaris* (Berberidaceae) by Hostalkova and colleagues¹¹⁵. In this *seco*-bisbenzylisoquinoline, a diaryl ether bridge connecting two isoquinoline units is still present, and formally one benzyl unit is lost (**Figure 25 a**). Therefore, muraricine can be regarded as an isoquinoline-benzylisoquinoline alkaloid and, based on analogy with related alkaloids, (*R*) configuration was postulated¹¹⁵. Apart from moderate butyrylcholinesterase inhibition in first investigations¹¹⁵, no pharmacological effects are known to date, which prompted us to investigate if *rac*-muraricine (muraricine), obtained by racemic total synthesis (performed by Ramona Schütz, Prof. Bracher, LMU Munich) possesses antiproliferative, toxic, TPC2 inhibitory, and multidrug resistance reversing properties¹¹⁶. Unlike the reference compound tetrandrine, muraricine showed only very low antiproliferative effects and no cytotoxic activity (**Figure 25 b**). Due to the known toxic effects of tetrandrine and other bisbenzylisoquinoline alkaloids, as outlined in chapters **4.1.2.3** and **4.1.4**, we investigated whether muraricine was toxic to non-cancerous cells. For that purpose, HUVECs were treated with 10, 20 and 50 μ M for 6 h and cell viability was assessed by quantifying intracellular ATP content. As expected, tetrandrine strongly and dose-dependently affected viability of HUVECs (**Figure 25 c**). In contrast, no significant toxicity to endothelial cells was observed upon muraricine treatment (**Figure 25 c**). In line with the observations from the screening of truncated tetrandrine analogues (**4.1.2.1**), removal of a second aromatic residue led to loss of inhibitory activity at TPC2, when subjected to single cell Ca^{2+} imaging (**Figure 25 d,e**).

Results

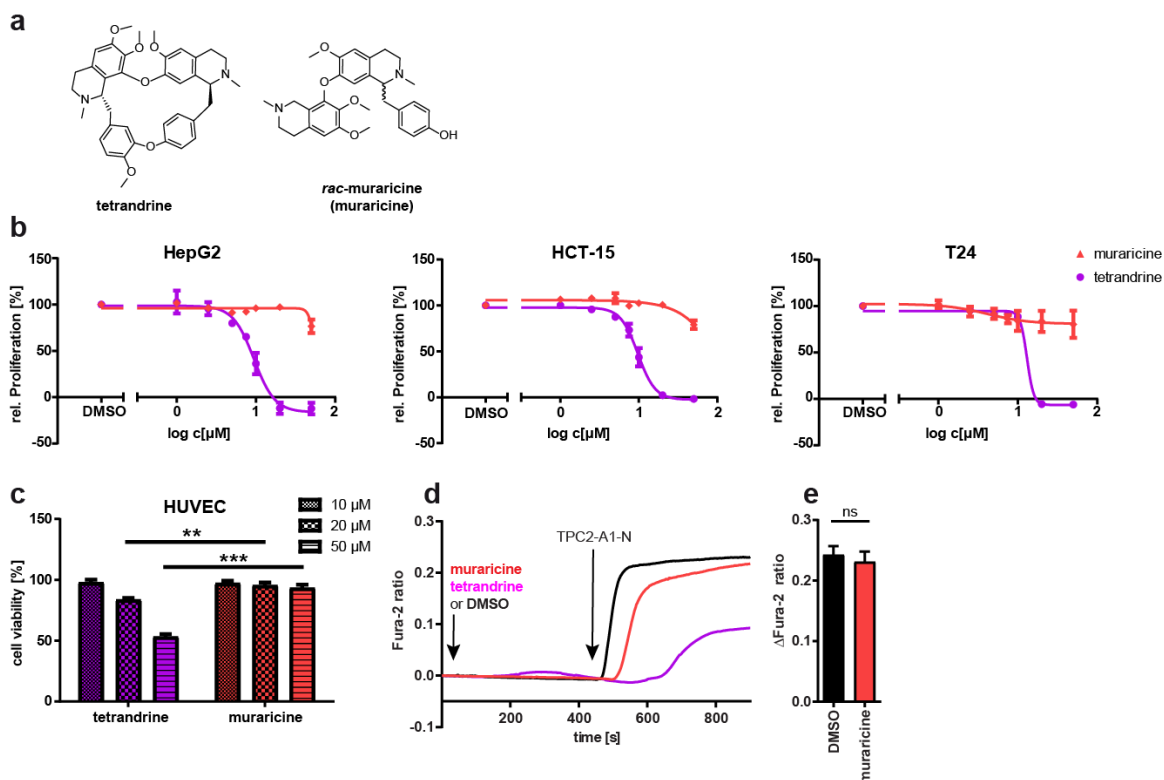


Figure 25 | Weak antiproliferative, toxic and TPC2 inhibitory potential of muraricine. (a) Chemical structures of tetrandrine and *rac*-muraricine (muraricine) are shown. (b) Antiproliferative effects of muraricine on hepatocellular carcinoma (HepG2), colorectal adenocarcinoma (HCT-15) and bladder carcinoma (T24) cell lines were determined by CellTiter-Blue[®] assay. Cells were incubated with the respective concentrations for 72 h and proliferation is shown as percentage of vehicle control after subtraction of the zero value. Tetrandrine served as control. Line graphs display means \pm SEM of three independent experiments. (c) Acute toxicity to non-cancerous human umbilical vein endothelial cells (HUVECs) is shown. Cells were treated for 6 h with muraricine and tetrandrine (10, 20, 50 μ M) for 6 h. Cell viability was determined by quantifying cellular ATP content applying a CellTiter-Glo[®] cell viability assay and is displayed as percentage of vehicle control as means \pm SEM of three independent experiments (One-Way ANOVA followed by Tukey's multiple comparison test, ** $P < 0.01$, *** $P < 0.001$). (d) Ca^{2+} imaging results of muraricine, tetrandrine and a DMSO control using the TPC2 activator TPC2-A1-N. Representative Ca^{2+} signals recorded from HEK293 cells stably expressing TPC2^{L11A/L12A}-RFP. After applying muraricine (10 μ M, $n = 19$ single cells), tetrandrine (1, 10 μ M, $n = 17$ single cells) or DMSO (0.1 % in HBS, $n = 16$ single cells) and monitoring the signal for 400 s, cells were stimulated with TPC2-A1-N (10 μ M) and further recorded for 400 s. (e) Statistical analysis of the maximal change in Fura-2 ratio is displayed as mean \pm SEM of at least two independent experiments (unpaired t-test, ns, not significant). Ca^{2+} imaging was performed by Susanne Gerndt (Prof. Bracher, LMU Munich).

As pointed out, muraricine does not cause direct antitumor effects. Hence, we aimed to evaluate its potential as add-on in combination therapy. As inhibition of P-gp could be shown for the *seco*-analogues of tetrandrine, SG-005 and SG-094 (4.1.5.1), we investigated the influence of muraricine on the accumulation of the P-gp model substrate calcein-AM in VCR-R CEM cells. We found a dose-dependent increase of calcein fluorescence (Figure 26 a,b). Although the inhibition of P-gp-mediated calcein-AM efflux was weaker than that of the known inhibitor verapamil (Figure 26 a,b), P-gp could be identified as target of muraricine. Verapamil was used as positive control since the treatment did not affect cell viability under the chosen conditions. To test if a combination

of vincristine with muraricine provides a therapeutic benefit, apoptosis of VCR-R CEM cells was evaluated. For both tested concentrations of vincristine (0.1 and 1 μM), significantly increased apoptosis rates were detected when it was combined with non-toxic concentrations of muraricine (25 μM) (**Figure 26 c**). Taken together, these results demonstrate that muraricine represents a non-toxic *seco*-analogue of tetrandrine without direct effects on TPC2 or cancer cell proliferation, but with the potential to overcome drug resistance in cancer. This work was published in the journal *Archiv der Pharmazie* (Wiley-VCH Verlag GmbH & Co. KGaA on behalf of Deutsche Pharmazeutische Gesellschaft) in 2020¹¹⁶.

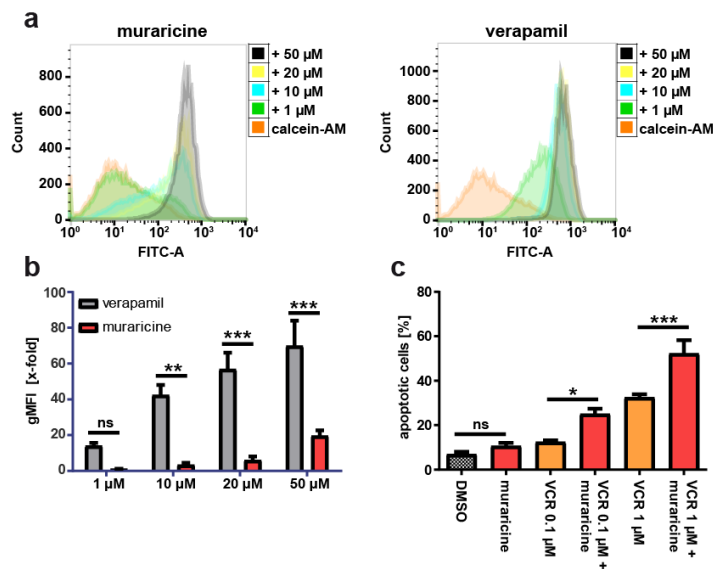


Figure 26 | Muraricine inhibits P-gp and provides a therapeutic benefit in combination therapy. (a,b) Retention of the P-gp model substrate calcein-AM in vincristine-resistant CEM (VCR-R CEM) cells was determined by flow cytometry. Cells were incubated with calcein-AM, in presence or absence of increasing concentrations of muraricine and the positive control verapamil (1, 10, 20, 50 μM). (a) Histograms of cell populations are shown. The experiment was performed in triplicate and one representative experiment is shown. (b) Quantification and statistical analysis of data from (a,b). Bar graph displays means \pm SEM of three independent experiments (One-Way ANOVA followed by Tukey's multiple comparison test, ns, not significant, ** $P < 0.01$, *** $P < 0.001$). (c) The Percentage of apoptotic cells is shown. VCR-R CEM cells were treated with vincristine (VCR, 0.1 and 1 μM) with or without muraricine (25 μM) for 48 h. Apoptotic cells were quantified by propidium iodide staining and flow cytometry. Bar graph displays means \pm SEM of three independent experiments (One-Way ANOVA followed by Tukey's multiple comparison test, ns, not significant, * $P < 0.05$, *** $P < 0.001$).

4.1.9 Part I: Summary

Here, we describe that genetic TPC2 knockout using CRISPR-Cas9 reduces cell proliferation *in vitro* and effectively suppresses tumor growth *in vivo*, suggesting that this lysosomal ion channel represents a suitable target for cancer therapy. Mechanistically, we could show that TPC2 deficiency alters the metabolic phenotype, rendering a lower dependency on glycolysis, the main energy-yielding pathway of solid cancers. By combining chemical synthesis and state-of-the-art functional testing systems, we succeeded in generating novel, tetrandrine-derived TPC2 inhibitors that inhibit TPC2 currents with either equal (SG-005) or even higher potency (SG-094) than tetrandrine. Further, both new molecules display an enhanced potency to inhibit proliferation of several cancer cell lines and to impair phosphorylation of angiogenesis related VEGFR2 downstream targets in endothelial cells. Importantly, reduced toxicity of both simplified analogues to liver and blood cells was observed and, thus, one major disadvantage of tetrandrine has been overcome. Along this line, SG-094 was well-tolerated and successfully reduced tumor growth in a mouse model, thereby representing the first described TPC2 inhibitor with antitumor efficacy *in vivo*.

Additionally, the advanced candidates SG-005 and SG-094 also inhibited the drug efflux pump P-gp, a major cause of multidrug resistance, similarly to tetrandrine. Consequently, combination of vincristine with either tetrandrine, SG-005 or SG-094 successfully re-sensitized drug-resistant leukemia cells. Considering their favorable toxicity profile, SG-005 and SG-094 represent promising choices to modulate P-gp, for which no approved treatment options are available to date. The well described P-gp inhibitor elacridar, in turn, was identified as potent TPC2 blocker, revealing that TPC2 and P-gp have structural similarities. In addition to the fact that P-gp and TPC2 share mutual pharmacological inhibitors, we could also show that TPC2 deficiency sensitized drug-resistant leukemia cells towards vincristine, thus influencing chemoresistance.

Furthermore, we discovered P-gp as pharmacological target of the recently described isoquinoline-benzylisoquinoline alkaloid muraricine. Significantly increased apoptosis rates were observed in combination with vincristine while no acute cytotoxicity to healthy human cells (HUVEC) in concentrations higher than required for reversing chemoresistance was detected.

Lastly, SG-005 and SG-094 successfully sensitized sorafenib-resistant liver cancer cells to sorafenib in a P-gp-independent manner, providing the basis for studying the exact underlying mechanisms.

4.2 Part II: Phenothiazine-based benzhydroxamic acids as inhibitors of HDAC6

4.2.1 Functional characterization of the HDAC6 inhibitors KV-46, KV-70 and KV-181

HDAC6 represents a unique isoenzyme among HDACs as it is predominantly localized in the cytoplasm and therefore mainly deacetylates non-histone proteins such as α -tubulin⁵⁴ and the HSP90 chaperone⁵⁵. Defective regulation of HDAC6 activity is associated with a variety of human diseases and high expression seems to play a crucial role in the pathogenesis of cancer⁶⁰. By preparation and systemic variation of phenothiazines and their analogues containing a benzhydroxamic acid moiety as zinc-binding group (ZBG) (synthesis performed by Katharina Vögerl, Prof. Bracher, LMU Munich), we identified KV-46, KV-70 and KV-181 as potent HDAC6 inhibitors (**Figure 27**)¹¹⁷. In a biochemical *in vitro* assay (conducted by the group of Prof. Jung, University of Freiburg), their inhibitory activities against human HDAC1 and HDAC6 were evaluated. The lead structure KV-46 already showed very impressive HDAC6 inhibition ($IC_{50} = 22$ nM) and a selectivity factor (SF) of 231 over HDAC1, thus comparing favorably with the data obtained for tubastatin A ($IC_{50} = 30$ nM, SF = 64), a known selective HDAC6 inhibitor (**Figure 27**). The incorporation of one or two nitrogen atoms into the phenothiazine scaffold (KV-70, KV-181) even enhanced the potency for HDAC6. Strikingly, KV-70, bearing an 1-azaphenothiazine scaffold, attained a very high level of potency and selectivity ($IC_{50} = 5$ nM, SF = 538)¹¹⁷.

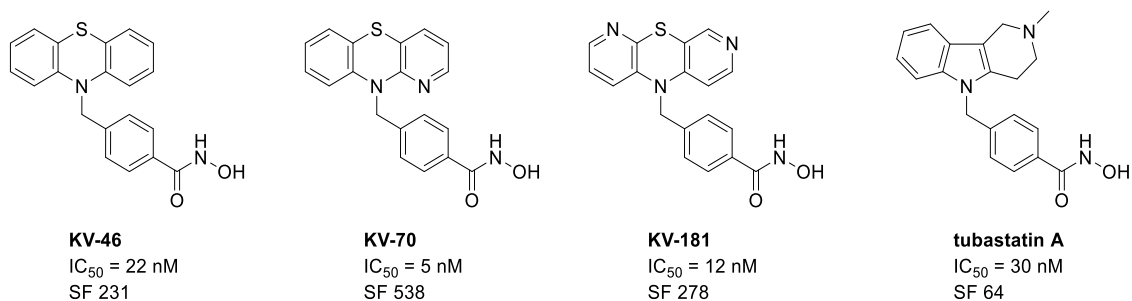


Figure 27 | Chemical structures of the novel HDAC6 inhibitors KV-46, KV-70 and KV-181 (synthesized by Katharina Vögerl, Prof. Bracher, LMU Munich) and the known HDAC6 inhibitor tubastatin A. The IC_{50} value indicates their inhibitory activity, as determined by *in vitro* testing on recombinant human HDAC6. The selectivity factor is a measure for their selectivity for HDAC6 over HDAC1. *In vitro* testing on HDAC6 and HDAC1 was performed by the group of Prof. Jung, University of Freiburg.

HDAC6 is a crucial regulator of gene expression and transcription in cancer and several HDAC6 inhibitors are currently investigated in clinical studies as potential tumor therapeutics⁵³. Likewise, we aimed to investigate the effects of KV-70 and KV-181 on different cancer cells. The lead structure KV-46 and the pan-HDAC inhibitor vorinostat were used as reference compounds. Firstly, cell viability assays indicated that KV46, KV-70 and KV-181 inhibited proliferation of HUH7 (hepatocellular carcinoma), MDA-MB-231 (breast adenocarcinoma) and T24 (bladder carcinoma) cells at concentrations of 10 and/or 100 μM after 72 h of incubation (**Figure 28 a**). Vorinostat treatment generally resulted in stronger antiproliferative effects, with IC_{50} values in the low micromolar range (HUH7: 1.2 μM , MDA-MB-231: 2.8 μM , T24: 2.4 μM). Secondly, cytotoxic effects on cancer cells were analyzed by measurement of apoptotic cell death. In accordance with antiproliferative effects, the highest apoptosis rates of all tested HDAC inhibitors were observed after treatment of MDA-MB-231 breast cancer and T24 bladder cancer cells with vorinostat for 48 h (**Figure 28 b**). These findings further emphasize that KV-46, KV-70 and KV-181 are selective HDAC6 inhibitors and their application as single treatment only causes minor anticancer activity, which is in line with the low clinical activity of selective HDAC6 inhibitors⁵³.

Furthermore, toxicity of the HDAC inhibitors to non-malignant cells was assessed using HepaRGTM cells. Toxicity and unfavorable tolerability associated with pan-HDAC inhibitor therapy¹¹⁸ remain key unmet needs that have driven the development of specific HDAC6 inhibitors. Viability of HepaRGTM cells after 24 h of treatment was not significantly reduced even at 100 μM concentrations of KV-46 and KV-70, whereas application of vorinostat and KV-181 slightly decreased cell viability at the highest tested concentration to around 80 % (**Figure 28 c**).

Results

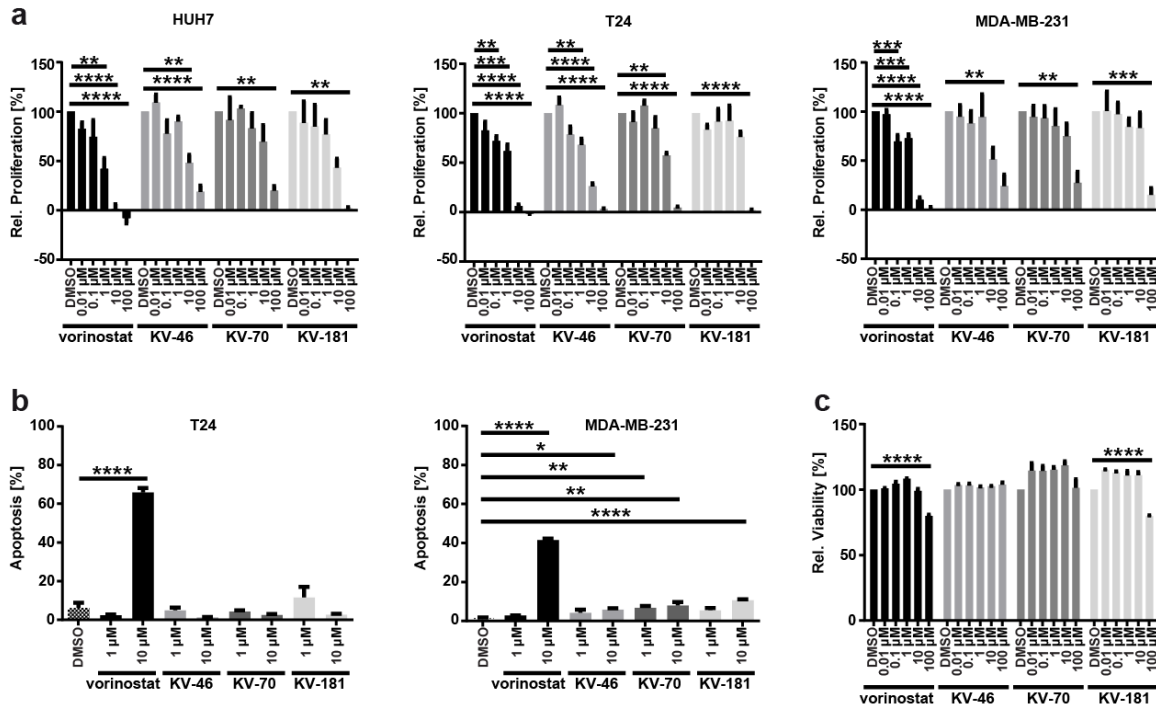


Figure 28 | Effects of HDAC6 inhibitors on proliferation and apoptosis of cancer cells and cell viability of non-cancerous liver cells. The pan HDAC-inhibitor vorinostat served as control. (a) Antiproliferative effects on HUH7, T24 and MDA-MB-231 cells were assessed by CellTiter-Blue® cell viability assay. Cells were treated with vorinostat, KV-46, KV-70 and KV-181 for 72 h. Proliferation is shown as percentage of vehicle control. **(b)** The percentage of apoptotic cells is shown. T24 and MDA-MB-231 cells were treated with the respective compounds (1 and 10 µM) 48 h. Apoptotic cells were quantified by propidium iodide staining and flow cytometry. **(c)** Toxicity was probed by treating HepaRG progenitor cells with vorinostat, KV-46, KV-70 and KV-181 for 24 h. Cell viability was assessed by CellTiter-Blue® cell viability assay and was normalized to vehicle control. **(a-c)** Bar graphs display means ± SEM experiments performed in triplicate (One-Way ANOVA followed by Tukey's multiple comparison test, * $P < 0.05$, ** $P < 0.01$, *** $P < 0.001$, **** $P < 0.0001$).

4.2.2 Influence of HDAC6 inhibition on immune checkpoints and unfolded protein response

The limited anticancer activity of specific HDAC6 inhibitors is sought to be overcome by combination strategies, e.g. with immunotherapeutic agents like lenalidomide¹¹⁹ or anti-programmed death receptor ligand-1 (PD-L1) antibodies¹²⁰ or, alternatively, with the proteasome inhibitor bortezomib^{121, 122}. Based on that, we hypothesized that KV-46, KV-70 and KV-181 might alter critical cancer-related pathways, namely immune checkpoints and unfolded protein response (UPR). Hence, we checked the influence of specific HDAC6 inhibition on PD-L1 and endoplasmatic reticulum chaperone BiP (GRP78). Interestingly, western blot analyses of bladder carcinoma lysates revealed that pharmacologic HDAC inhibition caused a clear upregulation of PD-L1 (**Figure 29 a**) and a slight increase in GRP78 protein level (**Figure 29 b**). Since a combination of HDAC6 inhibition and bortezomib is known to strongly enhance induction of GRP78 and

synergistically reduce cell viability¹²¹, we tested the influence of simultaneous exposure of KV-46, KV-70 and KV-181 and bortezomib on cell proliferation by impedance measurements. However, we could not prove a synergism of KV-46, KV-70 and KV-181 and bortezomib at the tested concentrations (**Figure 29 c**), which we related to the narrow therapeutic window of bortezomib in our setting (**Figure 29 d**). Taken together, KV-46, KV-70 and KV-181 alter protein levels of PD-L1 and GRP78, providing the rationale for their future investigation in combination therapies. This piece of work was published in the Journal of Medicinal Chemistry (American Chemical Society) in 2019¹¹⁷.

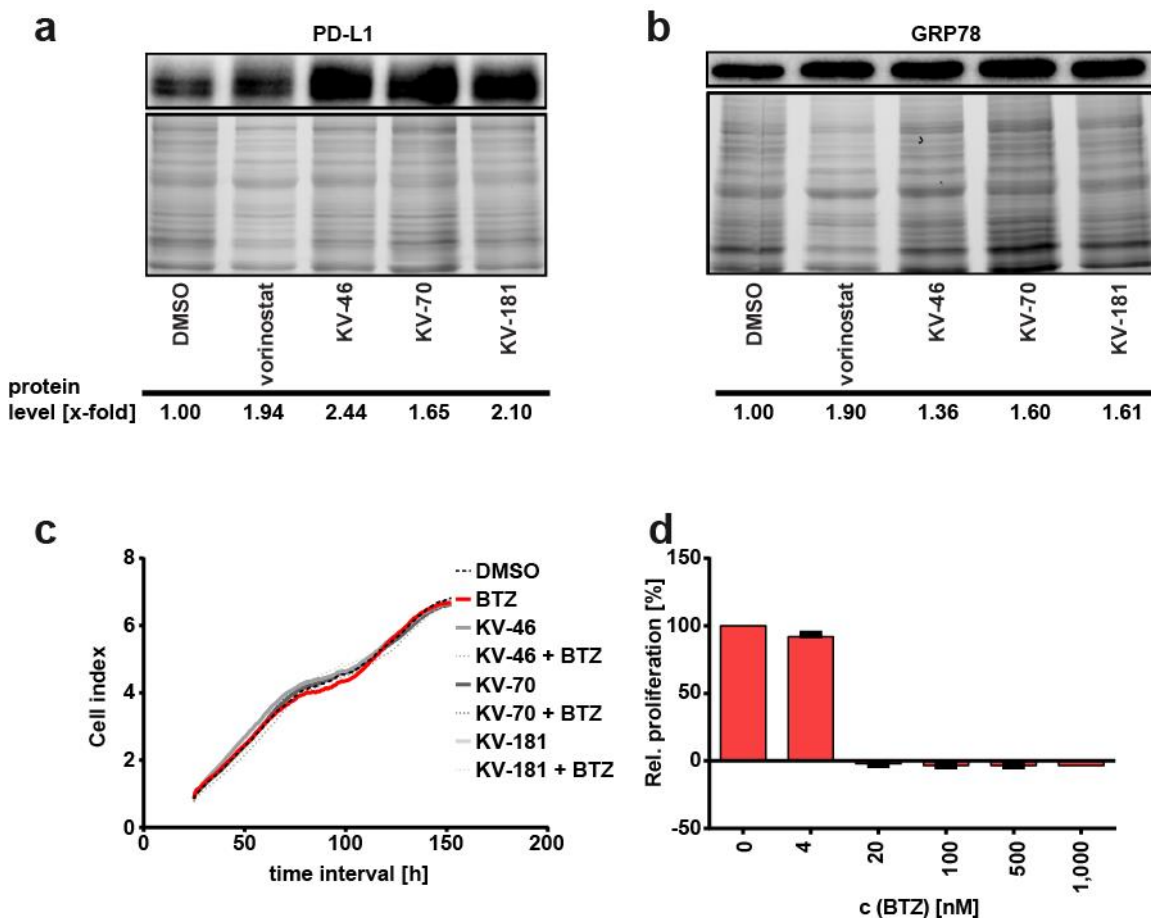


Figure 29 | Alteration of expression of immune checkpoint and unfolded protein response protein markers upon HDAC6 inhibition provide the rationale for combination regimens. (a,b) Influence of vorinostat, KV-46, KV-70 and KV-181 treatment (48 h) on protein expression of (a) programmed death receptor ligand-1 (PD-L1) and (b) endoplasmic reticulum chaperone BiP (GRP78) in T24 cells. (c) No synergism of KV-46, KV-70 and KV-181 (1 μ M) with bortezomib (BTZ) could be found by analysing proliferation of T24 cells with impedance measurements. (d) A CellTiter-Blue[®] cell viability assay shows the narrow therapeutic window of bortezomib after 72 h of treatment. (c) Graph displays mean and (d) bar graph displays means \pm SEM of experiments performed in triplicate.

4.2.3 Part II: Summary

With the second part of this project, inhibitors of another cancer-relevant target, HDAC6, were investigated. Together with collaborators, the group of Prof. Bracher developed HDAC6-specific inhibitors, currently a hot topic in clinical trials, namely the phenothiazine-based benzhydroxamic acids KV-46, KV-70 and KV-181. Biological characterization revealed that all three molecules were relatively non-toxic to non-malignant, hepatocyte-like cells, they moderately inhibited proliferation of different cancer cell lines and barely caused apoptosis. In contrast, the pan-HDAC inhibitor vorinostat impaired proliferation and induced apoptosis to a greater extent. These observations are in line with the low clinical efficacy of specific HDAC6 vs. pan-HDAC inhibition, providing the rationale for combination regimens. In that respect, we detected an upregulation of protein markers of the unfolded protein response and immune checkpoints, namely GRP78 and PD-L1, upon exposure of bladder cancer cells to KV-46, KV-70 and KV-181.

DISCUSSION



5 Discussion

5.1 Discussion part I

5.1.1 Validation of two-pore channel 2 as target for cancer therapy and development of synthetically accessible inhibitors

Inevitably, the identification of novel, druggable targets represents a key step for the improvement of tumor therapy. Analysis of differentially expressed gene signatures revealed that high gene expression of *TPCN2* acts as negative predictive value for post-operative biochemical recurrence in prostate cancer patients after radical prostatectomy⁸. Moreover, TPC2 was shown to be involved in neoangiogenesis^{13, 15} as well as migration and metastasis formation¹², providing incentive for further investigation of its role in cancer. Our findings clearly illustrate that TPC2 is a cancer driver as genetic ablation of the channel reduced proliferation of liver cancer cells *in vitro* and effectively halted tumor growth in an ectopic mouse model. This, in turn, highlights the need for the development of suitable TPC2 inhibitors as potential anticancer drugs. Apart from induction of blood vessel formation and activation of invasion and metastasis, chronic proliferation doubtlessly represents a key hallmark capability that enables tumor growth¹⁴.

In addition to the frequent dysregulation of cellular proliferation, cancer cells often reprogram their energy metabolism in order to fuel extensive cell division¹⁴. We unraveled that TPC2 influences glucose utilization of liver cancer cells for energy production. Mechanistically, TPC2 knockout led to reduced phosphorylation of HK II, a key mediator of glycolytic flux, which can be regulated transcriptionally⁸² or by posttranslational modification^{104, 106}. Thus, our work expands the number of cancer hallmarks¹⁴ that are affected by TPC2. Normal cells convert glucose to pyruvate in the cytosol by glycolysis, then further oxidize it to carbon dioxide in mitochondria. Many cancer cells, however, preferentially use glycolysis for ATP production, despite the presence of oxygen, a phenomenon that is termed aerobic glycolysis or Warburg effect⁸². Upon loss of TPC2 function or pharmacological inhibition of this channel, extracellular flux analyses and FRET-based live cell monitoring indicated a switch towards lower glycolysis and, hence, metabolic reprogramming of liver cancer cells was partly reversed. Although glycolysis produces substantially less ATP per mol glucose than mitochondrial oxidative phosphorylation¹⁴, it is hypothesized that it represents a distinct growth advantage and seems to be linked to tumor aggressiveness⁸². On the one hand, constantly upregulated glycolysis provides faster ATP production and metabolic intermediates for biosynthesis of

macromolecules required for rapid proliferation and it enables the adaption to hypoxic conditions that frequently occur in tumor regions. On the other hand, elevated export of the glycolytic waste products lactic acid and hydroxonium ions into the extracellular space can facilitate invasion through acidification of the tumor microenvironment⁸². Several preclinical and early phase clinical studies showed efficacy of disrupting glycolytic energy metabolism of cancer cells. However, direct inhibition of the glycolytic pathway can cause severe toxicity¹²³. By targeting TPC2, we present an alternative approach to indirectly interfere with aerobic glycolysis.

Importantly, we have underlined that TPC2 is a druggable target as novel small molecule blockers, SG-005 and SG-094, with antiproliferative activity have been developed in the course of this investigation. Taking into consideration that TPC2 KO mice are viable^{13, 48, 81, 107}, our study suggests that pharmacological interference with TPC2 function is sufficient to induce antitumor effects while it can generally be tolerated by mammalian organisms. Besides, preferential uptake of the blockers into cancer cells could contribute to the observed tumor selectivity.

Further, the tetrandrine congeners are superior to other known TPC2 inhibitors, naringenin and Ned-19, concerning the impairment of proangiogenic signaling and inhibition of cancer cell proliferation. Naringenin and Ned-19 were mechanistically studied by others with respect to the involvement of TPC2 in VEGF-induced angiogenesis, which is necessary for vascularization of solid tumors^{13, 15}. In detail, knockdown of TPC2 using shRNA abolished capillary-like tube formation of HUVECs *in vitro* and vessel formation was abrogated in TPC2 KO, but not in TPC1 KO mice, suggesting an isoform-specific role for TPC2¹³. This effect was mimicked by treatment with Ned-19 and, mechanistically, it reduced Ca²⁺-evoked phosphorylation of eNOS, JNK, MAPK and AKT, although high micromolar doses (100 μ M) were required¹³. Similarly, 500 μ M of naringenin were applied to prevent VEGF-induced vessel formation¹⁵. Of note, we could show that 1 h of pre-treatment with a far lower concentration of SG-005 and SG-094 (10 μ M each) was sufficient to impair phosphorylation of VEGFR2 downstream targets, whereas tetrandrine did not show an effect. Thus, an improved on-target effect of truncated tetrandrine analogues SG-005 and SG-094 was found in intact whole cells, which we partly linked to enforced accumulation in lysosomes.

Additionally, we tested the tetrandrine congeners as well as known TPC2 inhibitors for their antiproliferative activities on cancer cells. In line with the reported requirement of high concentrations (at \geq 50 μ M) for the impairment of VEGF-induced vessel formation, as well

as migration¹² and proliferation of tumor cells^{124, 125}, Ned-19 and naringenin displayed weak antiproliferative effects on RIL175 cells, starting at high micromolar concentrations (at $\geq 75 \mu\text{M}$). Instead, we chose tetrandrine as lead molecule as it could successfully inhibit migration of invasive cancer cells (at $\leq 15 \mu\text{M}$)¹² and reduce Ebola virus infection of HeLa cells (at $\leq 2 \mu\text{M}$)²⁴ *via* TPC inhibition at low micromolar concentrations. Though tetrandrine also considerably inhibited proliferation of RIL175 cells (IC_{50} : $9.1 \mu\text{M}$), antiproliferative effects were markedly enhanced for SG-005 and SG-094 (IC_{50} : 2.4 and $3.7 \mu\text{M}$).

Moreover, tetrandrine has serious deficiencies, which include its rather moderate inhibition of TPC2 (54 % at $10 \mu\text{M}$ in our setting), its structural complexity and its pulmonary and hepatic toxicity^{27, 28, 91, 92, 93}. To cope with these limitations, we have synthesized and screened various analogues (other bisbenzylisoquinoline alkaloids and synthetic derivatives thereof, truncated analogues, mainly substituted 1-BTHIQs) of the lead molecule by cell proliferation assays, calcium imaging and endolysosomal patch clamp. Apart from enabling chemical accessibility, structural simplification was proven to be an effective strategy to overcome drawbacks of natural compounds, with respect to drug-likeness and potency¹²⁶. Exemplarily, structurally simpler analogues of trabectedin¹²⁷ and gambogic acid¹²⁸ led to equal or stronger antitumor activity, depending on the cell line, while the mode of action remained the same. Here, we demonstrate that the rigid, macrocyclic BBTHIQ structure of tetrandrine can be reduced to less complex BTHIQ scaffold, in case additional aromatic residues (no less than two aryl or benzyl ethers) are introduced. These crucial additional aromatic residues most likely mimic the two benzenoid rings of the second benzylisoquinoline moiety of the parent compound tetrandrine and their flexibility should enable them to adapt to the binding site of the target protein. In comparison to the very complex synthetic routes to tetrandrine^{29, 30}, SG-005 and SG-094 are accessible *via* a short and inexpensive synthesis. Moreover, simplification resulted in similar (SG-005: 44 % at $10 \mu\text{M}$) or even enhanced inhibition (SG-094: 75 % at $10 \mu\text{M}$) of PI(3,5)-P₂-evoked TPC2 currents and, as stated before, to comparable or stronger antiproliferative properties against several cancer cell lines. This even applied to leukemic cells which display a multidrug resistant phenotype (VCR-R CEM)⁷⁰. Concurrently, toxicity to non-cancerous liver cells and PBMCs was markedly reduced for SG-094 and slightly reduced for SG-005. Since SG-005 was more toxic to PBMCs than SG-094, a lower dose was applied in the ectopic mouse model, but this dose was not sufficient to translate the antiproliferative *in vitro* potency into *in vivo* efficacy. Nevertheless, due to the enhanced on-target effect on TPC2 and the improved toxicity profile *versus* tetrandrine, as outlined above, SG-005 might have the potential to treat

other conditions that are connected to TPC2, such as cardiac dysfunction and viral infections^{7, 25, 26}. The other optimized tetrandrine congener, SG-094, successfully managed to reduce tumor growth *in vivo* at tolerated doses and thereby represents a promising drug candidate for cancer therapy.

Taken together, we could show that interfering with TPC2 function reduces cancer cell proliferation, alters cellular energy metabolism and prevents tumor growth. Additionally, we have added easily accessible, potent inhibitors with favorable drug-likeness to the limited panel of currently available direct TPC2 blockers.

5.1.2 Tetrandrine toxicity is independent of cellular CYP3A4 expression

Tetrandrine has diverse pharmacological activities¹¹¹, but, as outlined above, its clinical application is limited by its toxicity^{27, 28, 91, 92, 94}. Five diastereomeric pairs of novel analogues of tetrandrine and its natural diastereomer isotetrandrine, respectively, were synthesized and biologically evaluated with respect to their toxicity in the course of this investigation. The design of these new analogues was driven by the published hypothesis that one particular structural element, the methoxy group at C-12 in *para*-position to a benzylic methylene group, is responsible for toxicity due to its susceptibility to undergo enzymatic oxidation to a reactive (toxic) *para*-quinone methide, which in turn can react with bio-nucleophiles²⁷. The shape of the new compounds was intended to prevent this oxidative toxification process. Although all the analogues lack the putative problematic structure motif, no significant decrease of toxicity could be observed without a concurrent reduction of anticancer activity. Compounds RMS2, RMS4 and RMS8 were found to be even more toxic to healthy cells than tetrandrine. Moreover, CYP3A4 overexpression in two cellular models that are established for recombinant hepatotoxicity studies suggested that the propagated mechanism of CYP3A4-mediated toxification involving the *para*-quinone methide is no primary cause for the cytotoxicity of tetrandrine and related (bis)benzylisoquinoline alkaloids.

To decipher the correlation between the structure of quinone methides and their liver toxicity, Thompson and coworkers¹²⁹ investigated the toxicity of a series of 4-alkyl-2-methoxyphenols using an *in vitro* hepatotoxicity model. Although all tested molecules were converted into quinone methides, only little correlation between the rate of quinone methide formation in microsomes and relative toxicities of the alkylphenols was found¹²⁹. It was suggested that primarily the reactivity of the quinone methides being formed and their stability towards solvolysis are the determining factors for their toxicity. These findings

support the results of a former *in vivo* study¹³⁰ which observed differences in the toxicities of 2-methoxy-quinone methides that could be explained by their relative reactivities¹³¹. Thus, formation of quinone methides does not necessarily lead to toxicity *in vitro* and *in vivo*.

Not only the comparison of tetrandrine with the analogues RMS1-RMS10 that lack the putative problematic structure motif, but also our study performed with the isoquinoline-benzylisoquinoline muraricine suggest that enzymatic oxidation to a *para*-quinone methide is not the primary cause for *in vitro* toxicity. Tetrandrine strongly and dose-dependently reduced cell viability of HUVECs within a 6 h treatment period, whereas muraricine did not show an effect. Muraricine contains a *para*-hydroxybenzyl moiety and could theoretically be oxidized to a (toxic) *para*-quinone methide by CYP3A4 without the need for previous O-demethylation. Since HUVECs express various CYP enzymes, including CYP3A¹³², but no cytotoxic effect even at micromolar high doses of muraricine (50 μ M) was observed, this finding further contradicts the hypothesis of CYP3A4-mediated toxification of tetrandrine and related alkaloids.

For tetrandrine, other proposed mechanisms might play a more substantial role in toxicity, such as the generation of ROS by CYP2E1⁹² or the proposed interaction with p38 α MAPK, a promotor of inflammatory processes in the liver⁹¹, or additional effects that remain to be elucidated.

5.1.3 TPC2, tetrahydroisoquinolines and chemoresistance

As outlined in chapter 5.1.1, the simplified tetrandrine congeners SG-005 and SG-094 are superior to their parental molecule regarding inhibitory on-target effects on TPC2 in a cellular setting and the toxicity profile. Additionally, we could show that SG-005 and SG-094 inhibit the efflux transporter P-gp and thus successfully reversed chemoresistance of VCR-R CEM cells to vincristine. P-gp facilitates the efflux of cytostatic drugs and thereby represents a major cause of treatment failure and resistance to common cancer therapeutics³⁷. As no clinically approved treatment options are available so far, there is a high unmet need for identifying novel safe and efficacious P-gp inhibitors. Inhibition of P-gp is mostly described for macrocyclic bisbenzylisoquinolines like tetrandrine, which even advanced into early phase clinical trials^{34, 35}, and related alkaloids³⁷, but also for some *seco*-analogues, such as sanguinarine¹³³ and chelidonine¹³⁴. Considering their reduced toxicity to non-malignant hepatocytes and PBMCs, in comparison to tetrandrine, the *seco*-analogues SG-005 and SG-094 might represent novel safe and effective options to

reverse multidrug resistance in cancer. Furthermore, since tetrandrine, SG-005 and SG-094 inhibit both TPC2 and P-gp, structural similarities between the binding pockets on both proteins must be present. The three-dimensional structure of P-gp has been resolved and numerous, structurally diverse inhibitors are known^{37, 38}, which could aid to identify new lead structures for TPC2 blockers.

In contrast to tetrandrine, SG-005 and SG-094, muraricine was not capable of blocking TPC2 currents in Ca²⁺ imaging experiments nor had significant antiproliferative or cytotoxic effects on cancer or endothelial cells. Muraricine lacks a second aryl or benzyl ether being essential for TPC2 inhibition, which is in line with the conclusions drawn from the screening of simplified tetrandrine congeners. Aside from moderate butylcholinesterase inhibition that was found upon initial investigations¹¹⁵, no pharmacological activities of muraricine were known. We could show that muraricine moderately inhibits P-gp and sensitizes drug-resistant leukemia cells to vincristine at a concentration that can be tolerated by non-malignant cells, albeit significantly higher concentrations (25 µM) were necessary than for tetrandrine, SG-005 and SG-094 (1 µM). Based on our synthetic approach, systematic structure variations of muraricine can be part of future drug design projects, as there is a high clinical need for P-gp inhibitors for the treatment of chemoresistant tumors.

The other way around, we tested elacridar, representative for third-generation P-gp inhibitors, for its ability to block TPC2. Indeed, patch clamp experiments revealed that it reduced TPC2 currents to a stronger extent than tetrandrine, challenging the widely accepted view on elacridar specifically acting on efflux pumps³⁹. Although elacridar bears a tetrahydroisoquinoline moiety, the acridone substituent and the lack of the 1-benzyl or 1-phenyl substituent substantially differentiate it from tetrandrine and analogues thereof. Consequently, elacridar might also represent a new lead structure for further optimization of TPC2 inhibitors. Thinking one step ahead, this further provides the basis for investigating other third-generation inhibitors, such as tariquidar, laniquidar and zosuquidar, which could potentially be repurposed as TPC2 inhibitors for tumor therapy and beyond. The molecules of this class have a known and favorable safety profile, when applied as monotherapy, which could simplify translatability into clinical practice. For instance, toxicity of three doses of zosuquidar 500 mg peroral (p.o.) was minimal¹³⁵ and adverse events of elacridar 400 mg p.o. twice daily were limited to occasional somnolence and gastrointestinal complaints⁴¹. However, when compared to SG-005 and SG-094, far

higher concentrations of elacridar were necessary to achieve direct anticancer effects. Hence, it remains to be determined if such plasma levels can be achieved with elacridar.

Interestingly, TPC2 and P-gp or, more generally, chemoresistance, not only share common small molecule modulators, they also seem to be functionally connected. We found that TPC2 mRNA levels were elevated in P-gp overexpressing VCR-R CEM cells in comparison to their non-resistant, parental counterpart and that TPC2 KO slightly sensitized VCR-R CEM cells to VCR, suggesting that TPC2 affects chemoresistance. Since recent works of others^{45, 46} pointed out that P-gp is not only localized to the plasma membrane, but can also be relocated to the lysosome to tremendously enhance lysosomal sequestration of chemotherapeutics, it will be of great relevance to study if TPC2 affects cellular localization of P-gp and thereby sensitizes resistant cells to cytostatic agents. Targeting of lysosomal proteins, such as the V-ATPase and the acid sphingomyelinase, was proven to be a successful strategy to overcome multidrug resistance. Specifically, V-ATPase knockdown sensitized doxorubicin-resistant MCF-7 cells to doxorubicin and vincristine⁴⁹. Targeting acid sphingomyelinase, a lipase responsible for lysosomal hydrolysis of sphingomyelin, was proven to be another effective strategy to successfully treat multidrug resistant tumors, by disrupting lysosomal membrane integrity and thereby achieving cancer-specific cytotoxicity⁵⁰.

Additionally, the TPC2 blockers tetrandrine, SG-005 and SG-094, significantly enhanced the response of sorafenib-resistant liver tumor cells to sorafenib. The broad cross-resistance of those HUH7-R cells was previously found to be independent of the multidrug resistance machinery. Instead, a shift towards a higher glycolytic phenotype, elevated cytosolic Ca²⁺ levels and increased lysosomal volume were observed, among others, when compared to the sensitive WT counterpart¹¹⁴. Since these characteristics can potentially be influenced by modulating TPC2 function, we tested the ability of tetrandrine and its congeners SG-005 and SG-094 to provide a therapeutic benefit. As this was the case, it remains to be clarified by using genetic knockdown/knockout models if blocking TPC2 is the main reason for the sensitization or if e.g. the basicity and potentially related lysosomotropic effects play a more important role.

Taken together, novel *seco*-analogues of tetrandrine, SG-005, SG-094 and muraricine were found to be either chemosensitizers and/or inhibitors of P-gp, thus aiding the search for effective multidrug resistance modulators. Further, first hints for TPC2 being a contributor to drug resistance were provided and a dual mode of action of TPC2 and P-gp antagonists was established.

5.2 Discussion part II

In contrast to most other HDACs, HDAC6 is primarily located in the cytoplasm and also deacetylates various non-histone substrates, such as cortactin⁵⁶ and α -tubulin⁶². Thereby, it is involved in cellular processes, including proliferation and motility⁵⁷, and it has gained great interest as target in tumor therapy⁵³. By developing the HDAC6 inhibitors KV-46, KV-70 and KV-181 with superior potency and specificity compared with the known HDAC6 inhibitor tubastatin A, we have addressed the high need for the identification of HDAC6-specific inhibitors⁵³. By variation of the phenothiazine-based capping motif, KV-70 could be developed as the most potent (IC₅₀: 5 nM) and isoenzyme-specific (SF of 538 over HDAC1) HDAC6 inhibitor of our study. As expected, antiproliferative effects of KV-46, KV-70 and KV-181 on several cancer cell lines were lower in comparison to those of the pan-HDAC inhibitor vorinostat. Likewise, induction of apoptosis was strongly reduced, which is in line with a study conducted by Woan *et al.*¹³⁶, who observed decreased proliferation without induction of apoptosis upon HDAC6 knockdown in melanoma cells. Further, viability of non-cancerous HepaRGTM cells was hardly or not at all impaired upon exposure to KV-46, KV-70 and KV-181, indicating low toxicity of the compounds. Undesired toxicity of pan-HDAC inhibition caused by indiscriminate modulation of various HDAC isoenzymes limits its clinical use and, thus, the usage of more selective HDAC inhibitors is sought to improve patient prognosis to a greater extent⁵³.

The limited efficacy of specific HDAC6 inhibition alone in both preclinical and clinical setting has driven studies on combination regimens, mainly with proteasome inhibitors^{66, 68, 121, 122} and immunomodulatory agents^{136, 137, 138}. Interestingly, we found that HDAC6 inhibition by KV-46, KV-70 and KV-181, as well as pan-HDAC modulation by vorinostat, increased protein expression of GRP78, a marker for the activation of the unfolded protein response (UPR). The UPR is responsible for detection of misfolded proteins and the control of their disposal. Misfolded proteins can either be eliminated via the proteasome or the aggresome. Simultaneous blockade of the two main garbage-disposal systems, namely the proteasome by proteasome inhibitors and the aggresome by HDAC inhibitors, can synergistically increase cytotoxicity¹³⁹. In this context, Amengual *et al.*¹²¹ detected increased GRP78 expression following treatment of lymphoma cells with ricolinostat, an effect that was enhanced by the proteasome inhibitor bortezomib. Later, Li and coworkers¹⁴⁰ detected elevated GRP78 protein levels after exposure of colon cancer cells to tubastatin A. Although we could not show a synergistic effect with bortezomib due to its narrow therapeutic window, our results further extend the knowledge about the impact on

HDAC6 inhibition on UPR and proposes KV46, KV70 and KV-181 as candidates for combination studies with proteasome inhibitors.

Moreover, our data could help to decipher the interaction of HDAC6 and PD-L1 in cancer, which is still debated. In our study, both pan-HDAC (vorinostat) and HDAC6 inhibition (KV-46, KV-70, KV-181) increased PD-L1 protein levels in T24 bladder cancer cells. Woods *et al.*¹⁴¹ could show that class I and pan-HDAC inhibition (panobinostat, entinostat, MGCD0103) enhances antitumor immunity by upregulating PD-L1 expression in a panel of melanoma cell lines *in vitro* and *in vivo*, Lienlaf and coworkers¹³⁷, on the other hand, found a reduction of PD-L1 protein level after HDAC6 inhibition (tubastatin A and nexturastat A) in melanoma cells. They reported that HDAC6 is essential for cytokine-mediated expression control of PD-L1. Yet, Woan *et al.*¹³⁶ could not detect alterations in PD-L1 protein level after pharmacologic (tubastatin A and nexturastat A) or shRNA knockdown of HDAC6 activity in both human and murine melanoma cell lines. It is therefore obvious that more research has to be performed to clarify the role of HDAC6 in PD-L1 regulation. Although several HDAC6-selective inhibitors are available, inhibition of other HDACs can lead to opposing effects, depending on the concentration of the inhibitor and incubation times. Unfortunately, studies on stable HDAC6 knockout cells and the influence on PD-L1 expression are lacking to date. Adding still more complexity to the question, the regulation might also be tissue specific as tumors of different origin display distinct immunogenicity¹⁴². Therefore, HDAC6 inhibition can cause an upregulation of PD-L1 in bladder cancer, as reported in our study, and at the same time an unchanged expression or a downregulation in melanoma as reported by Woan *et al.*¹³⁶ and by Lienlaf *et al.*¹³⁷, respectively.

Taken together, the novel potent and selective HDAC6 inhibitors KV-46, KV-70 and KV-181 were developed and our findings confirm the rationale for combining them with anti-PD1/anti-PD-L1 antibodies and proteasome inhibitors.

REFERENCES



6 References

1. Bray, F. *et al.* Global cancer statistics 2018: GLOBOCAN estimates of incidence and mortality worldwide for 36 cancers in 185 countries. *CA Cancer J Clin* **68**, 394-424 (2018).
2. Santos, R. *et al.* A comprehensive map of molecular drug targets. *Nat Rev Drug Discov* **16**, 19-34 (2017).
3. Workman, P. & Al-Lazikani, B. Drugging cancer genomes. *Nat Rev Drug Discov* **12**, 889-890 (2013).
4. Patel, S. Two-pore channels open up. *Nature* **556**, 38-40 (2018).
5. She, J. *et al.* Structural insights into the voltage and phospholipid activation of the mammalian TPC1 channel. *Nature* **556**, 130-134 (2018).
6. Gerndt, S. *et al.* Agonist-mediated switching of ion selectivity in TPC2 differentially promotes lysosomal function. *Elife* **9** (2020).
7. Patel, S. & Kilpatrick, B.S. Two-pore channels and disease. *Biochim Biophys Acta Mol Cell Res* **1865**, 1678-1686 (2018).
8. Li, F., Ji, J.P., Xu, Y. & Liu, R.L. Identification a novel set of 6 differential expressed genes in prostate cancer that can potentially predict biochemical recurrence after curative surgery. *Clin Transl Oncol* (2019).
9. Grimm, C., Bartel, K., Vollmar, A.M. & Biel, M. Endolysosomal Cation Channels and Cancer-A Link with Great Potential. *Pharmaceuticals (Basel)* **11** (2018).
10. Faris, P., Shekha, M., Montagna, D., Guerra, G. & Moccia, F. Endolysosomal Ca(2+) Signalling and Cancer Hallmarks: Two-Pore Channels on the Move, TRPML1 Lags Behind! *Cancers (Basel)* **11** (2018).
11. Ruas, M. *et al.* Purified TPC isoforms form NAADP receptors with distinct roles for Ca(2+) signaling and endolysosomal trafficking. *Curr Biol* **20**, 703-709 (2010).
12. Nguyen, O.N. *et al.* Two-Pore Channel Function Is Crucial for the Migration of Invasive Cancer Cells. *Cancer Res* **77**, 1427-1438 (2017).
13. Favia, A. *et al.* VEGF-induced neoangiogenesis is mediated by NAADP and two-pore channel-2-dependent Ca²⁺ signaling. *Proc Natl Acad Sci U S A* **111**, E4706-4715 (2014).
14. Hanahan, D. & Weinberg, R.A. Hallmarks of cancer: the next generation. *Cell* **144**, 646-674 (2011).

-
15. Pafumi, I. *et al.* Naringenin Impairs Two-Pore Channel 2 Activity And Inhibits VEGF-Induced Angiogenesis. *Sci Rep* **7**, 5121 (2017).
 16. Fuhr, U., Klittich, K. & Staib, A.H. Inhibitory effect of grapefruit juice and its bitter principal, naringenin, on CYP1A2 dependent metabolism of caffeine in man. *Br J Clin Pharmacol* **35**, 431-436 (1993).
 17. Guengerich, F.P. & Kim, D.H. In vitro inhibition of dihydropyridine oxidation and aflatoxin B1 activation in human liver microsomes by naringenin and other flavonoids. *Carcinogenesis* **11**, 2275-2279 (1990).
 18. Ho, P.C., Saville, D.J. & Wanwimolruk, S. Inhibition of human CYP3A4 activity by grapefruit flavonoids, furanocoumarins and related compounds. *J Pharm Pharm Sci* **4**, 217-227 (2001).
 19. Scholz, E.P. *et al.* Inhibition of cardiac HERG channels by grapefruit flavonoid naringenin: implications for the influence of dietary compounds on cardiac repolarisation. *Naunyn Schmiedebergs Arch Pharmacol* **371**, 516-525 (2005).
 20. Zitron, E. *et al.* QTc prolongation by grapefruit juice and its potential pharmacological basis: HERG channel blockade by flavonoids. *Circulation* **111**, 835-838 (2005).
 21. Penny, C.J. *et al.* Mining of Ebola virus entry inhibitors identifies approved drugs as two-pore channel pore blockers. *Biochim Biophys Acta Mol Cell Res* **1866**, 1151-1161 (2019).
 22. Divac, N., Prostran, M., Jakovcevski, I. & Cerovac, N. Second-generation antipsychotics and extrapyramidal adverse effects. *Biomed Res Int* **2014**, 656370 (2014).
 23. Rossi, L.M.M. *et al.* Factors related with osteoporosis treatment in postmenopausal women. *Medicine (Baltimore)* **97**, e11524 (2018).
 24. Sakurai, Y. *et al.* Ebola virus. Two-pore channels control Ebola virus host cell entry and are drug targets for disease treatment. *Science* **347**, 995-998 (2015).
 25. Gunaratne, G.S., Yang, Y., Li, F., Walseth, T.F. & Marchant, J.S. NAADP-dependent Ca(2+) signaling regulates Middle East respiratory syndrome-coronavirus pseudovirus translocation through the endolysosomal system. *Cell Calcium* **75**, 30-41 (2018).
 26. Ou, X. *et al.* Characterization of spike glycoprotein of SARS-CoV-2 on virus entry and its immune cross-reactivity with SARS-CoV. *Nat Commun* **11**, 1620 (2020).

-
27. Jin, H. *et al.* Pulmonary toxicity and metabolic activation of tetrandrine in CD-1 mice. *Chem Res Toxicol* **24**, 2142-2152 (2011).
 28. Tainlin, L., Tingyi, H., Changqi, Z., Peipei, Y. & Qiong, Z. Studies of the chronic toxicity of tetrandrine in dogs: an inhibitor of silicosis. *Ecotoxicol Environ Saf* **6**, 528-534 (1982).
 29. Inubushi, Y., Masaki, Y., Matsumoto, S. & Takami, F. Total syntheses of optically active natural isotetrandrine, phaeanthine and tetrandrine. *Tetrahedron Lett*, 3399-3402 (1968).
 30. Schütz, R., Meixner, M., Antes, I. & Bracher, F. A modular approach to the bisbenzylisoquinoline alkaloids tetrandrine and isotetrandrine. *Org Biomol Chem* (2020).
 31. Wang, G., Lemos, J.R. & Iadecola, C. Herbal alkaloid tetrandrine: from an ion channel blocker to inhibitor of tumor proliferation. *Trends Pharmacol Sci* **25**, 120-123 (2004).
 32. Bellik, Y. *et al.* Molecular mechanism underlying anti-inflammatory and anti-allergic activities of phytochemicals: an update. *Molecules* **18**, 322-353 (2012).
 33. Liao, D. *et al.* Tetrandrine Interaction with ABCB1 Reverses Multidrug Resistance in Cancer Cells Through Competition with Anti-Cancer Drugs Followed by Downregulation of ABCB1 Expression. *Molecules* **24** (2019).
 34. Robey, R.W. *et al.* Inhibition of P-glycoprotein (ABCB1)- and multidrug resistance-associated protein 1 (ABCC1)-mediated transport by the orally administered inhibitor, CBT-1[®]. *Biochem Pharmacol* **75**, 1302-1312 (2008).
 35. Kelly, R.J. *et al.* A pharmacodynamic study of the P-glycoprotein antagonist CBT-1[®] in combination with paclitaxel in solid tumors. *Oncologist* **17**, 512 (2012).
 36. <https://clinicaltrials.gov/>, last accessed on 06-18-2020.
 37. Joshi, P., Vishwakarma, R.A. & Bharate, S.B. Natural alkaloids as P-gp inhibitors for multidrug resistance reversal in cancer. *Eur J Med Chem* **138**, 273-292 (2017).
 38. Dewanjee, S. *et al.* Natural Products as Alternative Choices for P-Glycoprotein (P-gp) Inhibition. *Molecules* **22** (2017).
 39. Dash, R.P., Jayachandra Babu, R. & Srinivas, N.R. Therapeutic Potential and Utility of Elacridar with Respect to P-glycoprotein Inhibition: An Insight

-
- from the Published In Vitro, Preclinical and Clinical Studies. *Eur J Drug Metab Pharmacokinet* **42**, 915-933 (2017).
40. Varma, M.V., Ashokraj, Y., Dey, C.S. & Panchagnula, R. P-glycoprotein inhibitors and their screening: a perspective from bioavailability enhancement. *Pharmacol Res* **48**, 347-359 (2003).
 41. Planting, A.S. *et al.* A phase I and pharmacologic study of the MDR converter GF120918 in combination with doxorubicin in patients with advanced solid tumors. *Cancer Chemother Pharmacol* **55**, 91-99 (2005).
 42. Kuppens, I.E. *et al.* A phase I, randomized, open-label, parallel-cohort, dose-finding study of elacridar (GF120918) and oral topotecan in cancer patients. *Clin Cancer Res* **13**, 3276-3285 (2007).
 43. Cripe, L.D. *et al.* Zosuquidar, a novel modulator of P-glycoprotein, does not improve the outcome of older patients with newly diagnosed acute myeloid leukemia: a randomized, placebo-controlled trial of the Eastern Cooperative Oncology Group 3999. *Blood* **116**, 4077-4085 (2010).
 44. Pusztai, L. *et al.* Phase II study of tariquidar, a selective P-glycoprotein inhibitor, in patients with chemotherapy-resistant, advanced breast carcinoma. *Cancer* **104**, 682-691 (2005).
 45. Yamagishi, T. *et al.* P-glycoprotein mediates drug resistance via a novel mechanism involving lysosomal sequestration. *J Biol Chem* **288**, 31761-31771 (2013).
 46. Al-Akra, L. *et al.* Tumor stressors induce two mechanisms of intracellular P-glycoprotein-mediated resistance that are overcome by lysosomal-targeted thiosemicarbazones. *J Biol Chem* **293**, 3562-3587 (2018).
 47. Noack, A. *et al.* Mechanism of drug extrusion by brain endothelial cells via lysosomal drug trapping and disposal by neutrophils. *Proc Natl Acad Sci U S A* **115**, E9590-E9599 (2018).
 48. Grimm, C. *et al.* High susceptibility to fatty liver disease in two-pore channel 2-deficient mice. *Nat Commun* **5**, 4699 (2014).
 49. You, H. *et al.* Small interfering RNA targeting the subunit ATP6L of proton pump V-ATPase overcomes chemoresistance of breast cancer cells. *Cancer Lett* **280**, 110-119 (2009).
 50. Petersen, N.H. *et al.* Transformation-associated changes in sphingolipid metabolism sensitize cells to lysosomal cell death induced by inhibitors of acid sphingomyelinase. *Cancer Cell* **24**, 379-393 (2013).

-
51. Geisslinger, F., Müller, M., Vollmar, A.M. & Bartel, K. Targeting Lysosomes in Cancer as Promising Strategy to Overcome Chemoresistance—A Mini Review. *Front Oncol* **10**:1156 (2020).
 52. Schnekenburger, M., Florean, C., Dicato, M. & Diederich, M. Epigenetic alterations as a universal feature of cancer hallmarks and a promising target for personalized treatments. *Curr Top Med Chem* **16**, 745-776 (2016).
 53. Li, T. *et al.* Histone deacetylase 6 in cancer. *J Hematol Oncol* **11**, 111 (2018).
 54. Hubbert, C. *et al.* HDAC6 is a microtubule-associated deacetylase. *Nature* **417**, 455-458 (2002).
 55. Kovacs, J.J. *et al.* HDAC6 regulates Hsp90 acetylation and chaperone-dependent activation of glucocorticoid receptor. *Mol Cell* **18**, 601-607 (2005).
 56. Zhang, X. *et al.* HDAC6 modulates cell motility by altering the acetylation level of cortactin. *Mol Cell* **27**, 197-213 (2007).
 57. Li, Y., Shin, D. & Kwon, S.H. Histone deacetylase 6 plays a role as a distinct regulator of diverse cellular processes. *FEBS J* **280**, 775-793 (2013).
 58. Simoes-Pires, C. *et al.* HDAC6 as a target for neurodegenerative diseases: what makes it different from the other HDACs? *Mol Neurodegener* **8**, 7 (2013).
 59. de Zoeten, E.F. *et al.* Histone deacetylase 6 and heat shock protein 90 control the functions of Foxp3(+) T-regulatory cells. *Mol Cell Biol* **31**, 2066-2078 (2011).
 60. Aldana-Masangkay, G.I. & Sakamoto, K.M. The role of HDAC6 in cancer. *J Biomed Biotechnol* **2011**, 875824 (2011).
 61. DeAngelo, D.J. *et al.* Phase Ia/II, two-arm, open-label, dose-escalation study of oral panobinostat administered via two dosing schedules in patients with advanced hematologic malignancies. *Leukemia* **27**, 1628-1636 (2013).
 62. Zhang, Y. *et al.* Mice lacking histone deacetylase 6 have hyperacetylated tubulin but are viable and develop normally. *Mol Cell Biol* **28**, 1688-1701 (2008).
 63. Butler, K.V. *et al.* Rational design and simple chemistry yield a superior, neuroprotective HDAC6 inhibitor, tubastatin A. *J Am Chem Soc* **132**, 10842-10846 (2010).

-
64. Wang, Z. *et al.* Tubastatin A, an HDAC6 inhibitor, alleviates stroke-induced brain infarction and functional deficits: potential roles of alpha-tubulin acetylation and FGF-21 up-regulation. *Sci Rep* **6**, 19626 (2016).
 65. Zhang, L. *et al.* Tubastatin A/ACY-1215 improves cognition in Alzheimer's disease transgenic mice. *J Alzheimers Dis* **41**, 1193-1205 (2014).
 66. Santo, L. *et al.* Preclinical activity, pharmacodynamic, and pharmacokinetic properties of a selective HDAC6 inhibitor, ACY-1215, in combination with bortezomib in multiple myeloma. *Blood* **119**, 2579-2589 (2012).
 67. Yee, A.J. *et al.* Ricolinostat plus lenalidomide, and dexamethasone in relapsed or refractory multiple myeloma: a multicentre phase 1b trial. *Lancet Oncol* **17**, 1569-1578 (2016).
 68. Vogl, D.T. *et al.* Ricolinostat, the First Selective Histone Deacetylase 6 Inhibitor, in Combination with Bortezomib and Dexamethasone for Relapsed or Refractory Multiple Myeloma. *Clin Cancer Res* **23**, 3307-3315 (2017).
 69. Butler, K.V. & Kozikowski, A.P. Chemical origins of isoform selectivity in histone deacetylase inhibitors. *Curr Pharm Des* **14**, 505-528 (2008).
 70. Haber, M. *et al.* Atypical multidrug resistance in a therapy-induced drug-resistant human leukemia cell line (LALW-2): resistance to Vinca alkaloids independent of P-glycoprotein. *Cancer Res* **49**, 5281-5287 (1989).
 71. Chen, C.C. *et al.* Patch-clamp technique to characterize ion channels in enlarged individual endolysosomes. *Nat Protoc* **12**, 1639-1658 (2017).
 72. Nakano, M., Imamura, H., Nagai, T. & Noji, H. Ca²⁺(+) regulation of mitochondrial ATP synthesis visualized at the single cell level. *ACS Chem Biol* **6**, 709-715 (2011).
 73. Imamura, H. *et al.* Visualization of ATP levels inside single living cells with fluorescence resonance energy transfer-based genetically encoded indicators. *Proc Natl Acad Sci U S A* **106**, 15651-15656 (2009).
 74. Bauer, D.E., Canver, M.C. & Orkin, S.H. Generation of genomic deletions in mammalian cell lines via CRISPR/Cas9. *J Vis Exp*, e52118 (2015).
 75. Ran, F.A. *et al.* Genome engineering using the CRISPR-Cas9 system. *Nat Protoc* **8**, 2281-2308 (2013).
 76. Haeussler, M. *et al.* Evaluation of off-target and on-target scoring algorithms and integration into the guide RNA selection tool CRISPOR. *Genome Biol* **17**, 148 (2016).

-
77. Chao, Y.K. *et al.* TPC2 polymorphisms associated with a hair pigmentation phenotype in humans result in gain of channel function by independent mechanisms. *Proc Natl Acad Sci U S A* **114**, E8595-E8602 (2017).
 78. Bradford, M.M. A rapid and sensitive method for the quantitation of microgram quantities of protein utilizing the principle of protein-dye binding. *Anal Biochem* **72**, 248-254 (1976).
 79. Zhang, J. *et al.* Measuring energy metabolism in cultured cells, including human pluripotent stem cells and differentiated cells. *Nat Protoc* **7**, 1068-1085 (2012).
 80. Fleige, S. *et al.* Comparison of relative mRNA quantification models and the impact of RNA integrity in quantitative real-time RT-PCR. *Biotechnol Lett* **28**, 1601-1613 (2006).
 81. Cang, C. *et al.* mTOR regulates lysosomal ATP-sensitive two-pore Na(+) channels to adapt to metabolic state. *Cell* **152**, 778-790 (2013).
 82. Gatenby, R.A. & Gillies, R.J. Why do cancers have high aerobic glycolysis? *Nat Rev Cancer* **4**, 891-899 (2004).
 83. Li, W. *et al.* Dauricine upregulates the chemosensitivity of hepatocellular carcinoma cells: Role of repressing glycolysis via miR-199a:HK2/PKM2 modulation. *Food Chem Toxicol* **121**, 156-165 (2018).
 84. Wu, H. *et al.* Central role of lactic acidosis in cancer cell resistance to glucose deprivation-induced cell death. *J Pathol* **227**, 189-199 (2012).
 85. Bergers, G. & Benjamin, L.E. Tumorigenesis and the angiogenic switch. *Nat Rev Cancer* **3**, 401-410 (2003).
 86. Denko, N.C. Hypoxia, HIF1 and glucose metabolism in the solid tumour. *Nat Rev Cancer* **8**, 705-713 (2008).
 87. Iturriaga-Vasquez, P., Miquel, R., Ivorra, M.D., D'Ocon, M.P. & Cassels, B.K. Simplified tetrandrine congeners as possible antihypertensive agents with a dual mechanism of action. *J Nat Prod* **66**, 954-957 (2003).
 88. Kazmi, F. *et al.* Lysosomal sequestration (trapping) of lipophilic amine (cationic amphiphilic) drugs in immortalized human hepatocytes (Fa2N-4 cells). *Drug Metab Dispos* **41**, 897-905 (2013).
 89. Zorova, L.D. *et al.* Mitochondrial membrane potential. *Anal Biochem* **552**, 50-59 (2018).
 90. Kogot-Levin, A. *et al.* Upregulation of Mitochondrial Content in Cytochrome c Oxidase Deficient Fibroblasts. *PLoS One* **11**, e0165417 (2016).

-
91. Li, F. *et al.* Molecular mechanisms involved in drug-induced liver injury caused by urate-lowering Chinese herbs: A network pharmacology study and biology experiments. *PLoS One* **14**, e0216948 (2019).
 92. Qi, X.M., Miao, L.L., Cai, Y., Gong, L.K. & Ren, J. ROS generated by CYP450, especially CYP2E1, mediate mitochondrial dysfunction induced by tetrandrine in rat hepatocytes. *Acta Pharmacol Sin* **34**, 1229-1236 (2013).
 93. Yan, C. *et al.* Tetrandrine-induced apoptosis in rat primary hepatocytes is initiated from mitochondria: caspases and endonuclease G (Endo G) pathway. *Toxicology* **218**, 1-12 (2006).
 94. Tian, Y. *et al.* CYP3A5 mediates bioactivation and cytotoxicity of tetrandrine. *Arch Toxicol* **90**, 1737-1748 (2016).
 95. Vlach, M. *et al.* Cytochrome P450 1A1/2, 2B6 and 3A4 HepaRG Cell-Based Biosensors to Monitor Hepatocyte Differentiation, Drug Metabolism and Toxicity. *Sensors (Basel)* **19** (2019).
 96. Josse, R. *et al.* Long-term functional stability of human HepaRG hepatocytes and use for chronic toxicity and genotoxicity studies. *Drug Metab Dispos* **36**, 1111-1118 (2008).
 97. Pernelle, K. *et al.* Automated detection of hepatotoxic compounds in human hepatocytes using HepaRG cells and image-based analysis of mitochondrial dysfunction with JC-1 dye. *Toxicol Appl Pharmacol* **254**, 256-266 (2011).
 98. Hashizume, T. *et al.* In vitro micronucleus test in HepG2 transformants expressing a series of human cytochrome P450 isoforms with chemicals requiring metabolic activation. *Mutat Res* **677**, 1-7 (2009).
 99. Yoshitomi, S. *et al.* Establishment of the transformants expressing human cytochrome P450 subtypes in HepG2, and their applications on drug metabolism and toxicology. *Toxicol In Vitro* **15**, 245-256 (2001).
 100. Steinbrecht, S. *et al.* Metabolic activity testing can underestimate acute drug cytotoxicity as revealed by HepG2 cell clones overexpressing cytochrome P450 2C19 and 3A4. *Toxicology* **412**, 37-47 (2019).
 101. Hashizume, T. *et al.* Advantages of human hepatocyte-derived transformants expressing a series of human cytochrome p450 isoforms for genotoxicity examination. *Toxicol Sci* **116**, 488-497 (2010).

-
102. Huang, Y.T., Liu, T.B., Lin, H.C., Yang, M.C. & Hong, C.Y. Hemodynamic effects of chronic tetrandrine and propranolol administration on portal hypertensive rats. *Pharmacology* **54**, 225-231 (1997).
 103. Lin, T.Y. *et al.* Tetrandrine increased the survival rate of mice with lipopolysaccharide-induced endotoxemia. *J Trauma* **66**, 411-417 (2009).
 104. Yang, T. *et al.* PIM2-mediated phosphorylation of hexokinase 2 is critical for tumor growth and paclitaxel resistance in breast cancer. *Oncogene* **37**, 5997-6009 (2018).
 105. Wolf, A. *et al.* Hexokinase 2 is a key mediator of aerobic glycolysis and promotes tumor growth in human glioblastoma multiforme. *J Exp Med* **208**, 313-326 (2011).
 106. Roberts, D.J., Tan-Sah, V.P., Smith, J.M. & Miyamoto, S. Akt phosphorylates HK-II at Thr-473 and increases mitochondrial HK-II association to protect cardiomyocytes. *J Biol Chem* **288**, 23798-23806 (2013).
 107. Lin, P.H. *et al.* Lysosomal two-pore channel subtype 2 (TPC2) regulates skeletal muscle autophagic signaling. *J Biol Chem* **290**, 3377-3389 (2015).
 108. Jin, H. *et al.* Pulmonary toxicity and metabolic activation of dauricine in CD-1 mice. *J Pharmacol Exp Ther* **332**, 738-746 (2010).
 109. Sun, Y., Yao, T., Li, H., Peng, Y. & Zheng, J. In vitro and in vivo metabolic activation of berbamine to quinone methide intermediate. *J Biochem Mol Toxicol* **31** (2017).
 110. Jin, H. *et al.* Pulmonary Toxicity and Metabolic Activation of Tetrandrine in CD-1 Mice. *Chem. Res. Toxicol.* **24**, 2142-2152 (2011).
 111. Bhagya, N. & Chandrashekar, K.R. Tetrandrine--A molecule of wide bioactivity. *Phytochemistry* **125**, 5-13 (2016).
 112. Llovet, J.M. *et al.* Sorafenib in advanced hepatocellular carcinoma. *N Engl J Med* **359**, 378-390 (2008).
 113. Strumberg, D. *et al.* Safety, pharmacokinetics, and preliminary antitumor activity of sorafenib: a review of four phase I trials in patients with advanced refractory solid tumors. *Oncologist* **12**, 426-437 (2007).
 114. Meßner, M. *et al.* Metabolic implication of tigecycline as an efficacious second-line treatment for sorafenib-resistant hepatocellular carcinoma. *FASEB J* (2020).

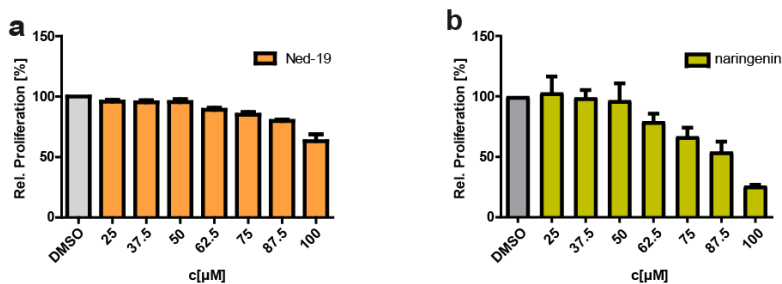
-
115. Hostalkova, A. *et al.* Isoquinoline Alkaloids from *Berberis vulgaris* as Potential Lead Compounds for the Treatment of Alzheimer's Disease. *J Nat Prod* **82**, 239-248 (2019).
 116. Schütz, R., Müller, M., Gerndt, S., Bartel, K. & Bracher, F. Racemic total synthesis and evaluation of the biological activities of the isoquinoline-benzylisoquinoline alkaloid muraricine. *Arch Pharm (Weinheim)*, e2000106 (2020).
 117. Vögerl, K. *et al.* Synthesis and Biological Investigation of Phenothiazine-Based Benzhydroxamic Acids as Selective Histone Deacetylase 6 Inhibitors. *J Med Chem* **62**, 1138-1166 (2019).
 118. DeAngelo, D.J. *et al.* Phase Ia/II, two-arm, open-label, dose-escalation study of oral panobinostat administered via two dosing schedules in patients with advanced hematologic malignancies. *Leukemia* **27**, 1628 (2013).
 119. Yee, A.J. *et al.* Ricolinostat plus lenalidomide, and dexamethasone in relapsed or refractory multiple myeloma: a multicentre phase 1b trial. *Lancet Oncol.* **17**, 1569-1578 (2016).
 120. Ray, A. *et al.* Combination of a novel HDAC6 inhibitor ACY-241 and anti-PD-L1 antibody enhances anti-tumor immunity and cytotoxicity in multiple myeloma. *Leukemia* **32**, 843 (2017).
 121. Amengual, J.E. *et al.* Dual Targeting of Protein Degradation Pathways with the Selective HDAC6 Inhibitor ACY-1215 and Bortezomib Is Synergistic in Lymphoma. *Clin Cancer Res* **21**, 4663-4675 (2015).
 122. Bazzaro, M. *et al.* Ubiquitin proteasome system stress underlies synergistic killing of ovarian cancer cells by bortezomib and a novel HDAC6 inhibitor. *Clin Cancer Res* **14**, 7340-7347 (2008).
 123. Abdel-Wahab, A.F., Mahmoud, W. & Al-Harizy, R.M. Targeting glucose metabolism to suppress cancer progression: prospective of anti-glycolytic cancer therapy. *Pharmacol Res* **150**, 104511 (2019).
 124. Abaza, M.S., Orabi, K.Y., Al-Quattan, E. & Al-Attayah, R.J. Growth inhibitory and chemo-sensitization effects of naringenin, a natural flavanone purified from *Thymus vulgaris*, on human breast and colorectal cancer. *Cancer Cell Int* **15**, 46 (2015).
 125. Latif, A.D. *et al.* Synthesis and In Vitro Antitumor Activity of Naringenin Oxime and Oxime Ether Derivatives. *Int J Mol Sci* **20** (2019).
 126. Wang, S., Dong, G. & Sheng, C. Structural Simplification of Natural Products. *Chem Rev* **119**, 4180-4220 (2019).

-
127. Martinez, E.J., Owa, T., Schreiber, S.L. & Corey, E.J. Phthalascidin, a synthetic antitumor agent with potency and mode of action comparable to ecteinascidin 743. *Proc Natl Acad Sci U S A* **96**, 3496-3501 (1999).
 128. Wang, X. *et al.* Studies on chemical modification and biology of a natural product, gambogic acid (III): determination of the essential pharmacophore for biological activity. *Eur J Med Chem* **46**, 1280-1290 (2011).
 129. Thompson, D.C., Perera, K., Krol, E.S. & Bolton, J.L. o-Methoxy-4-alkylphenols that form quinone methides of intermediate reactivity are the most toxic in rat liver slices. *Chem Res Toxicol* **8**, 323-327 (1995).
 130. Mizutani, T., Satoh, K. & Nomura, H. Hepatotoxicity of eugenol and related compounds in mice depleted of glutathione: structural requirements for toxic potency. *Res Commun Chem Pathol Pharmacol* **73**, 87-95 (1991).
 131. Bolton, J.L., Comeau, E. & Vukomanovic, V. The influence of 4-alkyl substituents on the formation and reactivity of 2-methoxy-quinone methides: evidence that extended π -conjugation dramatically stabilizes the quinone methide formed from eugenol. *Chem. Biol. Interact.* **95**, 279-290 (1995).
 132. Ghosh, C. *et al.* Pattern of P450 expression at the human blood-brain barrier: roles of epileptic condition and laminar flow. *Epilepsia* **51**, 1408-1417 (2010).
 133. Eid, S.Y., El-Readi, M.Z. & Wink, M. Synergism of three-drug combinations of sanguinarine and other plant secondary metabolites with digitonin and doxorubicin in multi-drug resistant cancer cells. *Phytomedicine* **19**, 1288-1297 (2012).
 134. El-Readi, M.Z., Eid, S., Ashour, M.L., Tahrani, A. & Wink, M. Modulation of multidrug resistance in cancer cells by chelidonine and Chelidonium majus alkaloids. *Phytomedicine* **20**, 282-294 (2013).
 135. Morschhauser, F. *et al.* Phase I/II trial of a P-glycoprotein inhibitor, Zosuquidar.3HCl trihydrochloride (LY335979), given orally in combination with the CHOP regimen in patients with non-Hodgkin's lymphoma. *Leuk Lymphoma* **48**, 708-715 (2007).
 136. Woan, K.V. *et al.* Targeting histone deacetylase 6 mediates a dual anti-melanoma effect: Enhanced antitumor immunity and impaired cell proliferation. *Mol Oncol* **9**, 1447-1457 (2015).
 137. Lienlaf, M. *et al.* Essential role of HDAC6 in the regulation of PD-L1 in melanoma. *Mol. Oncol.* **10**, 735-750 (2016).

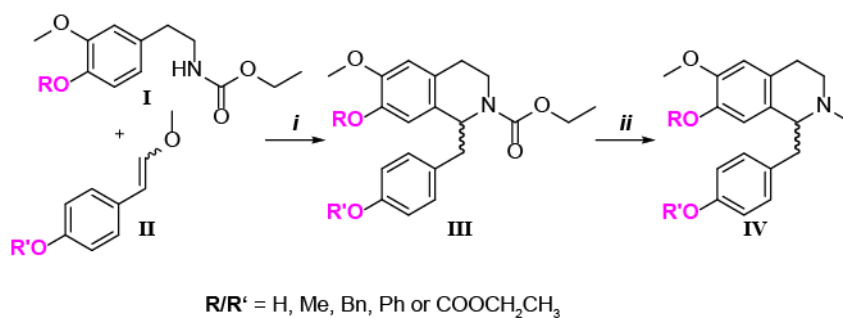
138. Ray, A. *et al.* Combination of a novel HDAC6 inhibitor ACY-241 and anti-PD-L1 antibody enhances anti-tumor immunity and cytotoxicity in multiple myeloma. *Leukemia* **32**, 843-846 (2018).
139. Chhabra, S. Novel Proteasome Inhibitors and Histone Deacetylase Inhibitors: Progress in Myeloma Therapeutics. *Pharmaceuticals (Basel)* **10** (2017).
140. Li, Z. *et al.* Acetylation modification regulates GRP78 secretion in colon cancer cells. *Sci Rep* **6**, 30406 (2016).
141. Woods, D.M. *et al.* HDAC inhibition upregulates PD-1 ligands in melanoma and augments immunotherapy with PD-1 blockade. *Cancer Immunol. Res.* **3**, 1375-1385 (2015).
142. Blankenstein, T., Coulie, P.G., Gilboa, E. & Jaffee, E.M. The determinants of tumour immunogenicity. *Nat. Rev. Cancer* **12**, 307-313 (2012).

APPENDIX

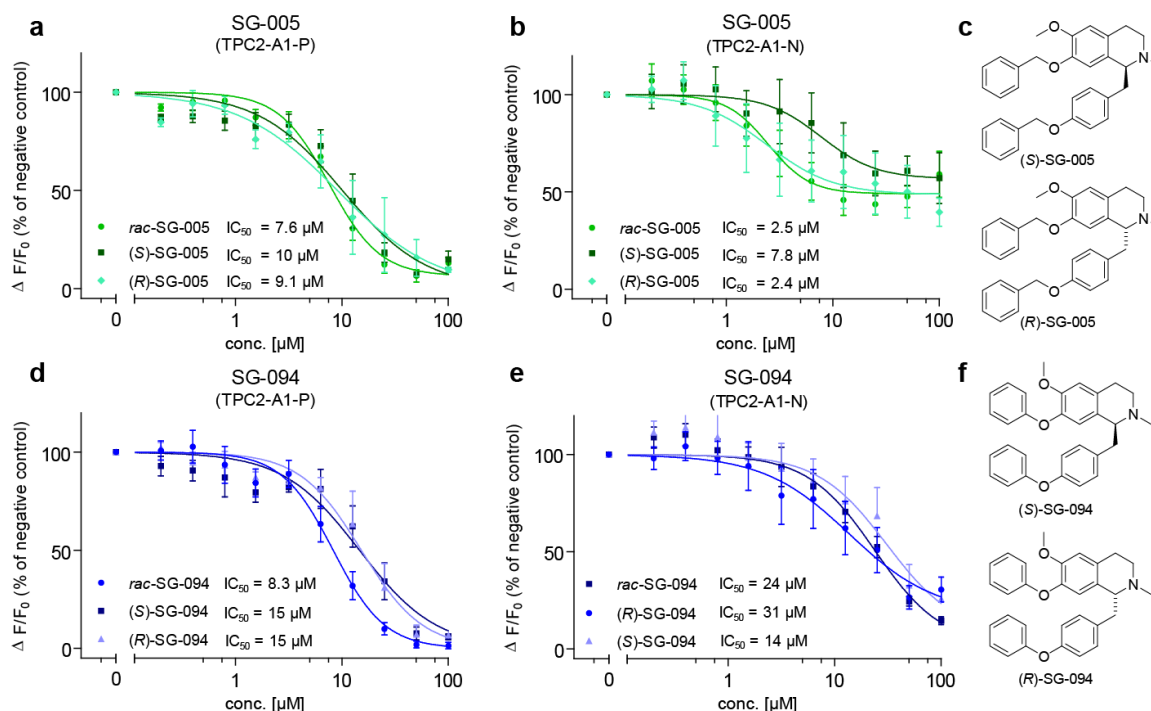




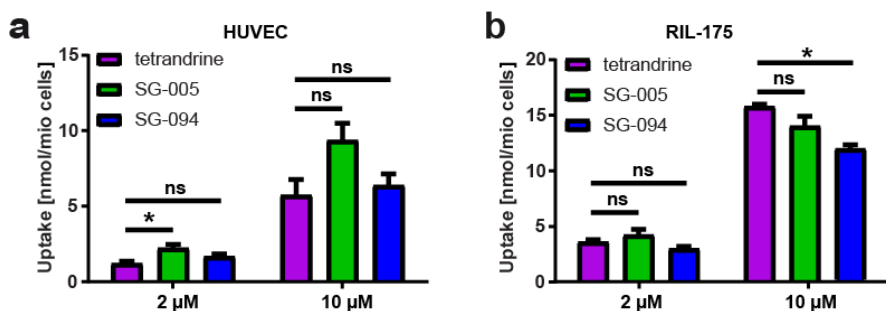
Supplementary Figure 2 | Weak antiproliferative effects of Ned-19 and naringenin. Antiproliferative effects of (a) Ned-19 and (b) naringenin on RIL175 WT cells were assessed by CellTiter-Blue® cell viability assays. (a,b) Fluorescence intensities were normalized to vehicle control and are displayed as mean \pm SEM of three independent experiments.



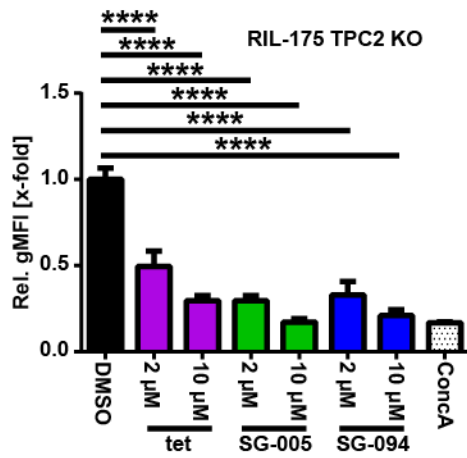
Supplementary Figure 3 | Synthesis of truncated analogs of tetrandrine. (i) Acyl-Pictet-Spengler reaction: phenylethyl amides of type I, enol ethers of type II, TFA, 4 Å molecular sieves, CH_2Cl_2 , $0^\circ\text{C} \rightarrow \text{rt}$, 18-90 h. (ii) Reduction: Carbamates of type III, LiAlH_4 , THF, reflux, 3-20 h. Subsequent construction of diaryl ethers from tetrahydroisoquinolines of type IV with one or two free phenolic groups was achieved by Chan-Evans-Lam coupling with the appropriate arylboronic acids and $\text{Cu}(\text{OAc})_2$ catalyst under alkaline dry conditions. Synthesis of tetrandrine congeners (SG compounds) was performed by Susanne Gerndt (Prof. Bracher, LMU Munich).



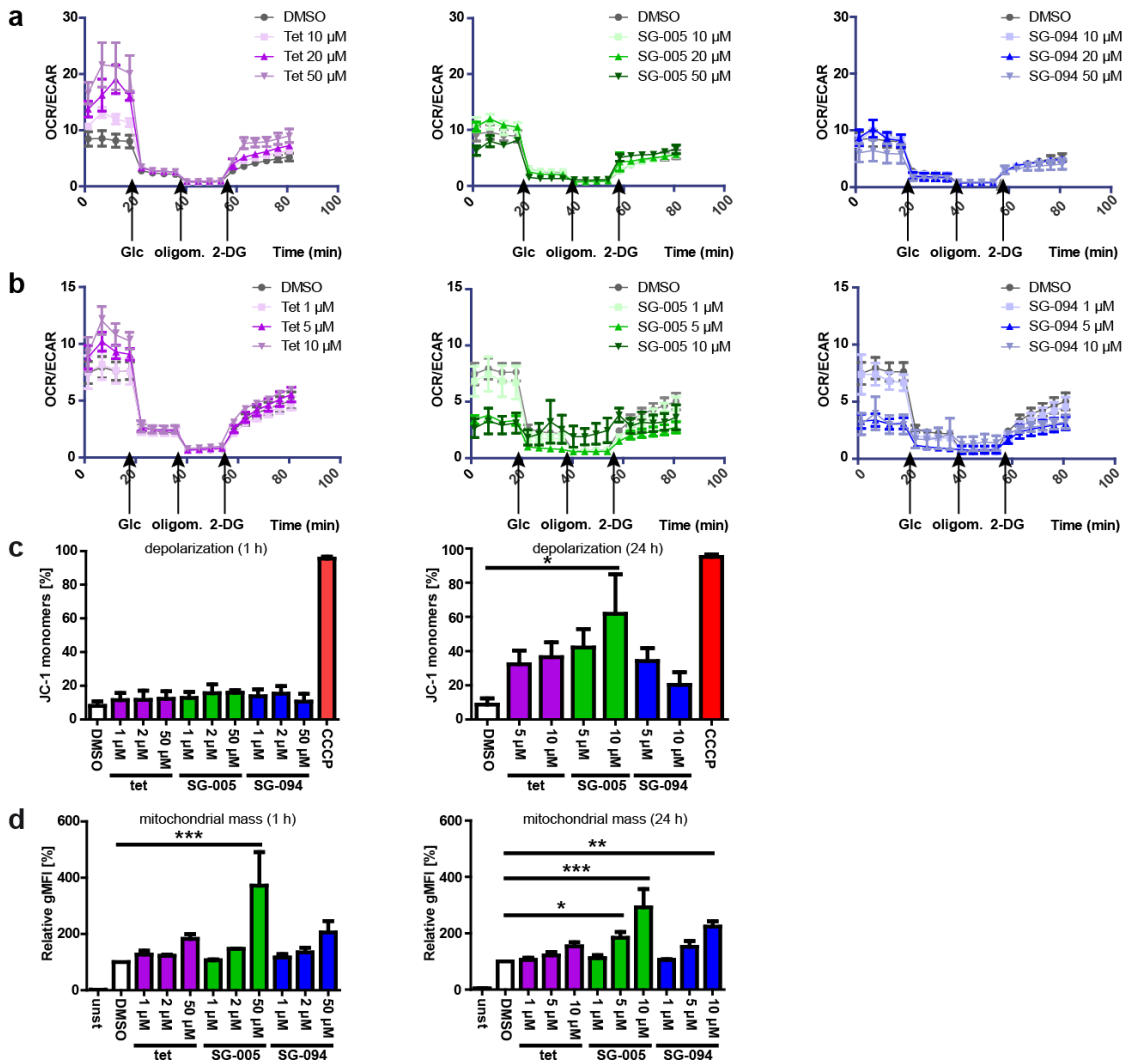
Supplementary Figure 4 | Enantiomerically pure (S)-SG-005, (R)-SG-005, (S)-SG-094 and (R)-SG-094 have inhibitory effects on TPC2, as determined by Fluo-4 based Ca^{2+} imaging. (a-f) After separation of the racemic mixtures SG-005 and SG-094 by semi-preparative chiral HPLC, inhibitory effects of the enantiomers and racemates were probed by Fluo-4 based Ca^{2+} imaging. Therefore, cells were sequentially treated with SG-005, (S)-SG-005, (R)-SG-005, SG-094, (S)-SG-094, (R)-SG-094 and the TPC2 activators (a,d) TPC2-A1-P or (b,e) TPC2-A1-N¹. Line graphs show means \pm SEM of at least three independent experiments. Experiments were performed by Nicole Urban (Prof. Schäfer, Leipzig University).



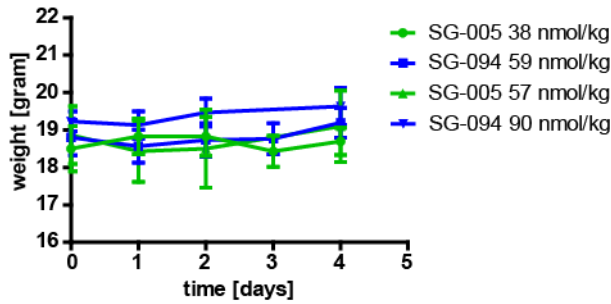
Supplementary Figure 5 | Uptake of tetrandrine, SG-005 and SG-094 into HUVECs and RIL175 cells. The amount of incorporated compounds within 75 min into (a) HUVECs and (b) RIL175 cells was determined by analytical HPLC and was normalized to cell number. (a,b) Bar graphs indicate means \pm SEM from three independent experiments (One-Way ANOVA followed by Tukey's multiple comparison test, * $P < 0.05$, ns, not significant).



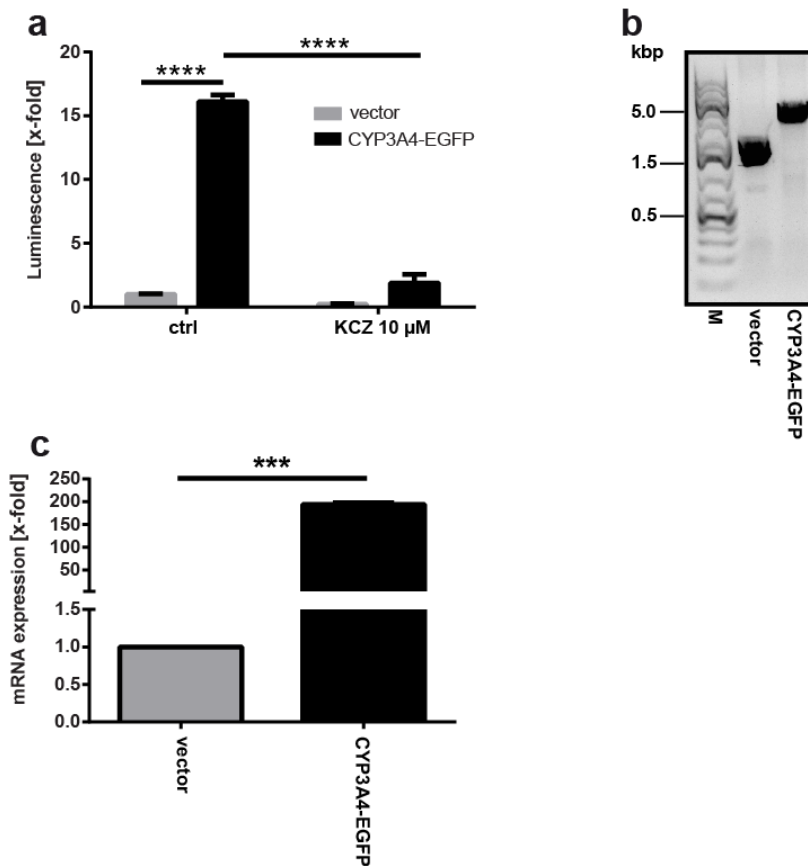
Supplementary Figure 6 | Lysosomal uptake of tetrandrine, SG-005 and SG-094 into RIL175 TPC2 KO cells. Reduction of LysoTracker™ Red fluorescence indicates uptake of tetrandrine, SG-005 and SG-094 into acidic vesicles of RIL175 TPC2 KO cells within 60 min. Geometric means of fluorescence intensity (gMFI) were determined by flow cytometry and normalized to DMSO control. Concanamycin A (ConcA, 10 nM) served as control. Bar graphs indicate mean \pm SEM of two independent experiments (One-Way ANOVA followed by Tukey's multiple comparison test, **** $P < 0.0001$).



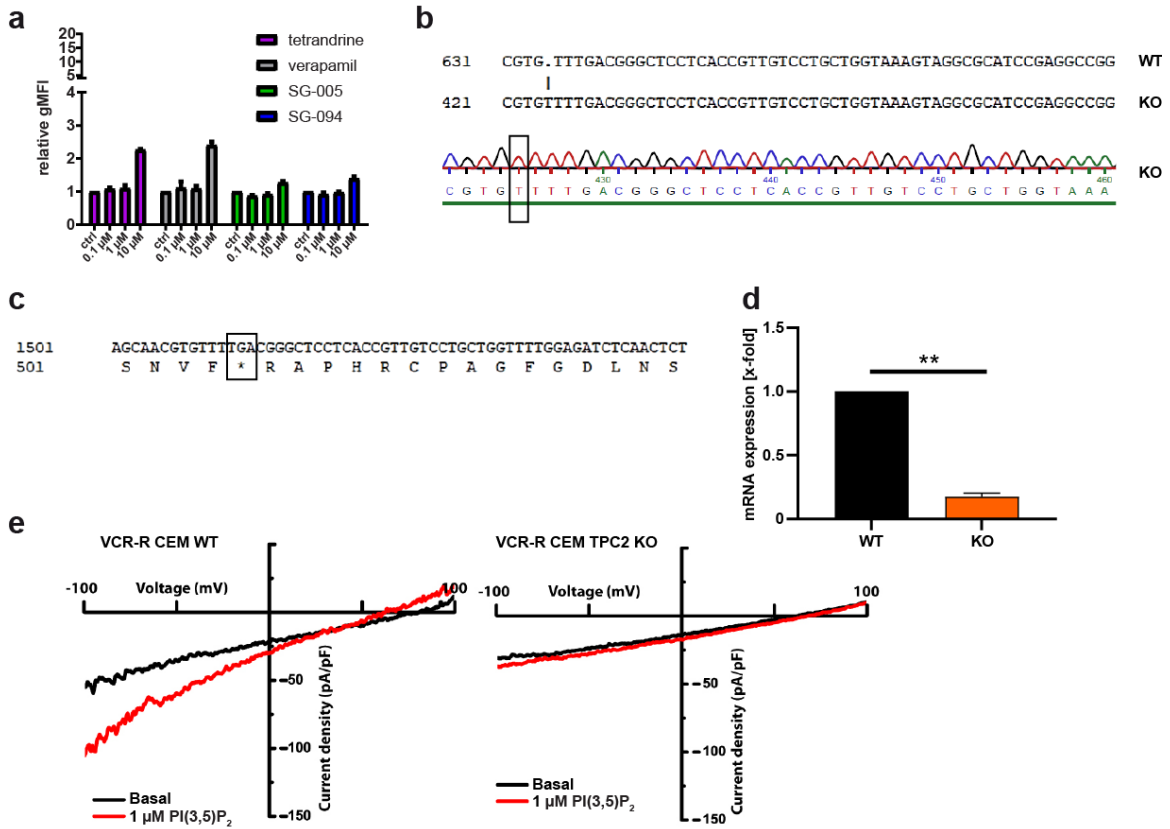
Supplementary Figure 7 | Effects of high-dose and long-term treatment with tetrandrine, SG-005 and SG-094 on metabolic parameters and mitochondria. **(a,b)** Metabolic profiling was performed as described for **Figure 14**. Tetrandrine, SG-005 and SG-094 **(a)** high-dose pre-treatment (10, 20 and 50 μ M) for 1 h and **(b)** low-dose pre-treatment (1, 5 and 10 μ M) for 24 h and their influences on OCR/ECAR ratios of RIL175 WT cells after glucose starvation are shown. The OCR/ECAR ratios are displayed over time as mean \pm SEM, performed in triplicate. **(c,d)** RIL175 WT cells were treated with the indicated concentrations of tetrandrine, SG-005 and SG-094 for 1 h or 24 h, respectively, **(c)** before staining with JC-1 (1 μ g/mL). Loss of mitochondrial membrane potential was quantified by determining the percentage of green fluorescent JC-1 monomers by flow cytometric analysis. The mitochondrial uncoupler CCCP (100 μ M) served as control. Data are shown as mean \pm SEM of two independent experiments (One-Way ANOVA followed by Dunnett's multiple comparison test, * P < 0.05). **(d)** Mitochondrial mass was determined by MitoTracker™ Green FM staining and flow cytometry. Data are displayed as geometric mean of fluorescence intensity (gMFI) relative to vehicle control as mean \pm SEM of at least three independent experiments (One-Way ANOVA followed by Dunnett's multiple comparison test, * P < 0.05, ** P < 0.01, *** P < 0.001).



Supplementary Figure 8 | Mouse weight during the dose-finding test for SG-005 and SG-094. C57Bl/6-Tyr mice were treated with the indicated doses of SG-005 and SG-094 (i.p.) on three consecutive days. Mouse weight was observed and is displayed as mean \pm SEM of three mice per group.



Supplementary Figure 9 | Confirmation of CYP3A4-EGFP activity and presence in transfected HepG2 cells. (a) HepG2 cells were transiently transfected with pcDNA3-CYP3A4-EGFP or empty vector control and CYP3A4 activity was confirmed with a luminescence-based P450-Glo™ assay in presence or absence of the CYP3A4 inhibitor ketoconazole (KCZ, 10 μ M). Experiment was performed in duplicates (Two-Way ANOVA followed by Sidak's multiple comparison test, **** P < 0.0001). (b) Presence of pcDNA3-CYP3A4-EGFP or empty vector control in stably transfected HepG2 cells was confirmed by PCR and subsequent agarose gel analysis. (c) Overexpression of CYP3A4 mRNA in stably transfected HepG2 cells was confirmed by qPCR. Experiment was performed in triplicate (unpaired t-test with Welch's correction, *** P < 0.001).

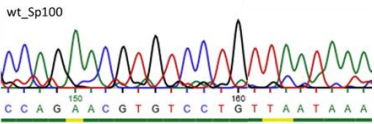
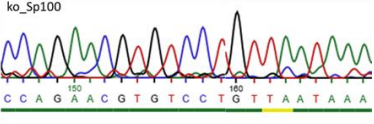
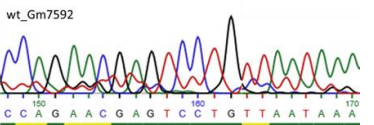
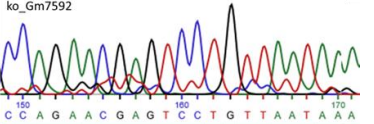
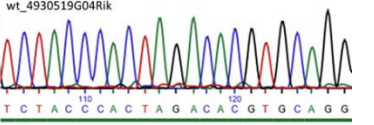
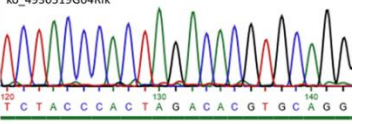


Supplementary Figure 10 | Utilization of VCR-R CEM cells as model cell line to study the influence of TPC2 on P-gp-mediated drug resistance. (a) Calcein-AM retention is low in RIL175 WT cells, as determined by flow cytometry. Cells were incubated with calcein-AM (ctrl), in presence or absence of increasing concentrations of the respective P-gp inhibitors (0.1, 1, 10 μM). Bar graph displays means ± SEM of three independent experiments. (b) A thymidine insertion in the VCR-R CEM TPC2 KO clone was detected by Sanger sequencing. (c) The thymidine insertion led to a premature stop codon, indicated by an asterisk. (d) Significantly reduced 5' mRNA levels, detected by qPCR, indicate the presence of nonsense-mediated decay (NMD) as a response to the insertion. Data are expressed as mean ± SEM, performed in triplicate (unpaired t-test with Welch's correction, ** $P < 0.01$). (e) PI(3,5)P₂-evoked TPC2 currents were reduced in vacuolin-enlarged TPC2 KO cells, compared with the WT control. Patch clamp recordings were performed by Yu-Kai Chao (Prof. Grimm, LMU Munich).

7.1.2 Supplementary Tables

CFD score	gene	TPC 2 geno type	PCR: forward primer (5'-3')	PCR: reverse primer (5'-3')	sequencing primer (5'-3')	potential off-target: Sanger sequencing (5'-3')	polym erase
0.49	<i>Kat7</i>	WT KO	CCCAAAGTTCA GTGAGGCCT	CACCTGTACTCA GCAGACCG	CCCAAAGTTCAG TGAGGCCT	CCAGCACTTGCCC ACTTGGTAGT CCAGCACTTGCCC ACTTGGTAGT	Phusio n Phusio n
0.40	<i>Sh3pxd2a</i>	WT KO	TCACACACACA CACAGCACT	GGGCCCTTTC ATACCTGAC	TCACACACACAC ACAGCACT	TCTACAGACAAGG CACGTTCTGGG TCTACAGACAAGG CACGTTCTGGG	Phusio n Phusio n
0.35	<i>Clint1</i>	WT KO	TGCTTCCTTTC TCCCCGAC	GCAGGTAAGGT ACAGGCAGG	TGCTTCCTTTCAT CCCCGAC	TCTGCTAACAGGA CACAAAGCAGG TCTGCTAACAGGA CACAAAGCAGG	Phusio n Phusio n
0.35	<i>Sp100</i>	WT KO	TGGGTAAGTCA GACCTCTGG	CTGGCTGTCCT GGAACCTCAC	ATATGGGTAAGT AGGACCTCTG	CCAGAACGTGTCC TGTTAATAAAA CCAGAACGTGTCC TGTTAATAAAA	Q5 Q5

Appendix

CFD score	gene	TPC 2 geno type	PCR: forward primer (5'-3')	PCR: reverse primer (5'-3')	sequencing primer (5'-3')	potential off-target: Sanger sequencing (5'-3')	polym erase
0.33	Gm7592	WT	 <p>wt_Sp100 C C A G A A C G T G T C C T G T T A A T A A A</p>	 <p>ko_Sp100 C C A G A A C G T G T C C T G T T A A T A A A</p>		CCAGAATGTGTCC TGTTAATAAA	Q5
0.32	4930519G	WT	 <p>wt_Gm7592 C C A G A A C G A G T C C T G T T A A T A A A</p>	 <p>ko_Gm7592 C C A G A A C G A G T C C T G T T A A T A A A</p>		CCAGAATGTGTCC TGTTAATAAA	Q5
0.29	Ralbp1	WT	 <p>wt_4930519G04Rik T C T A C C C A C T A G A C A C G T G C A G G</p>	 <p>ko_4930519G04Rik T C T A C C C A C T A G A C A C G T G C A G G</p>		TCTACCCACTAGA CACGTGCAGG	Phusion
		KO				TCTACCCACTAGA CACGTGCAGG	Phusion
		KO				CCAGCACGTGTGC TGCTGGTAAA	Phusion
		KO				CCAGCACGTGTGC TGCTGGTAAA	Phusion

Appendix

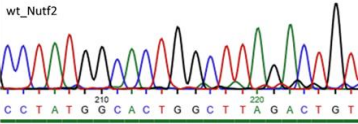
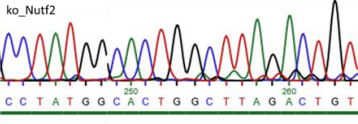
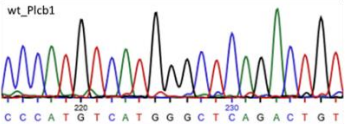
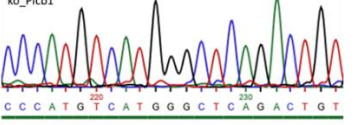
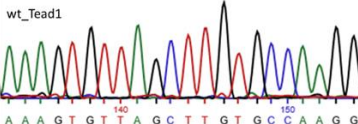
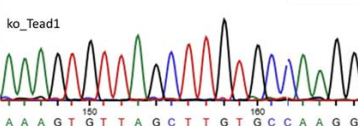
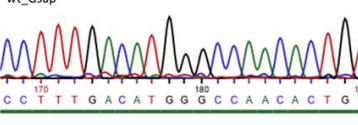
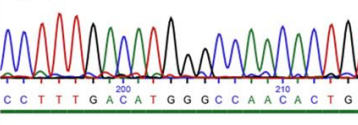
CFD score	gene	TPC 2 geno type	PCR: forward primer (5'-3')	PCR: reverse primer (5'-3')	sequencing primer (5'-3')	potential off-target: Sanger sequencing (5'-3')	polym erase
0.29	2610507B1Rik	wt_Ralbp1					
		WT	CTCTCTGGTCC	CCTTGAGGGAG	CCTTGAGGGAGT	CCCGCACTTGCCC TTTTCTAGT	Phusio n
		KO	AGGCACTTG	TTGAGGCAG	TGAGGCAG	CCCGCACTTGCCC TTTTCTAGT	Phusio n
0.28	Wnt4	wt_Wnt4					
		WT	CGGAGGTGTGG	GAGGCTGACCA	CGGAGGTGTGGA	TCTAGAACTGGG CACAACTGG	Phusio n
		KO	ATTAGCCTC	TCCTTGCTT	TTAGCCTC	TCTAGAACTGGG CACAACTGG	Phusio n
0.27	Gm17495	wt_Gm17495					
		WT	GCTGCTCCCAT	GATTCCAAGTG	GATTCCAAGTGG	CCAGCACTTGCCC TGCTTGTGGA	Q5
		KO	CAATTTGCTC	GTGCCTGGA	TGCCTGGA	CCAGCACTTGCCC TGCTTGTGGA	Q5

Supplementary Table 1 | CRISPR-Cas9 off-target screening. The ten predicted off-target sequences present in exons or introns with the highest CFD scores for the 5' sgRNA were amplified by PCR and analyzed by Sanger sequencing. The investigated off-targets, sequences and the used primer pairs and polymerases are shown.

Appendix

CFD score	gene	TPC2 genotype	PCR: forward primer (5'-3')	PCR: reverse primer (5'-3')	sequencing primer (5'-3')	potential off-target: Sanger sequencing (5'-3')	polym erase
0.29	<i>R3hcc1l</i>	WT	CTCTGATGGTGT GCCTGGTT	CCTGCCACTTCA GCACCTTA	CTCTGATGGTGT GCCTGGTT	ACGATCTTAGCCT GTGCCAGAGG	Phusio n
		KO				ACGATCTTAGCCT GTGCCAGAGG	Phusio n
0.24	<i>Pxn</i>	WT	AGCGCTGTAGA AGGGACCTA	ACTGCTCATCTC TCCCTGGT	AGCGCTGTAGA AGGGACCTA	CCCTTGGCACGGT CTCAGCCAGT	Phusio n
		KO				CCCTTGGCACGGT CTCAGCCAGT	Phusio n
0.20	<i>Tiam1</i>	WT	GCCCAAGGTGT GTTTGCATT	GTGGCTCAATG GCTTCTCCT	GCCCAAGGTGT GTTTGCATT	ACAGACCTAGCCC GTGCCATTGG	Phusio n
		KO				ACAGACCTAGCCC GTGCCATTGG	Phusio n
0.18	<i>Nurr2</i>	WT	GCCTCGTGGGA CTTTACCTC	GATGGATGACCT GAGGTGCC	GCCTCGTGGGA CTTTACCTC	CCTATGGCACTGG CTTAGACTGT	Phusio n
		KO				CCTATGGCACTGG CTTAGACTGT	Phusio n

Appendix

CFD score	gene	TPC2 geno type	PCR: forward primer (5'-3')	PCR: reverse primer (5'-3')	sequencing primer (5'-3')	potential off-target: Sanger sequencing (5'-3')	polym erase	
0.15	<i>Picb1</i>	wt_Nutf2						
		ko_Nutf2						
0.13	<i>Tead1</i>	wt_Picb1						
		ko_Picb1						
0.11	<i>Gsap</i>	wt_Tead1						
		ko_Tead1						
0.11	<i>Gsap</i>	wt_Gsap						
		ko_Gsap						

Supplementary Table 2 I CRISPR-Cas9 off-target screening. The ten predicted off-target sequences present in exons or introns with the highest CFD scores for the 3' sgRNA were amplified by PCR and analyzed by Sanger sequencing. The investigated off-targets, sequences and the used primer pairs and polymerases are shown.

7.2 Abbreviations

Abbreviation	Term
2-DG	2-deoxy-D-glucose
ANOVA	Analysis of variance between groups
APS	Ammonium persulfate
ATP	Adenoside 5'-triphosphate
BBTHIQ	bisbenzyltetrahydroisoquinoline
BCRP	Breast cancer resistance protein
BSA	Bovine serum albumin
BTHIQ	benzyltetrahydroisoquinoline
cDNA	Complementary DNA
CFD	Cutting Frequency Determination
CFSE	Carboxyfluorescein succinimidyl ester
CoV	Coronavirus
CRISPR	Clustered Regularly Interspaced Short Palindromic Repeats
CYP	Cytochrome P450 enzyme
DMEM	Dulbecco's Modified Eagle Medium
DMSO	Dimethyl sulfoxide
DNA	Deoxyribonucleic acid
DTE	Dithioerythritol
DTT	1,4-dithiothreitol
EC ₅₀	Half-maximal effective concentration
ECAR	Extracellular Acidification Rate
ECL	Enhanced chemiluminescence
EDTA	Ethylenediaminetetraacetic acid
EL	endolysosomal
eNOS	Endothelial Nitric Acid Synthase
ERK	Extracellular signal-regulated kinase
FCS	Fetal calf serum
FITC	Fluorescein isothiocyanate
FLIM	Fluorescence lifetime imaging
FRET	Förster resonance energy transfer
GFP	Green fluorescent protein
gMFI	Geometric mean of fluorescence intensity
GRP78	Endoplasmatic reticulum chaperone BiP
HAT	Histone acetylase
HCC	Hepatocellular carcinoma
HDAC	Histone deacetylase
HK II	Hexokinase II

Abbreviation	Term
HPLC	High Performance Liquid Chromatography
HSP90	Heat shock protein 90
HUH-R	Sorafenib-resistant HUH7 cells
HUVECs	Human Umbilical Vein Endothelial Cells
IC ₅₀	half-maximal inhibitory concentration
InDel	Insertion or deletion of bases in the genome
JNK	c-Jun N-terminal kinase
KCZ	Ketoconazole
KO	Knockout
MAPK	Mitogen-activated protein kinase
MDR	Multidrug resistance
MERS	Middle East Respiratory Syndrome
min	Minute
mRNA	Messenger RNA
NAADP	Nicotinic acid adenine dinucleotide phosphate
nd	Not determined
NMD	Nonsense-mediated decay
ns	Not significant
OCR	Oxygen Consumption Rate
OFP	Orange fluorescent protein
OXPPOS	Oxidative phosphorylation
PAGE	polyacrylamide gel electrophoresis
PARP	Poly (ADP-ribose) polymerase
PARP	Poly (ADP-ribose) polymerase
PBMCs	Peripheral blood mononuclear cells
PBS	Phosphate-buffered saline
PCR	Polymerase chain reaction
PD-1	Programmed death receptor-1
PD-L1	Programmed death receptor ligand-1
P-gp	P-glycoprotein
PI(3,5)P ₂	Phosphatidylinositol 3,5-bisphosphate
qPCR	Quantitative real-time PCR
rac	Racemic
RNA	Ribonucleic acid
ROS	Reactive oxygen species
SARS	Severe Acute Respiratory Syndrome
SDS	Sodium dodecyl sulfate
SEM	Standard error of the mean
Ser	Serine

Abbreviation	Term
SERM	Selective estrogen receptor modulator
sgRNA	Single guide RNA
shRNA	Short hairpin RNA
T/E	Trypsin/ethylenediaminetetraacetic acid
TEMED	Tetramethylethylenediamine
tet	Tetrandrine
TPC	Two-pore channel
Tris	Tris(hydroxymethyl)aminomethane
UPR	Unfolded protein response
V-ATPase	Vacuolar ATPase
VCR	Vincristine
VCR-R	Vincristine-resistant
VEGF-A	Vascular endothelial growth factor A
VEGFR2	Vascular endothelial growth factor receptor 2
WT	Wildtype
XF	Extracellular Flux
ZBG	Zinc-binding group

Table 25 | List of abbreviations

7.3 Index of figures

Figure 1 Targeting TPC2 and P-gp in cancer – the project at a glance	2
Figure 2 Characterization of HDAC6 inhibitors in cancer – the project at a glance	3
Figure 3 Structure of murine TPC1..	6
Figure 4 Structures of known HDAC6 inhibitors (tubastatin A, ricolinostat) and the novel hydroxamate-based lead structure KV46.	11
Figure 5 Gating for PE-A positive and Alexa-Fluor-488-A positive populations after staining with JC-1.	32
Figure 6 Gating strategy used to determine viability of PBMCs.	43
Figure 7 Generation of a TPC2 knockout cell line and validation of loss of channel function by migration and dissemination assays	47
Figure 8 TPC2 knockout impairs cancer cell proliferation and tumor growth	48
Figure 9 TPC2 knockout alters the metabolic phenotype of cancer cells.....	50
Figure 10 Structures of the (bis)benzyltetrahydroisoquinoline library.	53
Figure 11 Effects of tetrandrine and the truncated analogues SG-005 and SG-094 on various cancer cell lines.....	54

Figure 12 Identification of novel TPC2 inhibitors	56
Figure 13 SG-005 and SG-094 impair VEGFR2 downstream signaling and are preferably taken up by cancer vs. endothelial cells	58
Figure 14 Tetrandrine, SG-005 and SG-094 affect energy metabolism of RIL175 cells	60
Figure 15 Evaluation of toxicity of tetrandrine, SG-005 and SG-094	62
Figure 16 SG-094 reduces tumor growth <i>in vivo</i>	63
Figure 17 TPC2 knockout reduces phosphorylation of Akt and hexokinase II <i>in vivo</i> ..	65
Figure 18 Postulated metabolic activation and toxification of tetrandrine, dauricine and berbamine, according to Jin <i>et al.</i> ²⁷ , Jin <i>et al.</i> ¹⁰⁸ and Sun <i>et al.</i> ¹⁰⁹	66
Figure 19 Chemical structures of RMS1-RMS10.....	66
Figure 20 Evaluation of toxicity of tetrandrine and the tetrandrine analogues RMS1-RMS10	68
Figure 21 Tetrandrine, SG-005 and SG-094 inhibit P-gp and sensitize VCR-R CEM cells to VCR.....	69
Figure 22 Elacridar is a potent TPC2 antagonist and a moderate inhibitor of cancer cell proliferation.....	71
Figure 23 Loss of TPC2 function decreased proliferation of VCR-R CEM cells and sensitized them to VCR treatment.....	73
Figure 24 Combination of sorafenib with tetrandrine, SG-005 and SG-094 re-sensitized sorafenib-resistant HUH7 (HUH7-R) cells	74
Figure 25 Weak antiproliferative, toxic and TPC2 inhibitory potential of muraricine.....	76
Figure 26 Muraricine inhibits P-gp and provides a therapeutic benefit in combination therapy	77
Figure 27 Chemical structures of the novel HDAC6 inhibitors KV-46, KV-70 and KV-181 (synthesized by Katharina Vögerl, Prof. Bracher, LMU Munich) and the known HDAC6 inhibitor tubastatin A	79
Figure 28 Effects of HDAC6 inhibitors on proliferation and apoptosis of cancer cells and cell viability of non-cancerous liver cells. The pan HDAC-inhibitor vorinostat served as control.....	81
Figure 29 Alteration of expression of immune checkpoint and unfolded protein response protein markers upon HDAC6 inhibition provide the rationale for combination regimens.	82

7.4 Index of tables

Table 1 Compounds.....	14
Table 2 Reagents	16
Table 3 Technical equipment.....	17
Table 4 Cell culture buffers and solutions	18
Table 5 Composition of the hypotonic fluorochrome solution.	20
Table 6 sgRNA sequences/cloning oligomers.....	25
Table 7 Oligo annealing reaction mix.	26
Table 8 Digestion of Cas9 plasmids.....	26
Table 9 Ligation of annealed oligos and Cas9 plasmids.....	26
Table 10 Components used for digestion of non-ligated plasmid.	26
Table 11 Primers used for PCR analysis of exon 2 deletion.....	28
Table 12 hTPC2 sgRNA top and bottom sequences.	28
Table 13 Primers used to detect InDels.	29
Table 14 Restriction digestion mix of CYP3A4 insert.	33
Table 15 Simultaneous plasmid vector linearization and dephosphorylation	33
Table 16 Ligation of linearized, dephosphorylated pcDNA3.1 and CYP3A4 insert.	33
Table 17 Buffers and solutions for Western Blot analysis.....	37
Table 18 Primary antibodies for Western Blot analysis	37
Table 19 Secondary antibodies for Western Blot analysis.....	37
Table 20 Poly-D-lysine coating solution	39
Table 21 Seahorse assay medium.....	40
Table 22 Port solutions for metabolic profiling.....	40
Table 23 Primers with nucleotide codes used for qPCR analysis	41
Table 24 HBSS buffer.	43
Table 25: List of abbreviations	123

7.5 Acknowledgements

Mein allergrößter Dank gilt meiner Doktormutter Frau Vollmar dafür, dass Sie mir ermöglicht haben, nach der Masterarbeit für meine Promotion in Ihrem Arbeitskreis zu bleiben. Außerdem möchte ich mich dafür bedanken, dass Sie mir ermöglicht haben, eigene Ideen in die Tat umzusetzen und dass sie mir das dafür nötige Vertrauen entgegengebracht haben; ebenso dafür, dass Sie sich immer für Diskussionen Zeit nehmen und auch in Stresssituationen immer noch gute Laune verbreiten. Außerdem respektiere ich Sie für ihren Führungsstil, der es beinhaltet, Ihren Mitarbeitern jederzeit das Gefühl zu geben, wertgeschätzt zu werden.

Ich möchte mich zudem bei Karin Bartel für die Betreuung während meiner Promotion bedanken. Danke, Karin, dass du immer ein offenes Ohr hattest und mit Rat zur Seite standest. Ich wünsche dir alles Gute und viel Erfolg für deinen weiteren akademischen Weg und ich bin mir sicher, dass wir in Kontakt bleiben. Eine große Wertschätzung gilt des Weiteren Phuong Nguyen. Danke, liebe Phuong, dass du mir während der Anfangszeit der Promotion sowohl die Fachkenntnisse als auch die Begeisterung für Klonieren und CRISPR-Cas9 vermittelt hast.

Mein Dank gilt auch den weiteren Mitgliedern des Prüfungskomitees, Prof. Bracher (danke lieber Franz für die Erstellung des Zweitgutachtens), Prof. Merkel, Prof. Zahler, Prof. Wagner und Prof. Frieß für Ihre Zeit und Mühe.

Ein aufrichtiges Dankeschön verdient haben sich die Kooperationspartner, ohne deren Mitwirkung die interdisziplinäre Arbeit nicht so vielseitig und interessant geworden wäre, wie sie ist. Dazu zählen insbesondere die Chemikerinnen Susanne Gerndt und Ramona Schütz und deren Chef, Franz Bracher (Department Pharmazie, LMU München), sowie Yu-Kai Chao und Christian Grimm vom Endolysosomal Ion Channel Lab (Walther-Straub-Institut für Pharmakologie und Toxikologie, Medizinische Fakultät der LMU München). Außerdem bedanke ich mich bei Anna Niedrig, Christoph Müller und Katharina Vögerl (Department Pharmazie, LMU München) für die gute und konstruktive Zusammenarbeit.

Weiterhin bin ich sehr dankbar für die tatkräftige Unterstützung durch TAs und, die Studenten, die ich während der Promotion betreuen durfte. Danke an Bernadette Grohs, Jana Peliskova, Silvia Schnegg, Franz Geisslinger, Lucas Siow, Linus Schömig, Julian Frädriich und Moritz Schroll. Eure hervorragende Arbeit war mir eine große Hilfe.

Außerdem möchte ich mich bei den Kollegen der „alten“ (Max, Flo G., Chrissi, Martina, Caro, Daniel und Conny) und „neuen“ Riege (Franz, Flo L.) für das freundschaftliche Verhältnis und die gegenseitige Unterstützung bedanken. Hier möchte ich auch die gute Arbeitsatmosphäre im Labor B4.014 und damit Max (danke für die Betreuung der Masterarbeit und die Aufnahme in den Arbeitskreis), Jana (keep rocking!) und Kerstin hervorheben. Antje danke ich für die vielen unterhaltsamen Kaffeepausen. Dank euch allen bin ich auch, obwohl Experimente zeitweise nicht funktioniert haben, gerne zur Arbeit gegangen und den Frust konnte man sich bei Mittagspausen, Kaffeepausen, Wiesn-Besuchen, einem (oder auch mehreren) Feierabendbier(en) oder beim Sport mit den (über die Campusgrenzen hinaus bekannten) LMU Shakers sowie bei der B2Run-Vorbereitung

kollektiv abbauen. In dem Zusammenhang möchte ich mich bei meinen Studienfreunden (den „Uni-Bitches“ und der „Nage-Crew“) dafür bedanken, dass wir uns seit dem ersten Semester gemeinsam durchkämpfen und uns nicht aus den Augen verloren haben.

Mama und Papa, ich bin euch unendlich dankbar dafür, dass eure Tür für mich immer offensteht und dass ich jederzeit, insbesondere in schlechten Zeiten, auf eure Unterstützung zählen kann. Deswegen habe ich euch diese Arbeit gewidmet. Bedanken möchte ich mich auch bei meinen Geschwistern Sabrina und Markus. Auch wenn ich euch leider viel zu selten sehe, habe ich mit euch immer das Gefühl, dass ich nie ganz erwachsen werden muss.

7.6 List of publications and conference contributions

7.6.1 Research articles

- i. Müller, M., Gerndt, S., Chao, Y.K., Zisis, T., Nguyen, O.N.P., Gerwien, A., Urban, N., Müller, C., Gegenfurtner, A., Geisslinger, F., Ortler, C., Zahler, S., Biel, M., Schäfer, M., Grimm, C., Bracher, F., Vollmar, A.M., and Bartel, K. (2020). Gene editing and synthetically accessible inhibitors reveal role for TPC2 in cancer cell proliferation and tumor growth. *Cell Chem Biol*, in revision.
- ii. Schütz, R.* , Müller, M.*, Geisslinger, F., Vollmar, A.M., Bartel, K., and Bracher, F. (2020). Synthesis, biological evaluation and toxicity of novel tetrandrine analogues. *Eur J Med Chem*, accepted.
*These authors contributed equally to the article.
- iii. Schütz, R., Müller, M., Gerndt, S., Bartel, K., and Bracher, F. (2020). Racemic total synthesis and evaluation of the biological activities of the isoquinoline-benzylisoquinoline alkaloid muraricine. *Arch Pharm (Weinheim)*, e2000106.
- iv. Geisslinger, F., Müller, M., Vollmar, A.M., and Bartel, K. (2020). Targeting Lysosomes in Cancer as Promising Strategy to Overcome Chemoresistance – A Mini Review. *Front Oncol*, accepted for publication.
- v. Meßner, M., Schmitt, S., Ardelt, M.A., Fröhlich, T., Müller, M., Pein, H., Huber-Cantonati, P., Ortler, C., König, L.M., Zobel, L., Köberle, A., Arnold, G.J., Rothenfuß, S., Kiemer, A.K., Gerbes, A.L., Zischka, H., Vollmar, A.M., and Pachmayr, J. (2020). Metabolic implication of tigecycline as an efficacious second-line treatment for sorafenib-resistant hepatocellular carcinoma. *FASEB J*.
- vi. Vögerl, K., Ong, N., Senger, J., Herp, D., Schmidtkunz, K., Marek, M., Müller, M., Bartel, K., Shaik, T.B., Porter, N.J., Robaa, D., Christianson, D.W., Romier, C., Sippl, W., Jung, M., and Bracher, F. (2019). Synthesis and Biological Investigation of Phenothiazine-Based Benzhydroxamic Acids as Selective Histone Deacetylase 6 Inhibitors. *J Med Chem* 62, 1138-1166.
- vii. Ardelt, M.A., Fröhlich, T., Martini, E., Müller, M., Kanitz, V., Atzberger, C., Cantonati, P., Messner, M., Posselt, L., Lehr, T., Wojtyniak, J.G., Ulrich, M., Arnold, G.J., König, L., Parazzoli, D., Zahler, S., Rothenfusser, S., Mayr, D., Gerbes, A., Scita, G., Vollmar, A.M., and Pachmayr, J. (2018). Inhibition of Cyclin-dependent Kinase 5 - a Novel Strategy to Improve Sorafenib Response in HCC Therapy. *Hepatology*.

- viii. Chao, Y.K., Schludi, V., Chen, C.C., Butz, E., Nguyen, O.N.P., Müller, M., Krüger, J., Kammerbauer, C., Ben-Johny, M., Vollmar, A.M., Berking, C., Biel, M., Wahl-Schott, C.A., and Grimm, C. (2017). TPC2 polymorphisms associated with a hair pigmentation phenotype in humans result in gain of channel function by independent mechanisms. *Proc Natl Acad Sci U S A* 114, E8595-E8602.
- ix. Capasso, C., Magarkar, A., Cervera-Carrascón, V., Fusciello, M., Feola, S., Müller, M., Garofalo, M., Kuryk, L., Tähtinen, S., Pastore, L., Bunker, A., and Cerullo, V. (2017). A novel in silico framework to improve MHC-I epitopes and break the tolerance to melanoma. *Oncoimmunology* 6, e1319028.

7.6.2 Conference contributions

- i. Müller, M., Geisslinger, F., Gerndt, S., Schütz, R., Chao, Y.K., Bracher, F., Grimm, C., Vollmar, A.M., and Bartel, K., **61st Annual Meeting & Exposition of the American Society of Hematology in Orlando, USA (December 2019)**. Blocking Lysosomal Two-Pore Channel 2 Function Inhibits Proliferation of Multidrug Resistant Leukemia Cells and Sensitizes Them to Vincristine Treatment. *Blood* 134(Supplement_1):2081-2081, DOI: 10.1182/blood-2019-128195.
- ii. Ardelt, M.A., Fröhlich, T., Martini, E., Müller, M., Kanitz, V., Atzberger, C., Cantonati, P., Meßner, M., Posselt, L., Lehr, T., Wojtyniak, J.G., Ulrich, M., Arnold, G.J., König, L., Parazzoli, D., Zahler, S., Rothenfußer, S., Mayr, D., Gerbes, A., Scita, G., Vollmar, A.M., and Pachmayr, J., **26th Scientific Congress of the Austrian Pharmaceutical Society in Graz, Austria (April 2019)**. Cdk5 Inhibition - The Key to Enhancing the Standard of Care in Hepatocellular Carcinoma Treatment. Final Programme & Book of Abstracts.
- iii. Meßner, M., Zischka, H., Schmitt, S., Ardelt, M.A., Huber-Cantonati, P., Fröhlich, T., Arnold, G.J., Atzberger, C., Müller, M., Pein, H., Köberle, A., Zobel, L.M., König, L., Vollmar, A.M., and Pachmayr, J., **26th Scientific Congress of the Austrian Pharmaceutical Society in Graz, Austria (April 2019)**. Diamonds in the rough - With low application Antibiotics against Tumor Relapse of sorafenib-resistant Hepatocellular Carcinoma. Final Programme & Book of Abstracts.
- iv. Müller, M., Chao, Y.K., Gerndt, S., Nguyen, O.N.P., Biel, M., Bracher, F., Vollmar, A.M., Keller, M., Grimm, C., and Bartel, K., **4th German Pharm Tox Summit in Stuttgart, Germany (February 2019)**. Two-pore channels shut down – targeting TPC2 inhibits proliferation of cancer cells in vitro and inhibits tumor growth in vivo. Final Programme & Book of Abstracts.

-
- v. Müller, M., Chao, Y.K., Gerndt, S., Schürmann, J., Schütz, R., Atzberger, C., Nguyen, O.N.P., Biel, M., Bracher, F., Vollmar, A.M., Keller, M., Grimm, C., and Bartel, K., **4th German Pharm Tox Summit in Stuttgart, Germany (February 2019)**. Targeting endolysosomal calcium channels as novel strategy to treat cancer. Final Programme & Book of Abstracts.
- vi. Müller, M., Gerndt, S., Arner, A., Chao, Y.K., Schömig, L., Atzberger, C., Biel, M., Bracher, F., Vollmar, A.M., Binder, V., Keller, M., Grimm, C., and Bartel, K., **60th Annual Meeting & Exposition of the American Society of Hematology in San Diego, USA (December 2018)**. Reversal of Chemoresistance in Leukemia Cells Using Synthetic Bisbenzylisoquinoline Derivatives. Blood 132(Supplement 1):3504-3504, DOI: 10.1182/blood-2018-99-111651.
- vii. Müller, M., Chao, Y.K., Gerndt, S., Schütz, R., Atzberger, C., Nguyen, O.N.P., Biel, M., Bracher, F., Vollmar, A.M., Bartel, K., Keller, M., and Grimm, C., **12th ILCA (International Liver Cancer Association) Annual Conference in London, United Kingdom (September 2018)**. Targeting Two-Pore Channel Function in HCC – Overcoming Limitations of Tetrandrine Treatment. Final Programme & Book of Abstracts.
- viii. Ardelt, M.A., Fröhlich, T., Martini, E., Müller, M., Kanitz, V., Atzberger, C., Posselt, L., Posselt, L., Lehr, T., Wojtyniak, J.G., Ulrich, M., Arnold, G.J., König, L., Parazzoli, D., Zahler, S., Rothenfuß, S., Mayr, D., Gerbes, A., Scita, G., Vollmar, A.M., and Pachmayr, J., **12th ILCA (International Liver Cancer Association) Annual Conference in London, United Kingdom (September 2018)**. Blocking Traffic Flow – Cdk5 Inhibition Introduces Novel Ways to Prevent Sorafenib Treatment Escape in HCC Cells. Final Programme & Book of Abstracts.
- ix. Müller, M., Chao, Y.K., Gerndt, S., Atzberger, C., Nguyen, O.N.P., Biel, M., Bracher, F., Vollmar, A.M., Keller, M., Grimm, C., and Bartel, K., **15th International Meeting of the European Calcium Society in Hamburg, Germany (September 2018)**. Two-Pore Channels as novel drug targets for cancer therapy.
- x. Capasso, C., Magarkar, A., Cervera-Carrascón, V., Müller, M., Garofalo, M., Kuryk, L., Fusciello, M., Ylösmäki, E., Bunker, A., and Cerullo, V., **4th ESMO (European Society of Medical Oncology) Symposium in Lausanne, Switzerland (November 2016)**. Enhanced anti-cancer vaccines with a new epitope improvement system. Annals of Oncology 27(suppl_8), DOI: 10.1093/annonc/mdw525.03.

- xi. Capasso, C., Cardella, D., Müller, M., Garofalo, M., Kuryk, L., Peltonen, K., and Cerullo, V., **19th ASGCT (American Society of Gene & Cell Therapy) Annual Meeting in Washington, D.C., USA (May 2016)**. Oncolytic Vaccines in Combination with PD-L1 Blockade for the Treatment of Melanoma. *Molecular Therapy* 24(1); DOI: 10.1016/S1525-0016(16)33217-8.
- xii. Capasso, C., Magarkar, A., Cervera-Carrascón, V., Müller, M., Garofalo, M., Kuryk, L., Cardella, D., Peltonen, K., Bunker, A., and Cerullo, V., **19th ASGCT (American Society of Gene & Cell Therapy) Annual Meeting in Washington, D.C., USA (May 2016)**. Oncolytic Vaccines with Modified Tumor Epitopes for Cancer Immunotherap. *Molecular Therapy* 24(1); DOI: 10.1016/S1525-0016(16)33450-5.